Investigating volcano-tectonic interactions in a youthful rift segment of the East African Rift System

J. Robert Jones

Dissertation submitted to the Faculty of the
Virginia Polytechnic Institute and State University
in partial fulfillment of the requirements for the degree of

Doctor of Philosophy
in
Geosciences

D. Sarah Stamps, Chair
John Hole
James Spotila
Christelle Wauthier
Sean Bemis

May 7, 2021
Blacksburg, Virginia

Keywords: Geodesy, volcanoes, rifting

Investigating volcano-tectonic interactions in a youthful rift segment of the East African Rift System

J. Robert Jones

(ABSTRACT)

Continental rifting, like other plate tectonic processes, plays a large role in shaping the Earth's crust. Active rift zones evolve from repeated tectonic and magmatic events including volcanic activity. Through investigations of currently and previously active rifts, scientists have discovered considerable interactions between these tectonic and magmatic processes during a rift's evolution; however questions remain about these interactions especially in youthful stages of rifts. We investigate an early phase magma-rich section of the East African Rift System (EARS), named the Eastern Branch to assess volcano-tectonic interactions. The Eastern Branch of the EARS consists of volcanically rich rifts that are actively spreading the Nubian Plate, Somalian plates, and Victoria block at different evolutionary stages making it an ideal study area for volcano-tectonic interactions. Our initial investigation of active volcano-tectonic interactions centered on a rifting event that occurred between 2007-2008 in the Natron Rift, a rift segment in the southern Eastern Branch located in Northern Tanzania. This rifting event contained multiple occurrences of tectonic, magmatic, and volcanic activity in close proximity. We examine the stress transferred from these events to the Natron Fault, which is the major border fault in the area, with analytical modeling using the USGS program Coulomb 3.4. We processed Global Positioning System (GPS) data that recorded slip on the major border fault in the region in early January 2008 and test which events could generate large enough stress changes to trigger the observed slip using a previously defined threshold of 0.1 MPa. These initial models were created using simplified

model parameters, such as an elastic homogeneous half-space, and find that 1) magmatically induced stress perturbations have the potential to trigger fault slip on rift border faults, 2) magmatic events have the potential to trigger strike-slip motions on a rift border fault, and 3) the proximity of magmatic activity may affect occurrences of slip on adjacent border faults. We then further investigate volcano-tectonic interactions in the Natron Rift by testing using numerical modeling with the CIG finite element code PyLith. We systematically test how adding topography, heterogeneous materials, and various reservoir volumes to an deflating 3 km deep magma reservoir system at the active volcano Ol Doinyo Lengai can affect stress transfer to the adjacent Natron Fault. We compare eight models with variations in topography, material properties, and reservoir volumes to calculate the percent differences between the models; to test their effects on the stress change results. We find that topography plays the largest role with the effect increasing with reservoir size. Finally, we seek to improve the capability of investigating volcano-tectonic interactions in the Natron Rift at faster time-scales by improving Global Navigation Satellite System (GNSS) positioning data (latitude, longitude, and height) collection and distribution capabilities. In the final part of this work, we describe a new Python-based data broker application, GNSS2CHORDS, that can stream real-time centimeter precision displacement data distributed by UNAVCO real-time GNSS data services to an online EarthCube cybertool called CHORDS. GNSS2CHORDS is applied to the TZVOLCANO GNSS network that monitors Ol Doinyo Lengai in the Natron Rift and its interactions with the adjacent rift border fault, the Natron Fault. This new tool provides a mechanism for assessing volcano-tectonic interactions in real-time. In summary, this work provides a new avenue for understanding volcano-tectonic interactions at unprecedented, 1-second time-scales, demonstrates slip can be triggered by small stress changes from magmatic events during early phase rifting, and provides insights into the key role of volcanic topography during volcano-tectonic interactions.

Investigating volcano-tectonic interactions in a youthful rift segment of the East African Rift System

J. Robert Jones

(GENERAL AUDIENCE ABSTRACT)

Investigating interactions between active volcanoes and tectonics (fault zones) is important for understanding how continental rifts grow and evolve over time. Modern researchers use geodetic data, geologic models, and computer simulations of rift processes; like volcanic eruptions and fault movement; to understand how stress in transferred and material deforms due to rift activity. We are especially interested in understanding the stress interactions when volcanic eruptions and earthquakes happen together over a short time period. Our projects apply these tools to examine a segment of the largest active continental rift zone, the Natron Rift in the East African Rift System (EARS), to understand more about the details of these volcano-tectonic interactions when continents break apart (rifting). We first present results that stress transferred to the Natron Fault associated with magmatic activity from the volcano Ol Doinyo Lengai may trigger a major fault to move. Next, we continue our investigations into volcano-tectonic interactions by seeing how volcanic properties could affect stress transferred in the Natron Rift region. We choose to initially test stress variations associated with different 1) topography surfaces, 2) material properties, and 3) reservoir volumes associated with the volcano Ol Doinyo Lengai using a more advanced computer modeling approach. This deeper investigation provides information about the individual roles these parameters play in a younger rift region. We present results that topography has the most influence on the stress transferred to the Natron Fault in our models, and that the other parameters did not play a large role in influencing the

stress transferred. Finally we work to increase the ability for researchers to perform geodetic studies in the Natron Rift by providing a new method to share surface displacement data at an unprecedented 1 position a second rate (near real-time). This new method is a data broker application called GNSS2CHORDS that can stream cm precision displacement data to an online cybertool called CHORDS. With our models and data provided through open source methods this work contributes significantly to our understanding of volcano-tectonic interactions.

Dedication

Dedicated to my grandmother Mary Stevenson; a lifelong educator and origin of my first nickname "The Professor"

Acknowledgments

First, I would like to thank and acknowledge everything that my primary advisor, Dr. D. Sarah Stamps, has done over the course of accomplishing this work. Dr. Stamps provided critical guidance in my thesis design as well as introduced me to the world and methods of Geodesy and Tectonophysics. Dr. Stamps also provided me multiple opportunities to grow my technical knowledge in computer science and my skills as a leader in both the field and the lab. I have appreciated the continued mentoring in my life over my time as a graduate student, and fully recognize the additional benefits from working with Dr. Stamps.

In addition to my primary advisor, I have had the privilege to have amazing researchers agree to be a part of my graduate committee. I would like to thank, in memoriam, one of my first committee members Dr. Bob Tracy, professor and previous department head, who taught me both as an undergraduate and a graduate student. Dr. Tracy provided me all of the background necessary to understand volcanoes, and I would not be as successful as I am now without his help. I also want to thank the members of my committee Dr. John Hole, and Dr. James Spotila for their help and guidance; both as an undergraduate and a graduate student. I am also thankful to my committee members Dr. Christelle Wauthier and Dr. Sean Bemis for joining at a crucial moment when I requested more expertise and feedback on my work.

I am also grateful and want to acknowledge other researchers that I have collaborated with to complete my dissertation. This includes: Dr. Elifuraha Saria, who was one of my introductions to field work and the Natron Rift, Dr. Juliet Biggs, who added valuable feedback

to my first published paper; and Dr. Brad Aagaard, who helped me develop my modeling and PyLith skills. I am also thankful for the python skills that I learned and the personal relationships established in the National Center of Atmospheric Research and my internship with the C.I.S.L group including but not limited to Mike Daniels, Mike Dye, Eric Nienhouse, Sophie Hou, Nathan Hook, and the SIParCS Team. I also want to thank David Mencin and the UNAVCO Organization for sharing their expertise of GPS/GNSS units and providing excellent field support. I also want to thank all of the other scientist who have helped or supported me through various conferences, workshops, and short courses especially the AGU and EarthCube communities.

I want to give special acknowledgements to the Geodesy and Tectonophysics group for all of their support over the years through classwork, assignments, and always ready to help with presentation preparation. I also want to give a giant thank you to the Laohs who provided a home away from home in Blacksburg. I am also thankful for all of my friends who have supported me over my time in school; from my fraternity brothers, to the great people I met in the Department of Geosciences including my fellow graduate students. Finally, I want to thank my dad, mother, brother, sister, and family for never giving up on me; dealing with all of my absences over the years; and for helping to take care of my Number 1, the best German shepherd in the world, Crixus.

Contents

List of Figures

List of Tables

Chapter 1

Evidence for slip on a border fault triggered by magmatic processes in an immature continental rift

J. Robert Jones[1], D. Sarah Stamps[1], Christelle Wauthier[2], 3, Elifuraha Saria[4], Juliet Biggs[5]

1. Virginia Tech, Blacksburg, VA, USA
2. Pennsylvania State University, State College, PA, USA
3. Institute for CyberScience, Pennsylvania State University, State College, PA, USA
4. Ardhi University, Dar es Salaam, Tanzania
5. University of Bristol, Bristol, United Kingdom

Jones, J. R., Stamps, D. S., Wauthier, C., Saria, E., & Biggs, J. (2019). Evidence for slip on a border fault triggered by magmatic processes in an immature continental rift. Geochemistry, Geophysics, Geosystems, 20(5), 2515-2530, https://doi.org/10.1029/2018GC008165.

1.1 Abstract

Continental rifting evolves through repeated tectonic and magmatic processes. Here we investigate the 2007-2008 Northern Tanzania rifting episode to understand the interactions between magmatism and border fault slip during immature continental rifting. We compare modelled stress changes with geodetic observations from the western adjacent border fault of the Natron basin. We model six distinct phases of the rifting episode, including the eruptive activity of Ol Doinyo Lengai. The southern portion of the border fault experienced a positive cumulative Coulomb stress change, consistent with newly processed Global Positioning System (GPS) data showing a distinct instance of slip during this time period. Our work suggests active volcanism and faulting are correlated in time, indicating magmatism associated with volcanic activity influences slip on border faults in immature continental rifts.

1.2 Introduction

The interactions of long-term, spatially-broad tectonic forces with short-term, localized magmatism play a crucial role in continental rift initiation by focusing strain and changing the regional stress field. These interactions have been studied in mature, youthful, and failed rifts, as well as mid-ocean ridges. Studies have revealed crucial mechanisms and processes responsible for rift initiation of the East African Rift System (EARS, Figure 1.1A). For example, from seismic moment calculations, Calais et al. [2008] suggests the seismic moment of slow slip, associated with diking, can be accommodated up to 65% during early stages of continental rifting, specifically in the region of the southern Gregory Rift of the EARS (Natron Rift, Figure 1.1B). Additional studies of youthful continental rifting in the

EARS indicate dike orientations are influenced by changes in pressurized magma reservoirs [Muirhead et al., 2015]. In later, intermediate stages of continental rifting, the influence of magmatism has been linked with concentrated extension in the center of active rifts [Keir et al., 2009], formation of silicic caldera systems [e.g. Hutchison et al., 2016], and magmatic triggering of fault slip through dike intrusions [e.g. Wauthier et al., 2015, 2013].

Several models have been proposed to explain how continental rifting processes begin and how they interact during immature rifting. These models include the tectonic and magma-assisted rift-initiation models [Buck, 2006], but more recent models have been proposed. Other rift initiation models invoke more specific concepts like fluid-assisted processes that promote slip on pre-existing weaknesses [Leseane et al., 2015, Roecker et al., 2017] and magmatic fluid release that causes crustal weakening [i.e. Ebinger et al., 2017, Lee et al., 2016, Muirhead et al., 2016]. In this project, we advance our understanding of magma-tectonic interactions during magma-assisted immature rifting in the southern Gregory Rift. We focus on the magma-assisted model due to the key role magmatism plays in the Eastern branch of the EARS. The magma-assisted rifting model assumes magmatic intrusions occur early in continental rifting and weaken the surrounding lithosphere. This lithospheric weakening allows for the magnitude of far-field forces required to initiate continental rifting to be reduced by up to 85% [Buck, 2006]. Further, thermal weakening from intrusions of magma from dikes and volcanic reservoirs makes magmatism a crucial component of the rift initiation process [Bialas et al., 2010].

This study seeks to elucidate how events that took place in the Southern Gregory rift during the 2007-2008 Tanzania rifting episode, influenced the border fault system. The rifting crisis included, tectonic, magmatic, and volcanic events in the forms of fault slip, dike intrusions, and eruptions, respectively [Figure 1.2]. This rifting episode provides us a unique

opportunity to study the individual roles of tectonic and magmatic processes that occur in an active, immature continental rift.

We assess strain accommodation on the southern portion of the Natron Fault in response to the 2007-2008 activities by calculating both Coulomb stress changes for the rifting episode's six distinct stages [events A-F, Figure 1.2] following Biggs et al. [2013], both cumulatively and for individual events. We use Coulomb 3.4 [Lin and Stein, 2004, Toda et al., 2005] to model the Coulomb stress changes and expected fault motions. Unlike previous studies of the Natron Rift, we include the southern portion of the Natron Fault in our modeled study area and quantify the static Coulomb stress changes on this portion of the fault. In addition to the Coulomb stress calculations, we model the normal and shear (strike-slip and dip-slip) components to assess the style of fault motion promoted, similar to previous studies that investigate the 1989 M6.9 Loma Prieta earthquake [Stein, 1999] and the 1992 M7.4 Landers earthquake [King et al., 1994, Stein et al., 1992]. In these previous studies, however, the focus is on stress transfer from faulting rather than diking and magma chamber inflation/deflation. A recent study on the role of a dike intrusion's influence on a border fault was conducted by Wauthier et al. [2015], but this study focused on the overall Coulomb stress change and not the individual components (normal and shear) as we do in our study. Seeking to resolve triggering mechanisms on a border fault from magmatic activities is a novel application of Coulomb stress calculations [Stein et al., 1997].

Here, we aim to unravel the potential trigger for the fault slip detected with GPS on the Natron border fault. We focus on ~35 km of the southern portion of the Natron Fault; dividing it into two sections referred to as 'volcano adjacent' and 'basin adjacent' for clarity. We detail the Natron Fault's response to the rifting episode due to the difference in proximity to Ol Doinyo Lengai. We resolve left-lateral strike-slip on the 'basin adjacent' section of the Natron Fault with Global Positioning System (GPS) data collected in 2008 [Calais, 2008a].

We use the data in conjunction with our calculated Coulomb, shear, and normal stress change results to compare the effects and response on the Natron Fault. Setting a Coulomb stress change threshold for triggering fault slip following Hamling et al. [2010] at ∼0.1 MPa, we test what events produced significantly positive Coulomb stress change. Overall, our results show that the range of magma-tectonic events that occurred during 2007-2008 rifting episode have different unclamping potential on the Natron border fault. We also present evidence that stress field perturbations caused by intrusive activity may have triggered fault slip in an immature continental rift setting. This work indicates that magmatically induced stress perturbations have the potential to trigger slip on rift border faults that could be strike-slip, and that the proximity of magmatic activity may affect occurrences of slip on adjacent border faults.

1.2.1 Study Area

Because the Eastern branch of the EARS is considered to be magma-rich, it is an ideal place to study continental rifting due to the close proximity of active tectonics, magmatism, and volcanism in immature stages of rifting [Corti, 2012, Karson and Curtis, 1989, Koptev et al., 2015]. The Natron Fault modeled here is the major western border fault of the Lake Natron basin located in the southern part of the Gregory Rift of the EARS [Figure 1.1B]. The border fault extends from the southern portion of Lake Natron to the dormant volcano Kerimasi [Sherrod et al., 2013] and is hypothesized to extend to a depth of ∼15 km [Weinstein et al., 2017]. We divide the Natron Fault included in our study into two sections: one section is adjacent to Ol Doinyo Lengai, and the other section extends further north approximately 20 km (Figure 1.1B). These sections are referred to as 'volcano adjacent' and 'basin adjacent', respectively.

The active carbonatite volcano, Ol Doinyo Lengai, is also located in the southern Gregory Rift region adjacent to the southern, 'volcano adjacent' section of the Natron border fault [Figure 1.1B]. In the past few decades, Ol Doinyo Lengai experienced periods of eruptions that lasted multiple years producing ash emissions and lava flows [e.g. Venzke, 2013]. These eruptions are accompanied by seismic activity in the region, and in the case of the most recent rifting sequence, magmatic intrusions as well [Calais et al., 2008]. Temporary deployments of episodic GPS sites in the surrounding region, prior to January 2008, have been used to study the kinematics of the southern Gregory Rift and indicate divergence at a rate of ∼3 mm/yr [e.g. Fernandes et al., 2013, Saria et al., 2013, 2014, Stamps et al., 2008]. We use data at one of the semi-continuous GNSS/GPS stations deployed on a volcanic lava flow positioned on the flank of the Natron Fault, NGRS [Calais et al., 2014a] [replaced by Engaresero, ENGC, Figure 1.1B, Calais et al., 2014b], to constrain normal movement of the Natron Fault after the 2007 diking event.

1.2.2 2007-2008 Rifting Episode

A prime example of the occurrence of magmatic activity coinciding with tectonic events was observed during the 2007-2008 Northern Tanzanian rifting episode with GPS measurements, InSAR images, and a distant seismic network [i.e. Albaric et al., 2010, Baer et al., 2008, Biggs et al., 2009, Calais et al., 2008]. The 2007-2008 rifting episode was composed of dike intrusions, magmatic reservoir deflations, and tectonic slip that were observed geodetically in the southern Gregory Rift. The onset of the rifting episode began with seismicity on the Gelai Fault observed from 14-16 July 2007 [Albaric et al., 2010], which was composed of a M_w 5.7 earthquake followed by the subsequent adjacent dike intrusion on 17 July 2007. The main Gelai diking event was followed by additional earthquake swarms and continued dike inflation for several months. Soon after the onset of the earthquake swarm, magma reservoir

deflation began beneath the flank of the historically inactive Gelai volcano adjacent to the Gelai Fault (July-September 2007) [Biggs et al., 2009, Calais et al., 2008]. Near the end of the reservoir activity at Gelai in 2008, the volcano Ol Doinyo Lengai underwent an increase in eruptive activity with confirmed ash emissions [e.g. Venzke, 2013]. This eruption was accompanied by a smaller dike intrusion sourced from Ol Doinyo Lengai and magma reservoir deflation at Ol Doinyo Lengai inferred from best-fit models derived from an InSAR inversion [Figure 1.1B, Biggs et al., 2013]. While magma continued to intrude in the region, Ol Doinyo Lengai experienced increased activity with eruptions reaching VEI = 3 [e.g. Venzke, 2013] and experienced a shift in composition from carbonatite to more silicic eruptions [Fischer et al., 2009].

1.2.3 Previous Work

The 2007-2008 Natron rifting event has provided opportunities to study immature continental rifting processes. These processes were addressed by several authors [Table 1.1] due to observable geophysical signals produced, which is not common in immature rifts. Ebinger et al. [2013] suggest slip on faults during early stages of continental rifting is embedded in thick lithosphere and occurs at the detection limits of geodetic observations. The 2007-2008 Tanzania rifting event, however, caused deformation and seismicity that was clearly observable with InSAR [i.e. Baer et al., 2008, Biggs et al., 2013], a temporary seismic network SEISMO-TANZ'07 [Albaric et al., 2010], and an episodic GPS site measured in 2006 and again in 2008 [Calais et al., 2008]. These previous studies provide insight into the geometry of deformation sources and the evolution of the rifting events in 2007-2008 [Albaric et al., 2010, Baer et al., 2008, Biggs et al., 2009, 2013, Calais et al., 2008].

Our study utilizes geometry and inversion results from the aforementioned previous studies of the 2007-2008 Tanzania rifting episode to create our forward Coulomb models. It is important to understand what assumptions were made in the previous studies so that we can assess how the various model parameters influence the Coulomb stress change calculated in each model [Table 1.1]. For each study published, there are differences in the data collected/used due to availability of data at the time and assumptions made on data quality. Three groups of authors studied the 2007 rifting event sequence [Baer et al., 2008, Biggs et al., 2009, Calais et al., 2008] or 2007-early 2008 sequence [Biggs et al., 2013]. Each group of authors performed inversions on interferograms to infer the best-fitting displacement models representing the sequence of deformation events in the rifting episode. Our study follows the Biggs et al. [2013] model due to the inclusion of the intrusive and magmatic activity at Ol Doinyo Lengai in 2008. Therefore, we can investigate the response of the Natron Fault's southern portion to the 2007-2008 rifting activities, and compare our results to the semi-continuous ENGC GPS data [Calais, 2008a, Figure 1.1B].

1.3 Methods

1.3.1 Coulomb Stress Changes

Coulomb 3.4 [Lin and Stein, 2004, Toda et al., 2005] is software used for static stress analysis. It is able to calculate regional stresses and Coulomb stress changes on specific receiver fault(s) in response to tectonic (e.g., faulting) or magmatic events (e.g., diking, magma reservoir deflation). This open source Matlab code provides the capability to design experiments with user-defined faults as tensile and shear dislocations, as well as, other simple magmatic geometries as volumetric sources embedded in an elastic, homogeneous and isotropic half-

space. Using Coulomb 3.4, we are not able to account for viscoelastic relaxation over time. However, since all events occurred within a time span of less than 1 year, we assume these effects are negligible. We use Coulomb 3.4 to calculate the stress resolved on faults and use the Coulomb failure hypothesis to determine if slip would be possible. The Coulomb fault failure hypothesis states that a positive Coulomb stress change brings a fault closer to failure while a negative Coulomb stress change inhibits fault slip for a specified fault rake direction. Equation 1 shows the Coulomb failure equation that is used to calculate the Coulomb stress change with $\Delta\sigma_f$ = Coulomb stress change, $\Delta\tau_s$ = shear stress change (strike-slip and dip-slip components), $\Delta\sigma_n$ = normal stress change, and μ = fault friction coefficient:

$$\Delta\sigma_f = \Delta\tau_s + \mu\Delta\sigma_n \tag{1.1}$$

For our Coulomb stress change analysis, we choose to not specify a rake for the Natron Fault allowing all possible motions. This type of Coulomb analysis is known as the optimized Coulomb stress change. The optimized Coulomb stress change is found by calculating the maximum Coulomb stress change value on a singular fault element. This maximum value is chosen using a 0.1 degree grid search rotating from 0° to 180° and 0° to -180° covering all possible rake directions. We set a Coulomb stress change threshold for triggering fault slip following Hamling et al. [2010] at the value of ∼0.1 MPa. With this approach, the optimized Coulomb stress change produces rakes that indicate fault slip direction and individual stress components.

Following Biggs et al. [2013], we include the stages as follows: (A) Initial 0.4 m of slip on the Gelai Fault from 12-17 July 2007; (B) Additional 0.5 m of fault slip on the Gelai Fault, 0.8 m dike opening, and 0.09 km^3 volume decrease in magma reservoir around Gelai

from 17-21 July 2007; (C) Additional 0.7 m dike opening around Gelai from 21-23 July 2007; (D) Further, 0.8 m dike opening coincides with an additional 0.08 km^3 magma chamber deflation at Gelai from 23 July - 23 August 2007. In addition to these events at Gelai, we model events at Ol Doinyo Lengai as follows: (E) intrusion of a 0.45 m-wide, SE-striking dike beneath Ol Doinyo Lengai from October - December 2007; and (F) A magma reservoir deflation of 0.03 km^3 under Lengai at ~3 km depth from February - September 2008. This information is provided in Table 1.2 and in the timeline provided in Figure 1.2.

We first choose to model the events cumulatively to assess the total Coulomb stress changes transferred to the Natron Fault during the 2007-2008 rifting events (A-F). To further investigate the Coulomb stress changes and to understand how the individual events in 2007-2008 affected the Natron Fault, we model the Coulomb stress changes from each of the individual events as well. Finally, to understand the style of motion expected on the Natron Fault, we model the components of the Coulomb stress changes, including the normal and shear (strike-slip and dip-slip) components.

Following Toda et al. [2005] and Biggs et al. [2013], we use the following material properties: Young's modulus (λ) = 50 GPa, Poisson's ratio (ν) = 0.25, and a fault friction coefficient (μ) = 0.4. In contrast to other studies of the 2007-2008 Tanzania rifting episode, we include the southern portion of the Natron Fault in our model as the primary receiver fault divided into the 'volcano adjacent' and 'basin adjacent' fault sections. We define the fault as dipping 50° east as an average value from field measurements by Sherrod et al. [2013] and project down to 15 km depth. Our model input files, including geometry and parameters for different stages, are available as .inp files in the supplementary information (Datasets S1-S3). We also include the associated outputs and descriptors of the fields (Datasets S4-S6).

To gain a better understanding of the uncertainties between the models and to aid in the interpretations of our calculations, we quantify the average differences between the

existing studies listed in Table 1.1. We perform this process only for comparable events in the previous studies performed on the 2007-2008 Tanzanian rifting episode, which is the initial slip on the Gelai Fault that caused the M_o 5.7 earthquake on 17 July 2007. This differencing process provides constraints on the uncertainties that propagate into our Coulomb stress change models [Figure 1.5] calculated on the Natron Fault. We find uncertainties for this first event range from <0.02 - 0.03 MPa, with values exaggerated on the surface due to the model's mix of tapered and non-tapered faults. With only one comparable event however, the result provides minimal constraints on the uncertainties between previous models.

We implement another strategy to further aid in understanding the uncertainties associated with our models and to test the robustness of our Coulomb stress change results. We create end-member models of each distinct event and employ variable fault dip and Young's moduli taken from values in previous studies [Baer et al., 2008, Biggs et al., 2013, Calais et al., 2008]. These values were chosen from the minimum/maximum material parameters [Table 1.1] and the minimum/maximum field dip measurements according to Sherrod et al. [2013] (main map: along strike dip measurements). We also vary the fault friction coefficient from $\mu = 0.3$ to $\mu = 0.5$, fault dip direction from 50° to 80° east, and Young's moduli from $\lambda = 30$ GPa to $\lambda = 50$ GPa. We find that the differences of Coulomb stress changes between end member models are negligible on the Natron Fault (<0.002 MPa) and stress change patterns are consistent.

1.3.2 Geodetic Observations

In addition to modeling the Coulomb stress changes, we present newly processed GPS time-series with daily positions from the Engaresero [Calais, 2008a, ENGC,Table 1.1,Table 1.3], Lwondolwo [Calais, 2008c, LDWC], and Ketumbeine [Calais, 2008b, KETC] semi-continuous

GPS sites available in the region during 2008. We use the processing software GAMIT/-GLOBK [Herring et al., 2016] to calculate the daily position solutions from doubly-differenced GPS phase observations spanning January 6 – August 15, 2008 with tropospheric zenith delay parameters set every 2 hours. We apply corrections for solid Earth tides, polar tides, and ocean loading from the International Earth Rotation Services following Saria et al. [2014].

ENGC, LDWC, and KETC were part of a semi-permanent deployment of GPS sites installed in January 2008. In our results, we only present the Engaresero continuous GPS site ENGC for several reasons. First, ENGC records the motion on the Natron Fault due to its position on the footwall of the 'basin adjacent' region of the Natron border fault. Second, we can interpret the GPS signals to be associated with tectonic processes rather than ground slumping or soil compaction since the station is installed on a stable ignimbrite flow on the footwall. Third, data at all three sites span the magma reservoir deflation event at Ol Doinyo Lengai [event F, Table 1.2], but we find insignificant motions at LDWC and KETC [Figure 1.4]. Finally, ENGC detects displacement in the north and east components on ∼30 January 2008.

We have included all timeseries available submitted as .pos files [Dataset S7-S9]. We also include in our supplementary information a re-processed InSAR interferogram from two ENVISAT passes in 2008 (18 February 2008 – 15 September 2008) after the initial rifting events of 2007 [Figure-S5]. This interferogram presents the broader deformation active in the Natron rift during the activity at Ol Doinyo Lengai with complex signals on the southern portion of the Natron Fault however, the interferogram does not show clear line-of-sight displacement on either section of the fault. These passes overlap with our ENGC GPS observations, but not with the displacement detected at ENGC on ∼30 January 2008 on the 'basin adjacent' section of the Natron Fault. Due to this gap in timing and lack of signal clarity, we do not include the interferogram in our discussion.

1.4 Results

1.4.1 Geodetic Observations

We first present in Figure 1.3 the newly processed GPS timeseries to show the response of the Natron Fault from 6 January - 15 August 2008. This timeseries contains evidence of fault slip on the Natron fault in the form of a distinct offset in the southeast direction occurring on ∼30 January 2008. The offset is consistent with the left-lateral slip due to the positioning of ENGC on the rift flank (footwall). This slip occurred between event E (Lengai dike intrusion) and event F (Lengai chamber deflation; Table 1.2). The timeseries shows displacement in the southern direction at ∼ 1.2 cm ± 0.3 cm and in the east direction at ∼1.8 cm ± 0.7 cm [Figure 1.3]. The noise and uncertainties in the vertical component are larger than the north and east components so millimeter scale displacements are not observable in the timeseries [Figure 1.3]. Again, Figure 1.4 shows that our processing found insignificant motions at LDWC and KETC in comparison with ENGC.

1.4.2 Coulomb Stress Changes

In Figure 1.5, we present calculations of cumulative optimal Coulomb stress changes on the 'volcanic adjacent' and 'basin adjacent' sections of the Natron Fault that encompass the 2007-2008 events, including the intrusive activity beneath Ol Doinyo Lengai published in Biggs et al. [2013]. This figure presents the evolution of the Coulomb stress changes cumulatively (for all events) over time on the Natron Fault with the Coulomb stress changes from each event summed. Our results indicate that Natron Fault undergoes a positive Coulomb stress change on both sections of the fault for depths ∼0-8 km for all cumulative events. On the 'basin adjacent' section, where the site ENGC is located, there is a negative Coulomb stress

change that ranges from -0.5 to -0.1 MPa centered beneath ENGC at ∼12 km depth with a radial pattern. Maximum positive Coulomb stress change values at ENGC are reached during event D (∼0.3 MPa) and the minimum during event A. Coulomb stress changes, on the 'volcano adjacent' section of the fault, are positive at all depths with a maximum occurring at Ol Doinyo Lengai during event F (>0.5 MPa). Only for the first event (A) is the threshold indicative of fault slip not reached, which establishes that enough stress was transferred to the fault over the course of the 2007-2008 events to trigger slip.

To assess how each of the individual stages in the 2007-2008 rifting episode contributed to the cumulative Coulomb stress change on the southern portion of the Natron Fault, we model the events separately using the same six distinct time-frames [Table 1.2]. Results for the isolated time-frames spanning the evolution of the 2007-2008 rifting episode are presented in Figure 1.6. The individual models show that the events cause positive stress changes on both fault sections at shallow depths (<8 km) with the largest magnitude Coulomb stress changes associated with the Ol Doinyo Lengai volcanic deflation (event F). B is the only other event that causes the threshold for slip to be reached at ENGC and the projected Ol Doinyo Lengai volcano. Negative Coulomb stress changes are seen in events A-D centered at ∼10 km depth. As a result of the Ol Doinyo Lengai dike (event E), a small area of negative Coulomb stress change is observed on the 'volcano adjacent' section between ∼8-11 km beneath the projected Ol Doinyo Lengai volcano. After the Ol Doinyo Lengai magma chamber deflation (event F), negative Coulomb stress changes extend from ∼10- 15 km deep from the southernmost 'volcano adjacent' section to the center of the 'basin adjacent' section.

To investigate the style of motion on the Natron Fault, we calculate the normal and shear (strike-slip and dip-slip) components of the Coulomb stress changes for the cumulative

evolution of the six distinct events occurring over 2007-2008 in the Southern Gregory Rift. Results are presented in Figures 1.7, 1.8, 1.9.

For the normal stresses, we follow the convention that positive stress change represents stresses perpendicular to the fault plane that induce "unclamping". The important observation from our normal stress change modeling is that events at Gelai (Figure 1.7; events A-D) clamp the 'basin adjacent' section and unclamp the 'volcano adjacent' section of the fault. We see a similar pattern for the magmatic events at Ol Doinyo Lengai (Figure 1.7; event E and F).

The shear (strike-slip and dip-slip) stress change results are more complex. For the shear stress in the strike-slip direction, we follow the convention that positive shear stresses represent right-lateral (rake = 180deg) stresses. For the first event (A- Initial Gelai slip) and last event (F- Lengai chamber deflation) the stress change found is right lateral slip, but the other events favor left-lateral slip [Figure 1.8]. This result may indicate that, cumulatively, events C-E promoted slip on the 'basin adjacent' section of the Natron Fault because the sense of slip is consistent with the GPS observations at ENGC.

For the shear component in the dip-slip direction we follow the convention that positive values represent stresses in the reverse direction parallel to the fault plane (rake = 90deg). We see that for each event in Figure 1.9 (events A-F) that the 'basin adjacent' portion of the fault under the GPS site ENGC is undergoing a consistent increase in positive stress change in the dip-slip direction to depths of $\sim$10 km. This positive stress change is indicative of dip-slip motion with a reverse sense at shallow depths on the 'basin adjacent' section. Given the rift environment, it is likely that these changes in stress will not exceed the background tectonic stresses, which are normal. Hence, we would not anticipate any dip-slip motion. On the 'volcano adjacent' section, there is a consistent negative shear component in the dip-slip direction, suggesting normal fault motion would be promoted.

1.5 Discussion

Our Coulomb stress results, both for the cumulative and isolated models, show that the 2007- 2008 Tanzania rifting events resulted in positive Coulomb stress changes at shallow fault depths for both the 'basin adjacent' and 'volcano adjacent' sections of the Natron Fault. The positive cumulative Coulomb stress changes pass the minimum threshold of 0.1 MPa that we have set for triggering fault slip [Hamling et al., 2010] in all cumulative events except for the initial fault slip [Figure 1.5A]. For the isolated events, only event B (Gelai activity continued) and event F (Lengai chamber deflation; see Table 1.2) have positive Coulomb stress changes greater than our threshold near ENGC [Figure 1.6]. At the projected Ol Doinyo Lengai location on the "volcano adjacent" fault section, event B (extended Gelai activity), event D (Gelai magmatic activity), and event F (Lengai chamber deflation) pass the threshold. These results suggest that the Natron Fault experienced significant changes to its stress state resulting from the sequence of magmatic and volcanic events. We note that the events at Ol Doinyo Lengai [Figure 1.5E-F] added additional stress along the Natron Fault.

The slip event observed at ENGC was detected approximately one month after the dike intrusion that was sourced from the Ol Doinyo Lengai magma chamber [Biggs et al., 2013, Figure 1.6E]. Event E (Lengai dike intrusion) could have promoted oblique left-lateral movements based on our shear and normal stress calculations, which is consistent with the observed slip. As noted above, the threshold is reached for triggering fault slip at Event E when considering the cumulative effects of events A-E. This interpretation implies that slip on a border fault could occur up to 20 km from diking or volcanic events. Alternatively, another, geodetically undetectable diking event may have occurred after the observed dike intrusion at Ol Doinyo Lengai during the time-frame of our geodetic observations, which would be consistent with InSAR as well [Biggs et al., 2013].

Individually, Event E is below our Coulomb stress change threshold for triggering fault slip [Hamling et al., 2010, 0.1 MPa]. Previous studies of more mature continental rifting regions where tectonic-magmatic interactions exist in the center of the rifts away from border faults [Rubin and Pollard, 1988, i.e. Ethiopia] suggest that small perturbations ≤ 0.01 MPa caused by intrusive activity could form a positive feedback with seismic activity to promote slip. However, there was no seismically detectable event on the Natron Fault during the time period of the GPS detected slip [Ekström et al., 2012, NEIC catalog]. Nostro et al. [1998] find that a Coulomb stress change of $\sim$0.008 – 0.018 MPa resulting from magmatic activity can promote tectonic events depending on the geometry of the magma chamber and proximity to the fault. Based on our cumulative models, we also observe that when the Ol Doinyo Lengai dike intrusion occurred, pre-stress may have already been provided by the initial events at Gelai. In addition to this stress, there are tectonic stresses from gravitational potential energy gradients and mantle traction on the order of 12-15 MPa acting on the region [Stamps et al., 2014]. Therefore, the small Coulomb stress change perturbation associated with the isolated diking event at Ol Doinyo Lengai may have only been sufficient to trigger and not drive the slip event observed at ENGC. A more recent study in the Southern Gregory rift also suggests local seismicity could be triggered by a change in stress state around magma bodies and dike intrusions based on a dense network of seismic instruments deployed in 2013 – 2014 [Weinstein et al., 2017].

There are minimal studies about the fault kinematics of strike-slip motions in rifts, although strike-slip faulting has been documented in several rift locations: Kenya Rift [Doser and Yarwood, 1991], Iceland [Green et al., 2014], and the southern Afar [Tapponnier et al., 1990]. Green et al. [2014] attribute the strike-slip faulting to bookshelf faulting, as does Tapponnier et al. [1990], but they also suggest block rotation plays a role. Ring et al. [1992] proposed a change in stress orientation at 2 Ma across the EARS that caused strike-slip

motions to be favored along border faults in the Malawi Rift of the EARS. In this study, we find a potential mechanism for magmatic activities that could have implications similar to the northern Malawi Rift where there is strike-slip faulting near the local Rungwe volcanic province. Instead of a regional stress change, slip that is temporally close with volcanism is another mechanism that could trigger strike-slip faulting in rifts.

Other mechanisms that could explain slip at ENGC involve degassing and magmatic fluids. Carbon and helium isotopic analyses from sites on the Natron Fault and thermal springs were recently collected by Lee et al. [2016, 2017]. Together, these two studies provide an alternative to fault slip triggering due to Coulomb stress changes and hypothesize that a deep-seated magma chamber uses regional faults to transfer CO2 rich fluids to the surface, which can weaken faults. Similar to Coulomb stress changes, degassing events accompany active volcanism and may trigger co-eruptive fault slip. Co-eruptive fault slip associated with magmatic fluids can also weaken faults [Roecker et al., 2017]. The role of magmatic fluids in immature rifting relies on a favorable setting, such as weak or critical state border faults, and close proximity of magmatic activity. In the southern Gregory Rift, the Natron Fault satisfies these factors with Ol Doinyo Lengai adjacent to the fault (<1 km east) and the existence of far-field extensional tectonic forces present in the Southern Gregory Rift such that the Natron Fault is in a critical state [Heidbach et al., 2010, Stamps et al., 2010, 2014].

1.6 Conclusion

In conclusion, our models of the cumulative Coulomb stress change for the 2007-2008 rifting events results in changing the state of stress on the southern portion of the Natron Fault enough to trigger slip on both the 'volcano adjacent' and on the 'basin adjacent' section of

the Natron Fault. The Coulomb stress change models for the diking event sourced from Ol Doinyo Lengai agree with the oblique left-lateral slip derived from the GPS data. We isolate the 2007-2008 Tanzanian rifting events at Gelai and Ol Doinyo Lengai to identify if a singular event could have triggered the recorded displacement by ENGC on the Natron Fault. These isolated Coulomb stress models indicate a positive Coulomb stress change exists in all events at low magnitudes except the initial slip (Event A) and that, the majority of the events in 2007-2008, pass the threshold set at 0.1 MPa for triggered slip. However, when quantifying the shear (strike-slip and dip-slip) and normal stress changes, we observe that normal fault motion was prohibited due to compressive stresses. This could explain why we see SE strike-slip motion in the GPS data. We also observe that the change in the Coulomb stress is an order of magnitude greater when we include the magmatic events at Ol Doinyo Lengai. These Coulomb stress change results suggest that the displacements on the 'basin adjacent' section Natron Fault may have been placed in a weakened or critical state by the Coulomb stress changes $\geq$0.1 MPa from the 2007-2008 magmatic and tectonic events. In particular, the recorded slip on $\sim$30 January 2008, after the initial 2007 events, was possibly triggered by the Lengai dike intrusion with only a small stress perturbation needed for triggering slip on the critically stressed Natron Fault.

In the broader framework of continental rift initiation, this work shows that transient magmatic processes are important to rifting and may have a larger effect earlier than previously thought. We present evidence that, in an immature continental rift setting, these small Coulomb stress perturbations from magmatic activity affects and may trigger slip on an adjacent border fault from ($<$1 km) to a distance of fault extension up to $\sim$20 km away where we detected slip at ENGC. We suggest the magma intrusion and eruption at Ol Doinyo Lengai provides the primary source of the positive Coulomb stress change on the 'basin adjacent' section of the Natron Fault. This work indicates that volcanism in early stages of

rifting affects the occurrence of individual slip events along a fault with more events and more slip occurring on the fault closest to the active volcano.

1.7 Acknowledgments

Materials in this work are based on data and equipment services provided by the UNAVCO Facility with support from the National Science Foundation (NSF) and National Aeronautics and Space Administration (NASA) under NSF Cooperative Agreement No. EAR-0735156. Specific datasets discussed and/or used for NGRS, ENGC, KETC, and LWDC are cited in the References section and are associated with the NSF grants No. EAR-0801801 and No. EAR-0538119. JB was supported by NERC grant RiftVolc:NERC NE/IO1372X/1 for her contributions. We are grateful for the efforts of the International GPS Service for providing data products and access to publicly accessible GPS data. Figures were made with Generic Mapping Tools v5.2.1 supported by the NSF (ftp://ftp.iris.washington.edu/pub/gmt/legacy/). GAMIT/GLOBK used in processing is a GPS processing software is available at (http://www-gpsg.mit.edu/ simon/gtgk/index.htm). The raw GPS data used are available through the UNAVCO data archive at (http://www.unavco.org/data/gps-gnss/data-access-methods/dai2/app/dai2.htr We produced the .pos files, which are are available in the supplementary material. Model files are also provided for reproducability as .inp files in the supplement. We thank Kang Hyeun Ji for input in early versions of this manuscript.

1.8 Tables and Figures

Table 1.1: Table 1. Published work on the 2007-2008 Tanzanian rifting episode that emphasize observable deformation. Details about each study include: (1) publication source, (2) data used for inverting the geometry and slip/opening quantities for the faults and diking events, respectively, (3) the time periods data was collected, (4) the results of inversions, and (5) the general results/outcomes of each previous study.

Model	Data Used	Time Period of InSAR Data	Inversion Results	Conclusions
Baer et al. [2008]	Envisat and ALOS-1	1-29-07 to 10-17-07	Fifteen tapered fault segments Five dike segments No reservoir deflations for Gelai	Inferences that (1) a 15 km deep magma reservoir beneath Ol Doinyo Lengai was pressurized and linked with the Gelai earthquake swarm and (2) Gelai dikes originated from magma reservoir beneath Ol Doinyo Lengai.
Calais et al. [2008]	Envisat and GPS Data	4-07-07 to 8-21-07	Tapered Gelai Fault segment Two tapered normal faults at Gelai One dike segment Two magma reservoir deflations	Comparison to GPS data gave evidence that supported strain accommodation aseismically associated with dike activity. Suggested Gelai dikes originated from a magma reservoir beneath Gelai.
Biggs et al. [2009]	Envisat and ALOS-1	3-05-07 to 8-27-07	Single plane fault Single plane dike One magma reservoir deflation	Describes how the 2007 rifting episode observations connect to the process of individual rifting episodes including the initiation, rate, and relations to volcano magma reservoirs.
Biggs et al. [2013]	Envisat and ALOS-1	3-05-07 to 9-15-08	Single plane fault Single plane dike magma reservoir deflation Lengai dike segment Lengai magma reservoir deflation	Provides supporting evidence that the stress change from Gelai event promoted the Lengai activity. Also suggests different sources for the Gelai and the Lengai magmatic activity.

Table 1.2: Table 2. The six distinct stages modeled from the 2007-2008 Tanzania rifting episode. The division follows the previous work of Biggs et al. [2013].

Letter	Date	Event	Amount	Location
A	12-17 July 2007	fault slip	0.4 m	Gelai Fault
B	17-21 July 2007	fault slip	0.5 m	Gelai Fault
		dike opening	0.8 m	Gelai dike
		magma reservoir deflations	0.09 km^3	Gelai
C	21-23 July 2007	dike opening	0.7 m	Gelai dike
D	23 July 2007 –	dike opening	0.8 m	Gelai dike
	23 August 2007	magma reservoir deflation	0.08 km^3	Gelai
E	October 2007 –	dike intrusion	0.45 m	Ol Doinyo Lengai
	December 2007	Ol Doinyo Lengai sourced		
F	February 2008 –	magma reservoir deflation	0.03 km^3	Ol Doinyo Lengai
	September 2008			

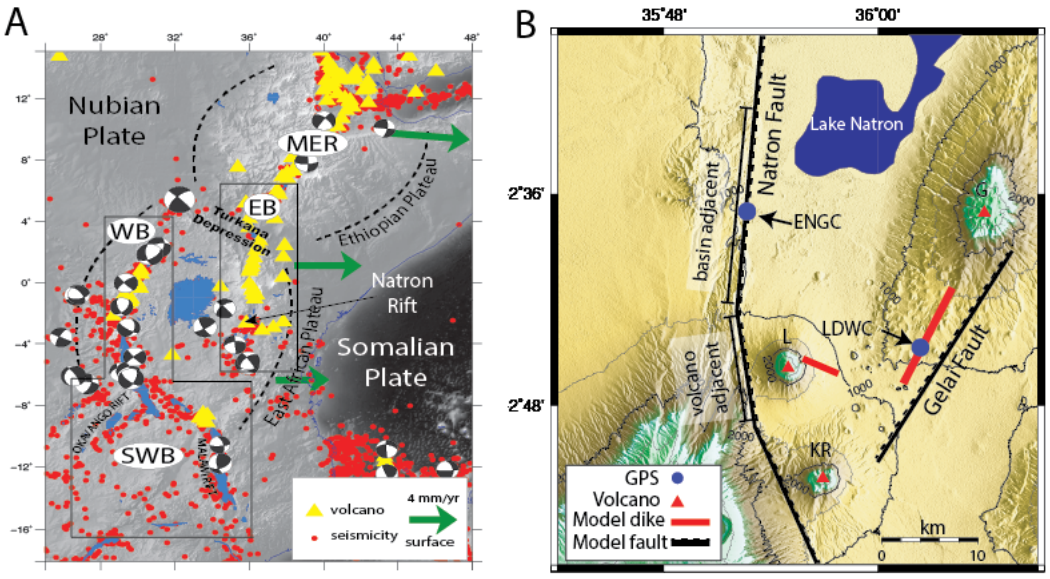

Figure 1.1: A: Map illustrating the southern Gregory Rift (Natron Rift) in relation to the East African Rift System. Yellow triangles represent volcanoes in the region and red dots represent seismicity. The figure also includes strike-slip focal mechanisms from the NEIC [Dziewonski et al., 1981] and vectors representing modeled extension rates from Saria et al. [2014]. B: Simplified tectonic setting of the southern Gregory Rift (Natron Rift) showing the location of the modeled southern portion of the Natron Fault, which is divided into the 'volcano adjacent' and 'basin adjacent' sections. Faults utilized in this study are shown with segmented markers that denote dip direction. The inset map illustrates the southern Gregory Rift in relation to the East African Rift System. The Gelai Fault was the source of the initial slip in 2007. The 2007-2008 diking events are portrayed as red lines. The blue dots represent the semi-continuous GPS sites that collected data in 2008 [Calais, 2008a,b,c]. ENGC and LDWC are the 4-character site names used to identify the GPS. Ol Doinyo Lengai, a Holocene active volcano, is annotated with an L. Gelai, a mid-Pleistocene inactive volcano, is annotated with a G. Kerimasi, another Pleistocene inactive volcano, is annotated with KR.

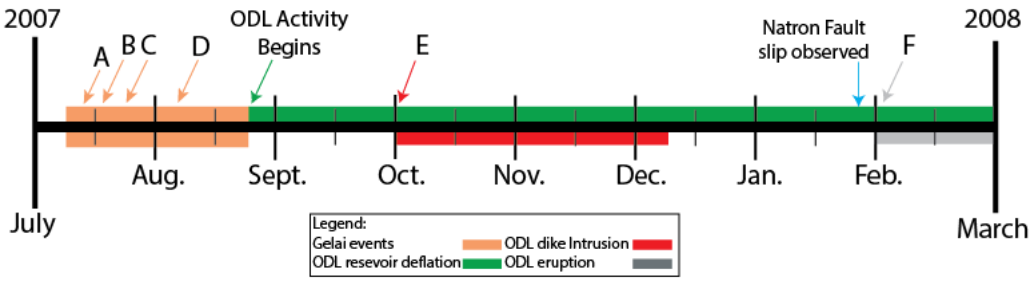

Figure 1.2: This figure is a timeline representation of the events listed in Table 2 that are included in our working model. This timeline also presents other important temporal events that were not able to be modeled including the graben collapse and initial eruptive activity at Ol Doinyo Lengai. The tan line represents the events occurring at Gelai (events A-D). The green line represents the volcanic activity at Ol Doinyo Lengai in relation to the other events. The red line represents the dike intrusion at Lengai (event E) and the grey line represents the explosive eruptive activity that produced a geodetic signal (event F)

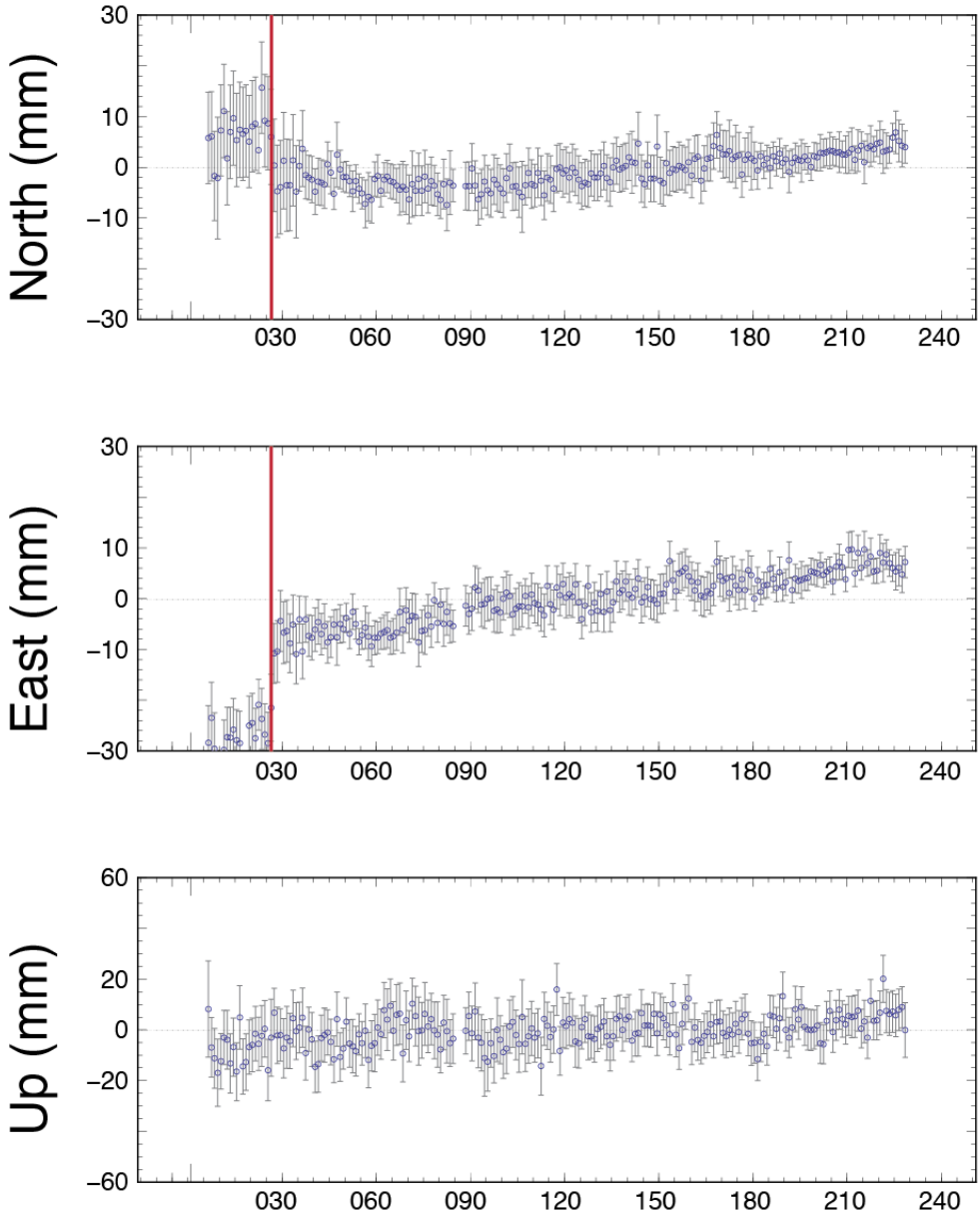

Figure 1.3: The timeseries processed for the Engaresero semi-continuous GPS site ENGC (6 January 6 - 15 August 2008). The X-axis represents time in day of year and the Y-axis represents displacements scaled in millimeters. The error bars are set at 2σ with RMS of 3 mm in the horizontal component and 5 mm in the vertical component. The red line represents the offset in the time-series' horizontal motion occurring ∼30 January 2008. This offset in the timeseries represents ∼1.4 cm of motion to the south and ∼2 cm to the east. There are no visible offsets in the vertical component.

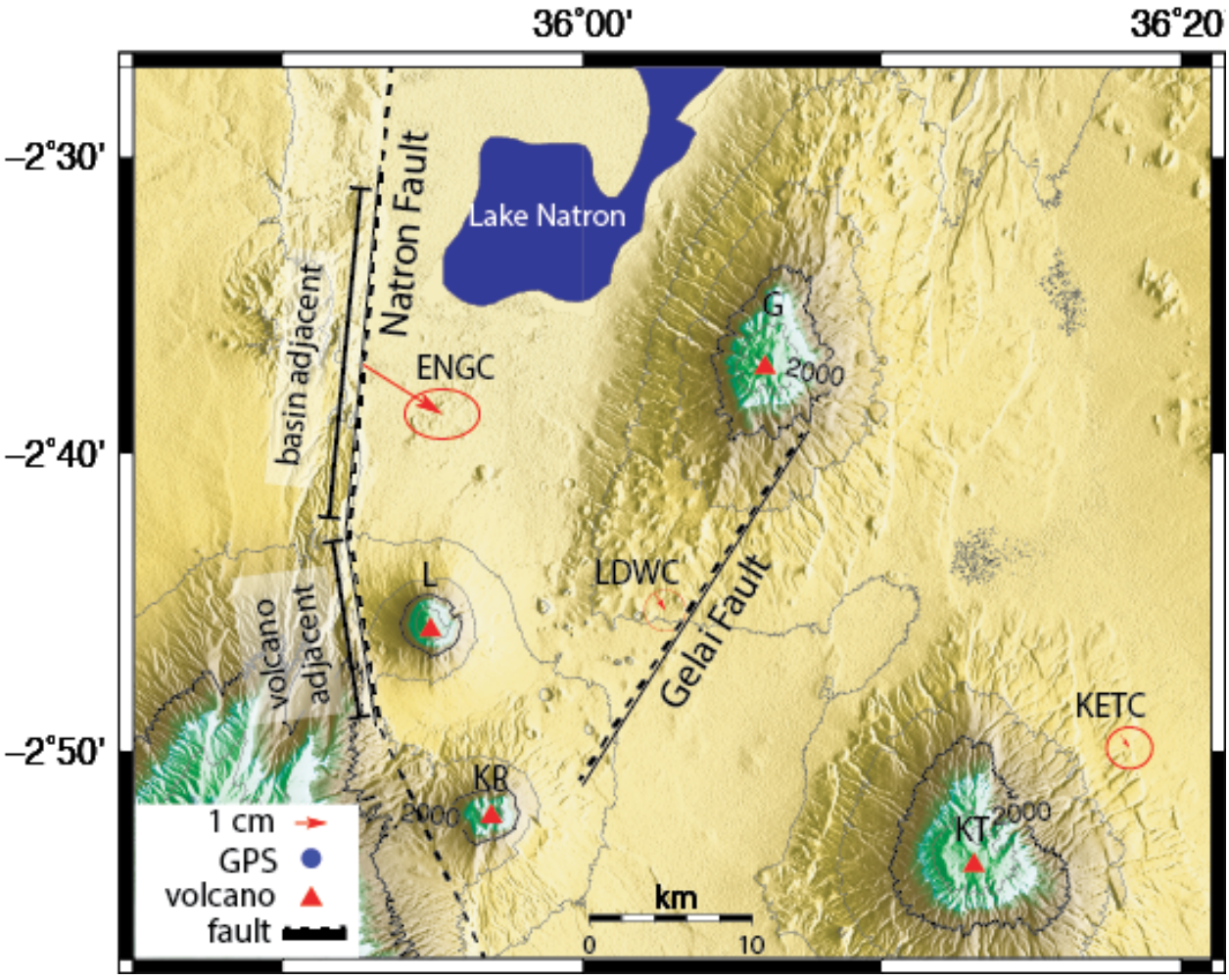

Figure 1.4: Displacements of ENGC, KETC, and LDWC with 95% confidence ellipses. The volcano Ol Doinyo Lengai is annotated with an L, and Gelai with G, Kerimasi with KR, and Ketumbeine volcano with KT. The modeled Natron Fault and Gelai Fault geometries are also shown.

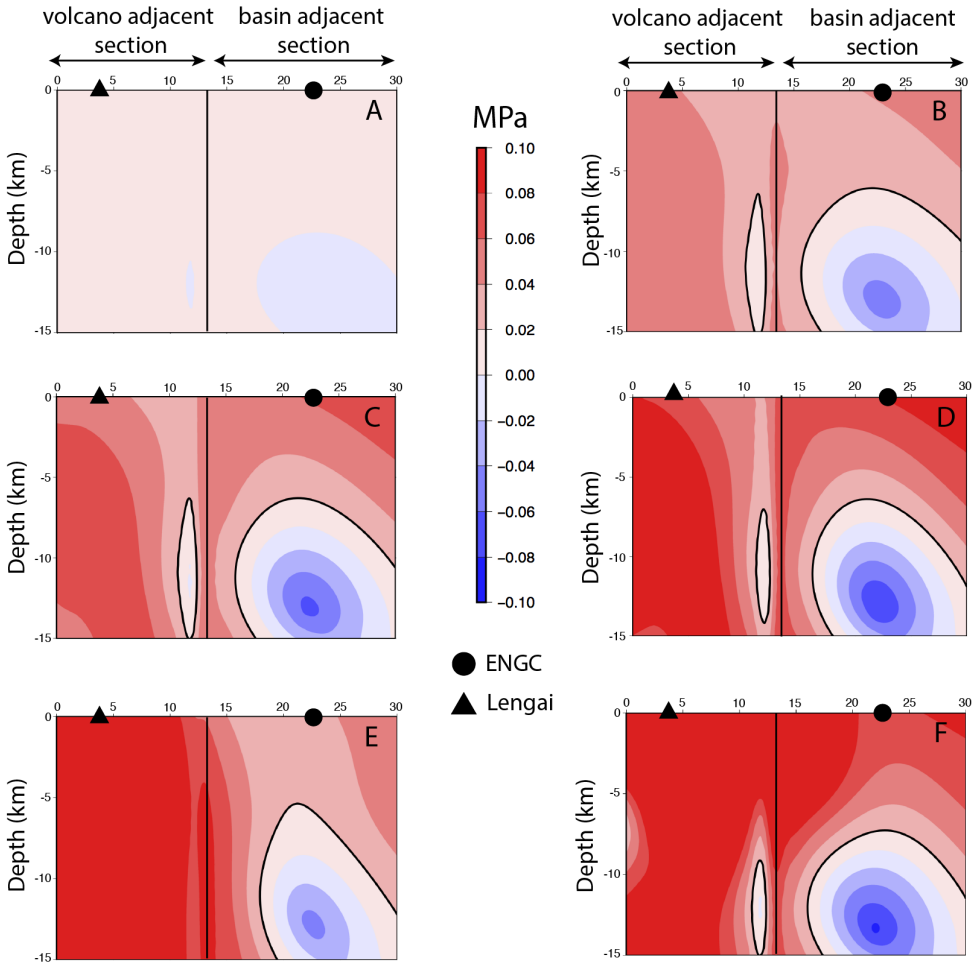

Figure 1.5: Cumulative Coulomb stress change results for the individual events of the 2007-2008 Tanzania rifting episode projected on the 'volcano adjacent' and 'basin adjacent' sections of the southern portion of the Natron Fault. Letters A-F represent the distinct stages of the Tanzania rifting episode following the convention given in Table 1.2. The X-axis is the distance along the fault in km with zero corresponding to the southern edge of the Natron Fault as depicted in Figure 1.1. The Y-axis is distance below the surface projected to a depth of 15 km. The triangle shows the relative location of Ol Doinyo Lengai to the fault, and the semi-circle similarly for ENGC. Warmer colors represent positive stress changes (unclamping) and cooler colors representing negative stress changes (clamping). Dip of the Natron Fault is 50°, depth is set at 15 km, and we use our default model parameters with λ= 50 GPa, ν= 0.25, and μ = 0.4. The 0.1 MPa contour is bolded for clarity.

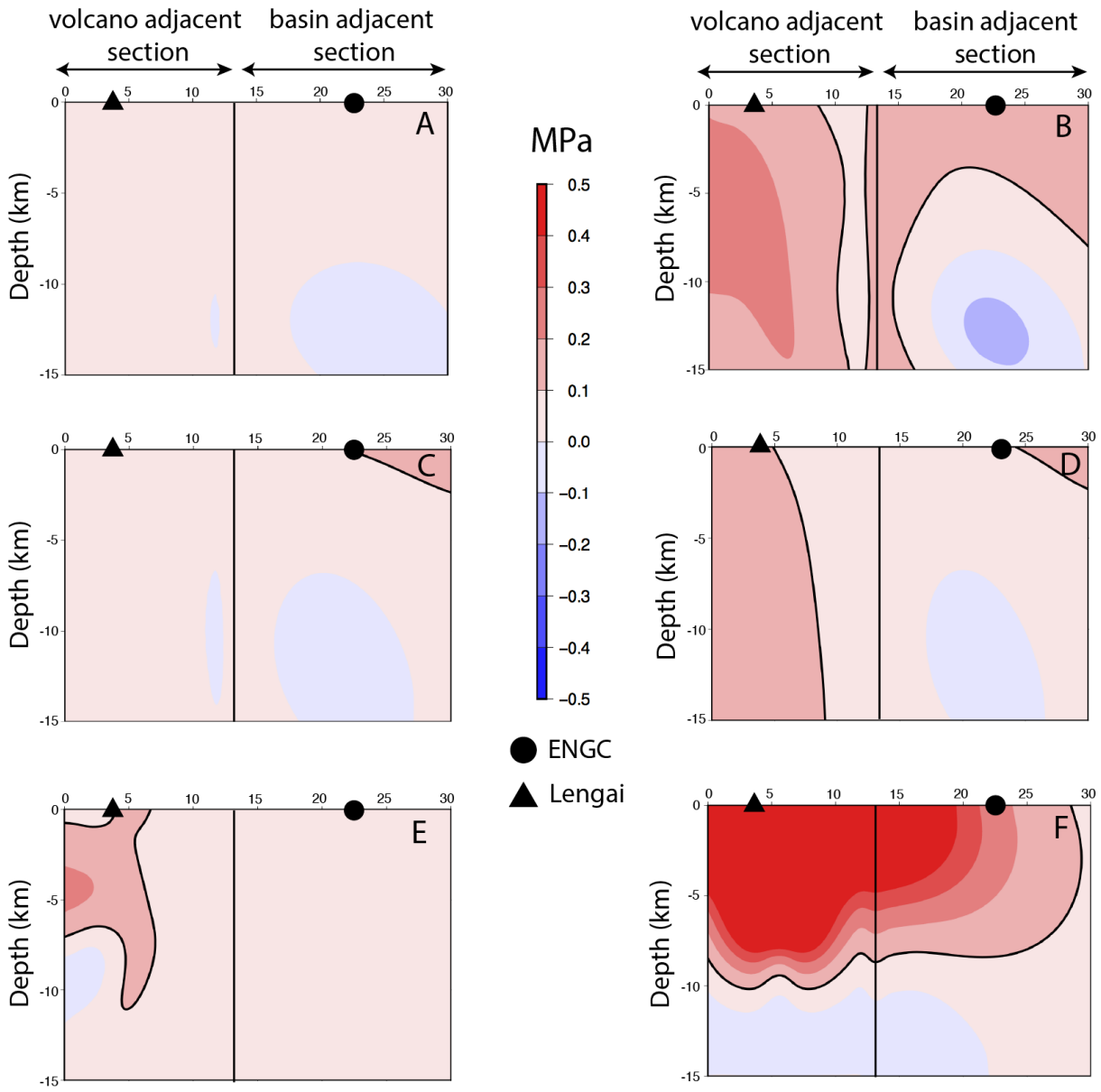

Figure 1.6: Isolated Coulomb stress changes associated with the individual 2007-2008 Gelai events and the 2008 activity at Ol Doinyo Lengai projected onto the southern portion of the Natron Fault (see 1.2). The figure is divided into the six distinct stages after Biggs et al. [2013] (see Table 1.2) and follows the format and convention set in Figure 1.5.

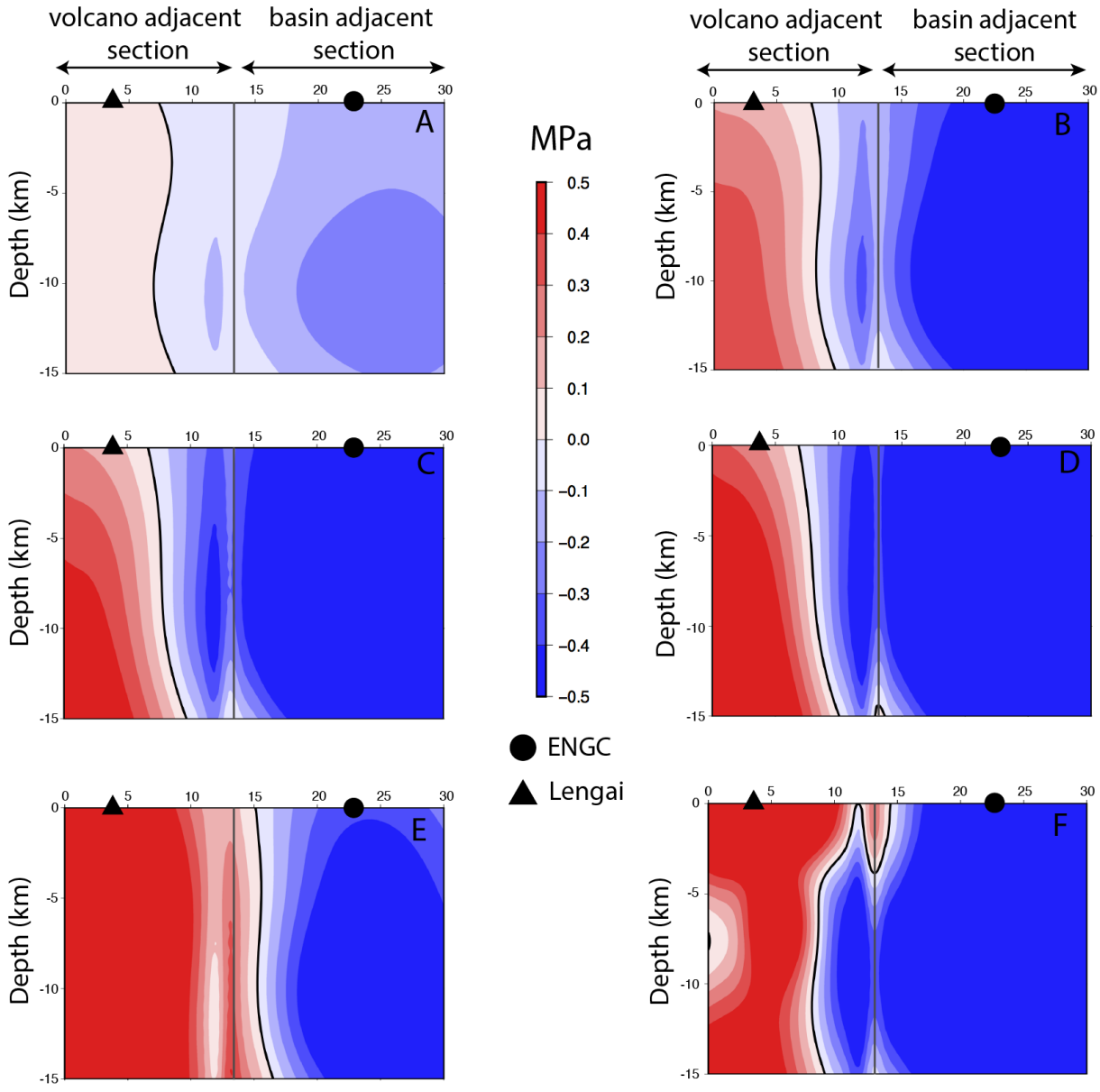

Figure 1.7: The normal stress change of the cumulative evolution associated with the 2007 - 2008 Tanzania rifting crisis projected onto the southern portion of the Natron Fault. The figure follows a similar format and convention set in Figure 1.5 (see Table 1.2). The division between positive and negative normal stress change values are clarified with a bold black line.

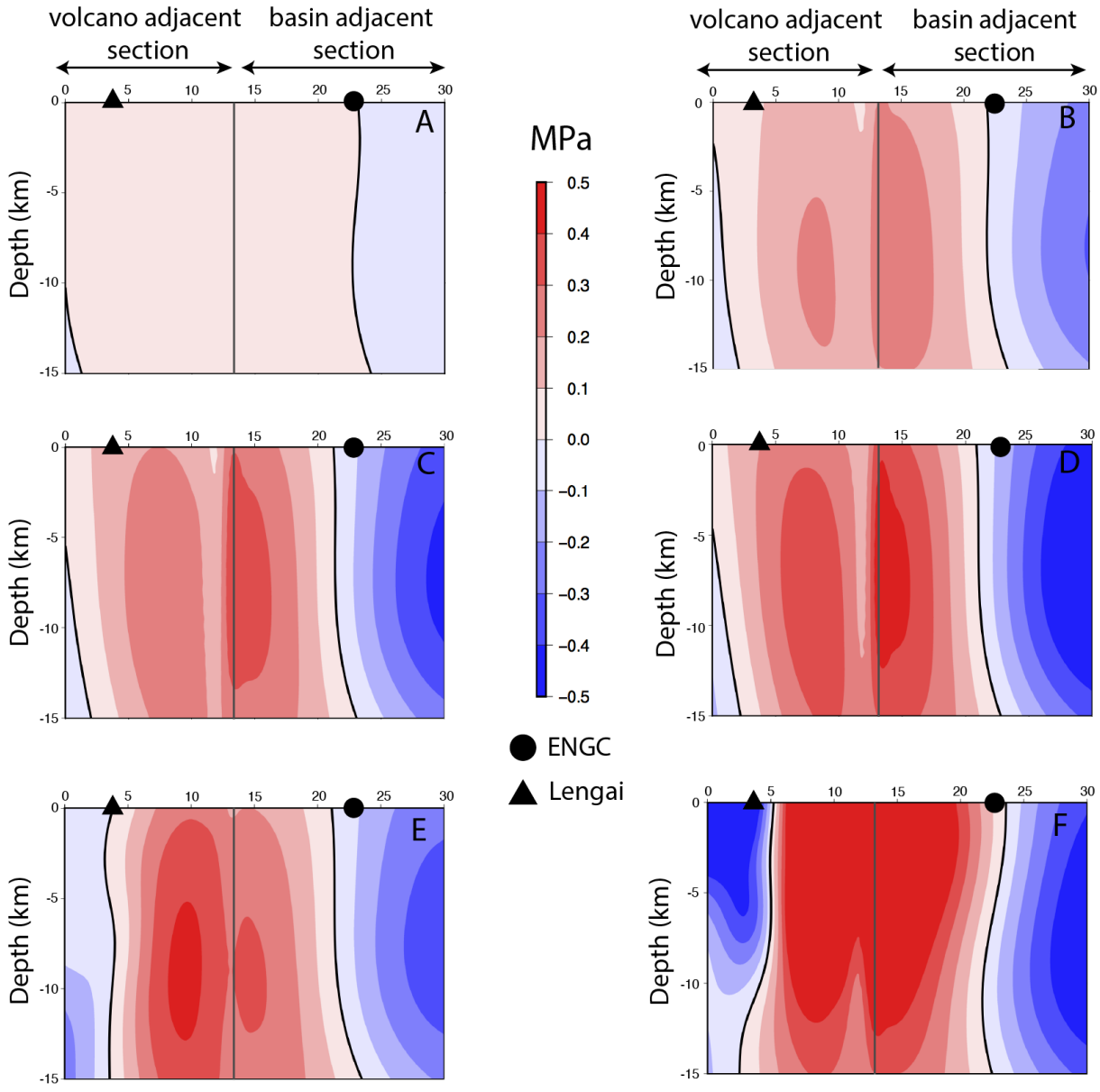

Figure 1.8: The shear component in the strike-slip direction of stress change for the cumulative evolution associated with the 2007-2008 Tanzania rifting event projected onto the southern portion of the Natron Fault. The figure follows a similar format and convention set in Figure 1.5 (see Table 1.2). The division between positive and negative shear stress change values are clarified with a bold black line.

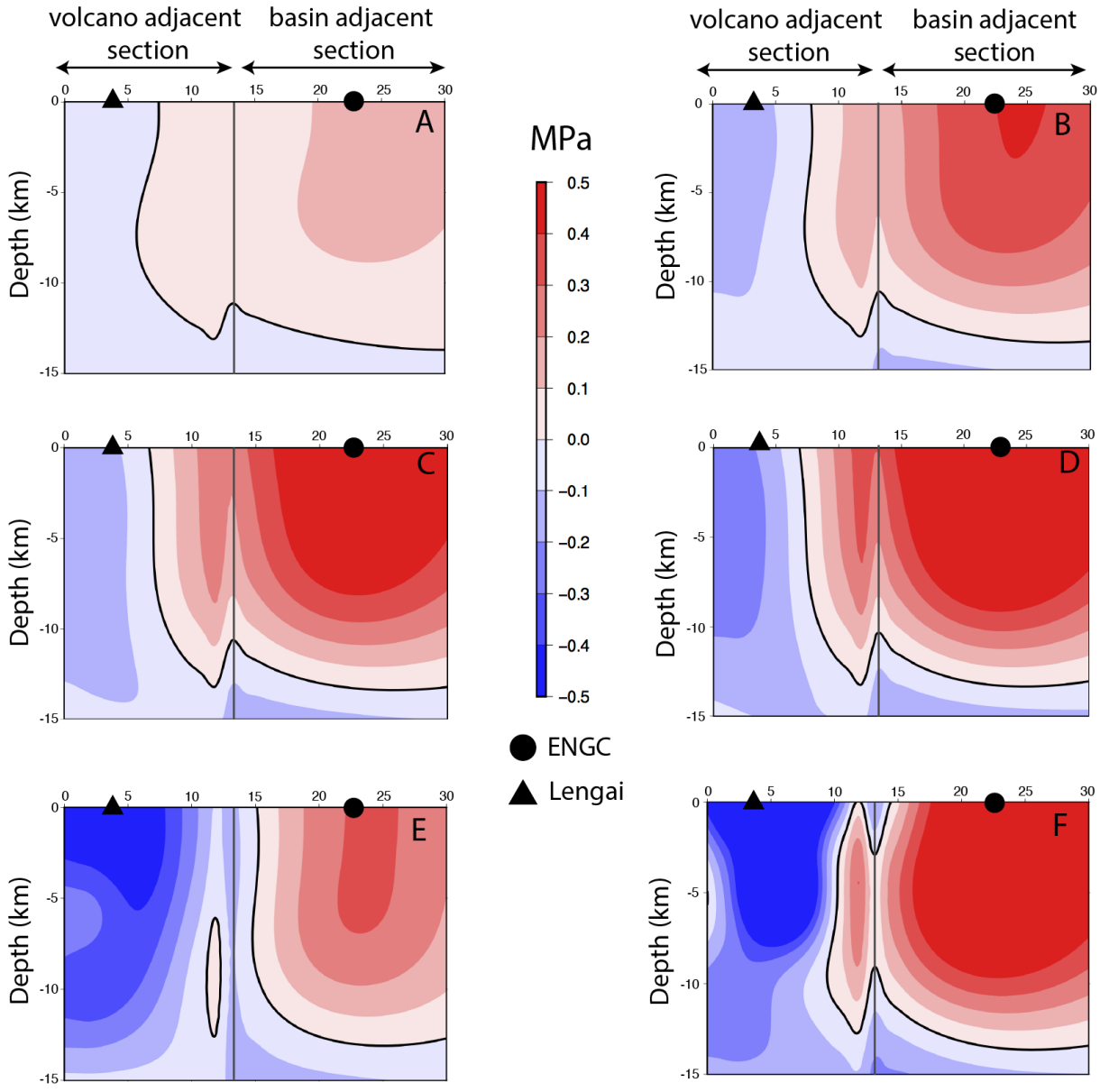

Figure 1.9: The shear component in the dip-slip direction of stress change from the cumulative evolution associated with the 2007-2008 Tanzania rifting crisis projected onto the southern portion of the Natron Fault. The figure follows a similar format and convention set in Figure 1.5 (see 1.2). The division between positive and negative shear stress values are clarified with a bold black line.

Chapter 2

Investigating the effects of topography, heterogeneous crustal composition, and magma reservoir structure on volcano-tectonic interactions in a youthful continental rift

In preparation for submission to the Journal of Geophysical Research.

2.1 Abstract

Previous studies of active volcanic rifts have provided evidence that geochemical and geophysical interactions may influence future magmatic and faulting events. In our previous work, we investigated stress interactions during the 2007-2008 Tanzanian rifting crisis in the Natron Rift and demonstrated that small stress changes (<0.1 MPa) induced by magmatic events could promote slip on a major border fault, the Natron Fault. In this work, we use

the 3D finite element code PyLith to investigate volcano-tectonic interactions in the same region by evaluating stress interactions between the active carbonatite volcano Ol Doinyo Lengai and the adjacent Natron Fault. We test the influence of stress changes on the Natron Fault that are due to a deflating magma reservoir consistent with the most recent VEI 3 eruption that is 3 km beneath Ol Doinyo Lengai. We perform a suite of experiments to test stress changes on the Natron Fault arising from a 1) deflating magma reservoir of various sizes, 2) a system with and without topography, and 3) a system that has homogeneous or heterogeneous crustal density derived from shear wave seismic velocities. Through quantitative comparisons based on percent difference calculations, we find that including topography has a significant effect on the stresses that are imparted on the Natron Fault due to volcano-tectonic interactions, but crustal density heterogeneities and magma reservoir size do not. These results imply simplistic point source models without topography are not sufficient to elucidate the influence of volcanically-induced stress changes on surrounding faults.

2.2 Introduction

Investigations into volcano-tectonic interactions in actively rifting regions have presented evidence that magmatic activity plays a significant role in promoting continental rifting [Bialas et al., 2010, Buck, 2006, Hamling et al., 2010]. This significance has been documented in more detail through research that assesses how active volcanism, dike intrusions, and magma transfer influence stress and strain in regions surrounding magma reservoirs [Gudmundsson, 2012]. A couple of examples specific to actively rifting regions include a dike intrusion that triggered border fault slip through stress transfer in the Kivu Rift of the Western Branch in the East African Rift System (EARS) [Wauthier et al., 2015] and magma chamber deflation likely promoting slip on an adjacent border fault >20 km away in the Natron Rift of the

Eastern Branch of the EARS [Jones et al., 2019]. Previous studies have found a link between static stress transfer from earthquakes to magma reservoirs promoting future eruptions in subduction zone settings [Diez et al., 2005, Nostro et al., 1998], but minimal work has focused on the reverse effects. Many questions remain about the details of the interactions between volcanic and tectonic sources, especially in complex youthful rifts, such as the role of local topography-induced gravitational potential energy, fluid interactions [Leseane et al., 2015], and irregular source geometries. These processes have been difficult to address due to limitations in existing methodologies and challenges with collecting high quality geophysical data in youthful continental rifts [Corti, 2012].

One of the current key methods used in investigating volcano-tectonic interactions is computational modeling. Computational modeling methods solve a wide variety of geophysical equations either analytically or numerically. The modeling we employ in this work allow us to calculate stress transfer in active volcanic and tectonic settings using the finite element method. Many computational methods utilize simplified material parameters and geometries due to the methodology (i.e. elastic half-space analytical approaches verses finite element or finite volume numerical methods), potential lack of geophysical, geochemical, and/or geodetic constraints, or because there are no existing models available to benchmark approximate solutions. Simplified model parameters typically are used for analytical solutions and include the following assumptions: all materials have the same properties and deform elastically, also known as homogeneous, elastic half-space models [i.e. Okada, 1985, Toda et al., 2005]; volcanic magma reservoirs are modeled as pressurization from a concentrated point, known as point sources and often implemented as the Mogi model [Kiyoo, 1958]; and the models do not have topography. Using these simplified methods provides only a basic or over generalized view of how volcanic reservoirs behave, which limits our understanding of volcano-tectonic interactions. These simplified models have also been rec-

ognized to either underestimate associated displacements or require unrealistic pressure or volume changes applied to magma reservoir sources to match observed surface displacements [Berrino et al., 1984]. However, applying finite element methods and finite volume methods have allowed researchers to add more complexity to volcano reservoir models and perform volcano-tectonic simulations with increasingly realistic models. The ability to impose complexity allows for more detailed investigations of volcanic regions [i.e. Apuani and Corazzato, 2009]. This investigation offers valuable information about a youthful active rift region where many questions remain about how volcanic and magmatic activity interact with border faults to accommodate extension.

We use the finite element method implemented in PyLith [Aagaard et al., 2008, 2009] to investigate volcano-tectonic stress interactions in a section of a youthful continental rift region in east Africa known as the Natron Rift (Figure 2.1). In this project, we test the influence of three key parameters that are usually missing from simple elastic half-space analytical models: 1) laterally varying material properties derived from a seismic velocity model [Roecker et al., 2017], 2) variations in a spherical reservoir volume size, and 3) topography. We recognize other factors are important for volcano-tectonic interactions, such as fluids, material mixing in reservoir, and irregular magma reservoirs, but we focus specifically on parameters that are simplified in elastic half-space volcano-tectonic models. We hypothesize that, individually, each of these parameters produces a significant change in the stress transferred to an adjacent fault from a magma reservoir deflation event. The model parameters are constrained by geophysical, geochemical, and geodetic observations and are explained in detail in Section 2.4 along with how we quantify significant change. We use PyLith to calculate stress changes that are resolved on two segments of the Natron Fault that are near the active volcano Ol Doinyo Lengai, which is the major western border fault of the Natron Rift (Figure 2.1). Our results suggest that only topography significantly

influences the stress transferred to an adjacent fault in a youthful continental rift. We find that changing material parameters to be heterogeneous and changing reservoir volume sizes have some influence on the stress transferred to the Natron Fault, but the influence of these two parameters do not pass our threshold of 0.1 MPa [Hamling et al., 2010, Jones et al., 2019] for significant stress change.

2.3 Study Area

We select the western portion of the Natron Rift for our study area to test our hypothesis. The Natron Rift is located in northern Tanzania and is currently considered a young rift segment in comparison with other rifts in the Eastern Branch of the EARS. Kinematic models derived from geodetic observations indicate the Natron Rift is currently rifting at 3.8 mm/yr [Stamps et al., 2021]. The western section of the Natron Rift shown in Figure 2.1 is ideal for our study on volcano-tectonic interactions due to the close proximity of the active carbonatite volcano Ol Doinyo Lengai and the adjacent active major western border fault known as the Natron Fault. These two features are ideal for investigating volcano-tectonic interactions during youthful continental rifting since they are part of the active southern Eastern Branch of the EARS. The potential for ongoing activity, along with their close spatial proximity, creates an opportunistic setting for capturing volcanic and tectonic signals, as well as their interactions. Another important reason we select Ol Doinyo Lengai and the Natron Fault is the unique character of the Ol Doinyo Lengai volcano. Ol Doinyo Lengai has a potentially complex reservoir system [Petibon et al., 1998, Reiss et al., 2021] that produces low viscosity carbonatite volcanism. The volcanic plumbing system is hypothesized to be a multi-reservoir system [Baer et al., 2008, Weinstein et al., 2017] with erupted materials originated in a relatively deep 15-20 km magma reservoir [Petibon et al., 1998, Reiss et al.,

2021] that collect in a ∼3 km magma reservoir [Petibon et al., 1998, Reiss et al., 2021]. Our previous work in this area with analytical modeling [Jones et al., 2019] also allows us to validate our finite element solution.

2.4 Methods

2.4.1 PyLith

We use the finite element code PyLith to test our hypothesis and model the magma reservoir of Ol Doinyo Lengai and the adjacent Natron Fault as shown in Figure 2.1. PyLith is an open source, scalable software that can be used to simulate crustal deformation in 2D and 3D through a numerical finite element approach. PyLith allows for modeling both quasi-static and time-dependent problems allowing adaptable approaches to various solving crustal deformation scientific problems. Another aspect that makes PyLith a unique method to solving problems in crustal deformation and tectonics is the modular design that has been incorporated into the code. PyLith consists of distinct modules that each perform a specific action in order to successfully investigate complex problems [Aagaard et al., 2009].

There are four main modules necessary for PyLith to function. The first two modules are responsible for the creation of the model geometry, generation of the model mesh, and establishing model parameters. We use the code Coreform Cubit 2020.2 to build our model geometries and define our mesh size while defining the boundaries and surfaces of our model for PyLith. The second module is a collection of configuration files that initializes the parameters of the numerical method, as well as, defines various parameters of the simulation (i.e. boundary conditions, initial values, and material parameters). This second module also uses a software framework called Pyre that allows cooperation between original standalone

codes to solve various numerical problems through different approaches. The third module is the main package of PyLith used to read in the model geometry and parameters while placing them in a format that can be used to solve the mathematical equations for the simulation. This third module also includes the main component of PyLith used to solve these complex equations called PETSc. PETSc, the Portable, Extensible Toolkit for Scientific computation, is the part of PyLith that creates and solves the matrices set up for the partial differential equations. PETSc allows for various types of numerical linear and non-linear solves (i.e. Jacobian, least squares, Chebyshev iterative). The last module is the visualization and post-processing. This last module has the most flexibility as there are many existing codes that can be used to read the output files of PyLith as long as they are formatted correctly. We use Python and Paraview for this step based on the default output files of PyLith which are .vtk and .h5 files. Figure 2 presents the workflow that we use in this project including codes, solution parameters, and output files. Because PyLith is build in this modular way, our workflow may differ slightly than other researchers who use other geometry and mesh generation tools, solution parameters, and visualization tools.

The governing equations of PyLith are derived from the wave equation and in our problem the equations are simplified by a Lagrangian description of the conservation of momentum. The following equations are the set of relationships that are used for the index notation of the governing equations ending with the elasticity equation that we solve using PyLith.

$$\sigma_{ij} n_j = T_i \text{ on } S_t \tag{2.1}$$

$$u_i = u_i^0 \text{ on } S_u \tag{2.2}$$

$$R_{ki}(u_i^+ - u_i^-) = d_k \text{ on } S_f \tag{2.3}$$

$$\rho \frac{\partial^2 u_i}{\partial t^2} - f_i - \sigma_{ij,j} = 0 \text{ in } V \tag{2.4}$$

In these equations, tractions (T_i) are specified on fault and magma reservoir surfaces (S_f), displacements (u_i^0) on the model surface (S_u), and for tectonic simulations slip (d_k) on the fault surface (S_f). The traction vectors are adjusted for different coordinate systems by using the rotation matrix (R_{ki})m which allows for various fault and surface geometries. The full finite element formulation incorporating Galerkin's method can be found in the PyLith manual [Aagaard et al., 2008].

2.4.2 Model Set-Up

Domain Geometry

To build our model in PyLith we use the computer code Coreform Cubit 2020.2, which builds and meshes our simplified geometry of the Natron Fault, Ol Doinyo Lengai shallow reservoir, and 3D model domain. We use a 3D rectangular cuboid for our model domain. The Ol Doinyo Lengai magma reservoir is positioned in the center of the model domain at 3 km depth to represent the hypothesized shallow magma reservoir of Ol Doinyo Lengai. Two distinct fault segments represent the Natron Fault. This set-up is similar to the analytical models that were created in the previous work of Jones et al. [2019] using the USGS code Coulomb 3.4 [Toda et al., 2011]. We set our domain model size at 100 km x 100 km x 60 km due to results found from boundary condition tests. We tested four different boundaries for the sides of our model specifying the top as a free surface and locking the model bottom boundary with a fixed velocity boundary condition. We calculated residuals between displacement magnitudes for the different boundary conditions at the surface. The boundaries tested included Dirichlet, Neumann, free surface, and rolling boundaries for domain sizes of 25 km

x 25 km x 25 km through 150 km x 150 km x 100 km in increasing increments of 25 km in the X and Y directions and increasing 15 km for each depth tested. The results indicate that the 100 km x 100 km x 50 km domain with different boundaries produces negligible differences in displacement magnitudes (<0.15 mm) in the center of the model within <30 km of the magma reservoir. These results suggest that the boundary conditions will not have a significant effect on the interior of the model domain where our region of interest is located. We also note that there was no significant decrease in the differences when testing the larger 125 km and 150 km models. Through these tests, we recognize that 100 km x 100 km x 50 km is the minimum domain needed to maximize computational efficiency, however in our evaluations we increase the depth to 60 km to include all of the available waveform tomography data used in creating the heterogeneous material model. More details about the boundary condition tests and incorporation of the tomography data can be found in the supplemental information and in the following section on material parameters.

For our modeled fault geometry we use a simplified fault geometry constrained from the geologic map of Sherrod et al. [2013]. We include two distinct fault segments of the Natron Fault totaling ~35 km in length along strike with a dip of 50°. We divide the fault into two segments, the 'volcano adjacent' (351° strike) and the 'basin adjacent' (5° strike) segments following Jones et al. [2019][Figure 2.1]. We explain our geometry for the Ol Doinyo Lengai magma reservoir in Section 2.4.2.

Defining a meshing scheme is an important step in developing the geometry required for PyLith. In this project we use a non-uniform mesh that varies in size based on the model element. Starting with the finest meshing scheme, we define the surface and volume intervals for the magma reservoir at 0.4 km^3 for volume elements and surface elements at 0.4 km^2. We mesh the 'volcano adjacent' segment of the fault surface at an interval of 0.2 km^2 and the 'basin adjacent' section at an interval of 0.5 km^2. The 'volcano adjacent' side is defined as a

finer mesh so we can better resolve potential stress transfer from the magma reservoir. The rest of the model domain is meshed at larger values of 1.1 km^3 for all volumes and 1.1 km^2 for all surfaces. Figure 2.3B shows an example of the non-uniform meshing schemes defined on the fault.

Material Properties

We define our model material parameters for creating the homogeneous and heterogeneous model using two different methods. In the homogeneous models we use a direct input method that uses an average crustal density (ρ) = 2800 kg/m^3, shear wave speed (V_s) = 3.76 km/s, and body wave speed (V_p) = 6.370 km/s as the material properties for the entire domain. Using these values allows us to reproduce the moduli used in the previous analytical models of this region in Biggs et al. [2013], Jones et al. [2019]. To create our model with heterogeneous material properties, PyLith requires the inputs of density, V_s, and V_p to calculate the bulk and shear moduli needed for the problem formulation. Typically in homogeneous models, a direct relationship can be made between the shear moduli and the shear wave speed (V_s), however this relationship cannot be used when it requires the shear moduli to change. Instead, we calculate the density values from updated mathematical relationships used in Brocher [2005] that allow us to approximate density using V_p values availalbe from Roecker et al. [2017]. Equation 2.5 is a polynomial regression that we use to solve for this relationship. We solve this equation using V_p values from the seismic waveform tomography data of Roecker et al. [2017], which includes our region. Equation 2.5 provides the relationship for density and V_s values associated with V_p models and is valid for V_p wave speeds between 1.6 km/s and 8.5 km/s [Brocher, 2005]. In our heterogeneous model, we have a range of density from 2648 kg/m^3 - 3370 kg/m^3, V_s from 3.29 km/s to 4.79 km/s,

and V_p from 5.66 km/s to 8.22 km/s. The Roecker et al. [2017] model spans the entire model domain down to 60 km in 1 km depth slices.

$$\rho(\frac{g}{cm^3}) = 1.6612V_p - 0.4721V^2{}_p + 0.0671V^3{}_p - 0.0043V^4{}_p + 0.000106V^5{}_p \tag{2.5}$$

Reservoir Geometry

For the magma reservoir we use the hypothesized total volume derived from petrological constraints from Kervyn et al. [2010] and calculate the associated radii lengths for a simple spherical geometry. These petrological constraints are consistent with an inversion of InSAR data in Biggs et al. [2013] that suggests a magma reservoir resides at ∼3 km depth and experienced a volume change during the most recent eruption that ranges from 10^6 to 10^8 m^3. We use these volume change values to define the minimum and maximum volume of a spherical reservoir that has radii of 69 m and 290 m respectively. Due to the large size of the domain and the relative small size of the magma reservoir, we are not able to test magma reservoir volumes $<$ 130 m, so we select a range of magma reservoirs with radii between 130 m to 290 m in 10 m increments. The values of the reservoir volume changes that we model Ol Doinyo Lengai are constrained by Biggs et al. [2013], who inverted InSAR data that observed deformation due to the last major eruption at Ol Doinyo Lengai in 2008. Using the approach of Kiyoo [1958] for the inversion, which assumes a point source for the magma reservoir, Biggs et al. [2013] loosely constrained a deflation event that occurred at a 3 km deep magma reservoir with a volume change of -3x$10^7$$m^3$. This point source inversion is considered loosely constrained due to the trade off with depth and magma compressibility. Since stress tractions are used in PyLith as model surface inputs, we are required to convert the volume change into the equivalent pressure change. We use the Equation 2.6 as the relationship used

for this conversion. This relationship was derived using the deformation solution of a simple spherical magma reservoir with uniform internal pressure and in a homogeneous elastic half-space. This relationship is also dependent on the magma reservoir radius size requiring us to use a different pressure change for each different sized magma reservoir. Figure 2.4.

$$\Delta P = \frac{\Delta V \mu}{\pi r^3} \tag{2.6}$$

where ΔP is the pressure change, ΔV is the volume change, and r is the radius of a spherical magma reservoir.

Topography

To incorporate topography in our model we use a downsampled digital elevation map (DEM) from images captured by the Shuttle Radar Topography Mission at 30 m resolution (SRTM30). This process provides a simplified topography to use for our PyLith simulations including Ol Doinyo Lengai's volcano edifice and a generalized fault escarpment of the Natron Fault. Similar to the method for creating the geometry, the topography is read and built in the first module using Coreform Cubit 2020 while the downsampling is performed using Python. In our final topography model we have an additional 2-3 km of material including the volcano edifice and the fault escarpment for the Natron Fault (Figure 2.3).

2.4.3 Modeling Comparisons

In order to compare the influences on stress calculated from the three selected parameters (topography, reservoir size, material properties) there are additional steps that need to occur in the post-processing stage of PyLith using Python 3. The first step is the extraction of

results from PyLith output files. Unlike the displacement results where each location point directly relates to a displacement value, the stress change is stored and read as elements, with each element consisting of three vertices constraining a surface. Examples of these elements are located in Section 2.5

To help with clarity in our results, we define and refer to our simplest PyLith model the 'base model' in all of our comparisons. This base model consists of: a regular 100 km x 100 km x 60 km domain, a reservoir with a radius of 130 m, homogeneous materials, and no topography.

The comparisons between the base model and each varied model requires an interpolation step to rename the vertices of the different models. This step is necessary because, even though each fault mesh is located in the same model space for each model, each element has a different assigned value because of slight changes in the various geometries used to accommodate changes in reservoir size and topography. We project the results for each model onto the original base model fault geometry so that we have a consistent element naming convention. Then we perform calculations from projected, interpolated results in Python. For the projection we use the nearest neighbor interpolation to maintain the values for each element and remap only the element name.

Along with the post-processing to prepare our PyLith models for comparisons with each other, we additionally need to establish the definition of 'significant change' between models. For this definition we use a percent difference calculation presented in Equation 2.7. We establish a difference threshold at a value of 0.1 MPa from evidence in Hamling et al. [2010] where stress changes >0.1 MPa could create a stress field that promotes fault slip (unclampling) in mature rift regions. In Equation 2.7 m_base is the stress change result from our base model and m_var is the stress change result from a model with a single varied parameter that we are comparing. By solving Equation 2.7 using our threshold value of 0.1 MPa

and the maximum of our base model value, m$_b ase$, we calculate a percent difference value of sim20\$. Using this value, we can determined which parameters generate a 'significant change' when averaged over an area of our fault.

$$\frac{|\sigma_{m_b ase} - \sigma_{m_v ar}|}{max|\sigma_{base}|} * 100 \tag{2.7}$$

where σ_{m1} is the maximum stress change for our base model, and σ_{m2} is the maximum stress change for the compared modeled.

2.4.4 Modeling Validation

Because we use a finite element numerical analysis method to model our results we choose to validate our model solutions. Validating our solutions is necessary since the finite element method is not directly solving solutions. Instead, the finite element method combines a series of approximations into one solution. By attempting to reproduce our previous results from these previous solutions, we can increase the confidence in our numerical approximation solution and begin to understand some of the uncertainties. We validate our model by comparing both surface displacements and stress changes on the Natron Fault with Line-of-Sight displacements from InSAR published in Biggs et al. [2013] and stress change results on the Natron Fault from Jones et al. [2019], respectively. The Line-of-Sight displacements indicate ∼7 cm of subsidence located above Ol Doinyo Lengai's magma reservoir. Our base model has vertical surface displacements with similar magnitudes.

Along with confirming that our finite element approximated solution is reasonable, we also have to confirm that the multiple PyLith models created are also consistent with each other when discussing the measured displacements. Even if we hypothesize that our

different parameters will give us different results in the stress transferred, we expect that all our models will provide similar surface displacements as our analytical models and to each other. In Figure 3 we show that we produce similar displacement results with a deflation event with our models of no-topography calculating a maximum displacement magnitude value of ∼20 cm, a ∼5 cm difference from the results in Biggs et al. [2013], and for our topography models calculating a maximum displacement magnitude value of ∼12 cm. We hypothesize that the small mismatches are due to the model design (volumetric verses Mogi point source) and the use of pure vertical displacements versus Line-of-Sight deformation, consisting of all three directions of motion, from the interferogram resulting in displacements sim15 cm over the summit of Ol Doinyo Lengai. The difference in calculated displacements between the flat surface and topography model are supported in literature that provides evidence that changing topography when calculating displacements has a significant effect on the result [Cayol and Cornet, 1998].

To validate the stress change results, the PyLith stress change results are qualitatively compared with results from the analytical code Coulomb 3.4 used in Jones et al. [2019] and similar projects in the Natron Rift. Figure 2.5 shows the validation comparison for the stress results compared to results used in Jones et al. [2019]. These figures presented are comparable with a few key exceptions. In the dip-slip shear component (B.), there is a large variation at ∼12 km depth in the PyLith output on the volcano adjacent side. We hypothesize that this difference is caused by the volumetric verses point source model design. With this difference we also are aware of how the mesh discretization scheme can also affect the result. Compared to the Coulomb 3.4 models in our previous work which use a meshing size of ∼1 km^2, we use a finer resolution for the mesh element size on the volcano adjacent side mentioned in Section 2.4.2. Overall, with the model differences mentioned, these results

are comparable to previous results and that the model solutions can be used for further investigations.

2.5 Results

In Table 2.1 we present select key models that we chose to run and the parameters associated with it. From this table Model A represents the base model that is used in the first set of comparisons. We created, in total, 64 different models each to cover all cases of material properties (homogeneous and heterogeneous), reservoir size (130 m to 290 m), and topography (removed and included). Table 2.1 also presents the maximum stress magnitude that is calculated on the Natron Fault for each associated model. For each of the models this maximum value was calculated on the volcano adjacent side in the center of the bulls-eye pattern shown in the example output for the base model in Figure 2.6. We only show the magnitude vector value for our base model because each of the models generate similar patterns. As mentioned in Section 2.4.2, the mesh element size on the volcano adjacent side is $\sim$0.4 km^2 which is finer than the basin adjacent side $\sim$0.5 km^2. For the models that we ran, the maximum values represented in the center of the bulls-eye pattern ranged from $\sim$0.50 MPa - $\sim$0.62 MPa (Table 2.1).

Our results for the first potential influence on stress transfer that we test, material properties, are presented in Figure 2.7. The percent difference calculation that we use to evaluate model differences is presented in Figure 2.7D. When we average the percent difference over the entire Natron Fault, we find an average percent difference of $<$0.5%. We also see from Figure 2.7D that the majority of the differences between these models occur on the 'volcano adjacent' portion of the Natron Fault. Our percent difference results for the second potential influence, reservoir size, are presented in Figure 2.8. When we average

the percent difference over the entire Natron Fault, we find an average percent difference of ∼2%. Once again, we see the majority of the larger differences between models to be isolated on the 'volcano adjacent' portion of the Natron Fault, similar to our results for the models that compared material properties.

Our results for the third potential influence, topography, are presented in Figure 2.9 and, from first order comparisons, are considerably different both in pattern and value. For this results, when we average out the percent difference over the entire Natron Fault, we calculate an average percent difference of ∼4%. All results are presented in the same MPa scale or same percent different scale. Even though topography gives us the largest percent difference change averaged over the Natron Fault, it still does not cross the threshold we set necessary for 'significant change'. Unlike the other model comparisons however, results from the topography comparison does show a small section on the shallow potion of the 'volcano adjacent' segment that exceeds the threshold. This is directly visible looking at the percent difference result from Figure 2.9D. When plotted using the threshold as the maximum value, any portion of the fault in the black does surpass the threshold. Table 2.2 summarizes the overall results of the model comparisons detailed in the following sections using the end member reservoir size models of radii 130 m and 290 m. We also include in Table 2.2 extra examples of model comparisons that are used for calculating uncertainties from the model comparisons.

2.6 Discussion

Our results show that out of the three parameters we chose to vary, each produced a different effect on the amount of stress resolved on the modeled Natron Fault. We also see that by using the our defined threshold for 'significant difference' on the Natron Fault none of the

models exceed that threshold of averaging > 20%. However, we see in the figures presented that for some of the model comparisons, especially for topography, certain sections of the fault does surpass the threshold set. Recognizing that the method of averaging out percent difference method over the entire modeled Natron Fault is heavily affected by the 0% values on the basin adjacent section we update our percent difference calculation to try and better capture the differences that are visible between the 'volcano adjacent' and 'basin adjacent' sections. To do this, we further divide the fault to add 'shallow' and 'deep' sections of the modeled fault. Next we average the percent difference over 4 individual sections of the fault instead of the fault as a whole. These sections now include 'shallow volcano adjacent', 'deep volcano adjacent', 'shallow basin adjacent', and 'deep basin adjacent'. We define shallow as < 7.5 km depth and deep and >= 7.5 km.

Figure 2.10 focuses on the 'shallow volcano adjacent' section that had the most visible difference, we run the same post processing steps, but this time removing all points outside of the 'shallow volcano adjacent' section as well as the fault edges where PyLith calculates zero stress change by design. Performing this step, we calculate a large increase in our percent difference values for each parameter compared. Differences between material comparisons increase from <1% to ∼4%, between reservoir comparisons from ∼.5% to ∼2%, and between topography ∼4% to ∼7%. This increase is expected as we are removing thousands of zero values from the 'basin adjacent' section and the 'deep volcano adjacent', but still does not satisfy the threshold we set defining 'significant change'. However even though our threshold was not met when averaging sections, Figure 2.10 clearly shows that the shallowest section of the fault <2 km does exceed the threshold for the length of the volcano adjacent section. This result suggests that topography is the only parameter that does significantly influence the stress change resolved on an adjacent fault, but in a limited capacity limited to the shallowest portions of the fault <2 km.

While only varying 3 parameters we also recognize that this is a limited study, however there are other benefits to these created models. One benefit is that our model setup can also act as a benchmark for future volcanic studies that want to utilize PyLith as the methodology. Using PyLith will allow other researchers to further investigate volcano-tectonic interactions in the Natron Rift. We can also benefit from building off of these created models and try to address questions that require more model complexity. This includes understanding more about the plumbing system of Ol Doinyo Lengai and incorporating data from the newly installed GNSS network on Ol Doinyo Lengai, TZVOLCANO. In addition to these benefits, our work is one of the first that presents Pylith's capability to accurately model volcano interaction in addition to the tectonic simulations. This is crucial for future tests that include investigating displacements as well as stress transfer from a magmatic source.

2.7 Conclusions

In conclusion, through our modeling results and evaluations, we show that topography has the most influence out of the three potential influences to the stress transferred in a youthful continental rift that we test. Even though no single changed parameter produced an average change of >0.1 MPa over the entire fault, each parameter varied did have some changes primarily occurring on the volcano adjacent side of the Natron Fault. We also show that topography can produce significant enough change in results and affect the stress calculated on a shallow segment of the volcano adjacent side <2km depths.

We also show in this work that changing both reservoir radius and material properties do not pass the threshold marked for 'significant difference' they can cause small stress perturbations in the stress transferred from magma reservoirs and are important to consider

for small (∼0.1 MPa) stress changes variations. If we chose a smaller threshold <0.1MPa, our results would be different especially when discussing the stress transferred to the volcano adjacent side of the modeled Natron Fault. We also recognize the strong spatial correlations from the difference of results from the various sections of the Natron Fault, with changes and stress increasing closer to the magma reservoir. This result supports research that extreme topography in rift regions may help influence the local stress field and help trigger fault slip, a process critical to the evolution of a rift.

2.8 Acknowledgments

This work was partially funded through the NSF CAREER grant EAR-1943681. We thank the Computational Infrastructure for Geodynamics (geodynamics.org), which is funded by the National Science Foundation under award EAR-0949446 and EAR-1550901, for providing expertise and help with PyLith modeling methods. We also thank the PyLith short-term deformation working group for providing feedback on earlier versions on this project. We also utilized volcanic modeling expertise provided by members of the USGS (United States Geological Survey).

2.9 Tables and Figures

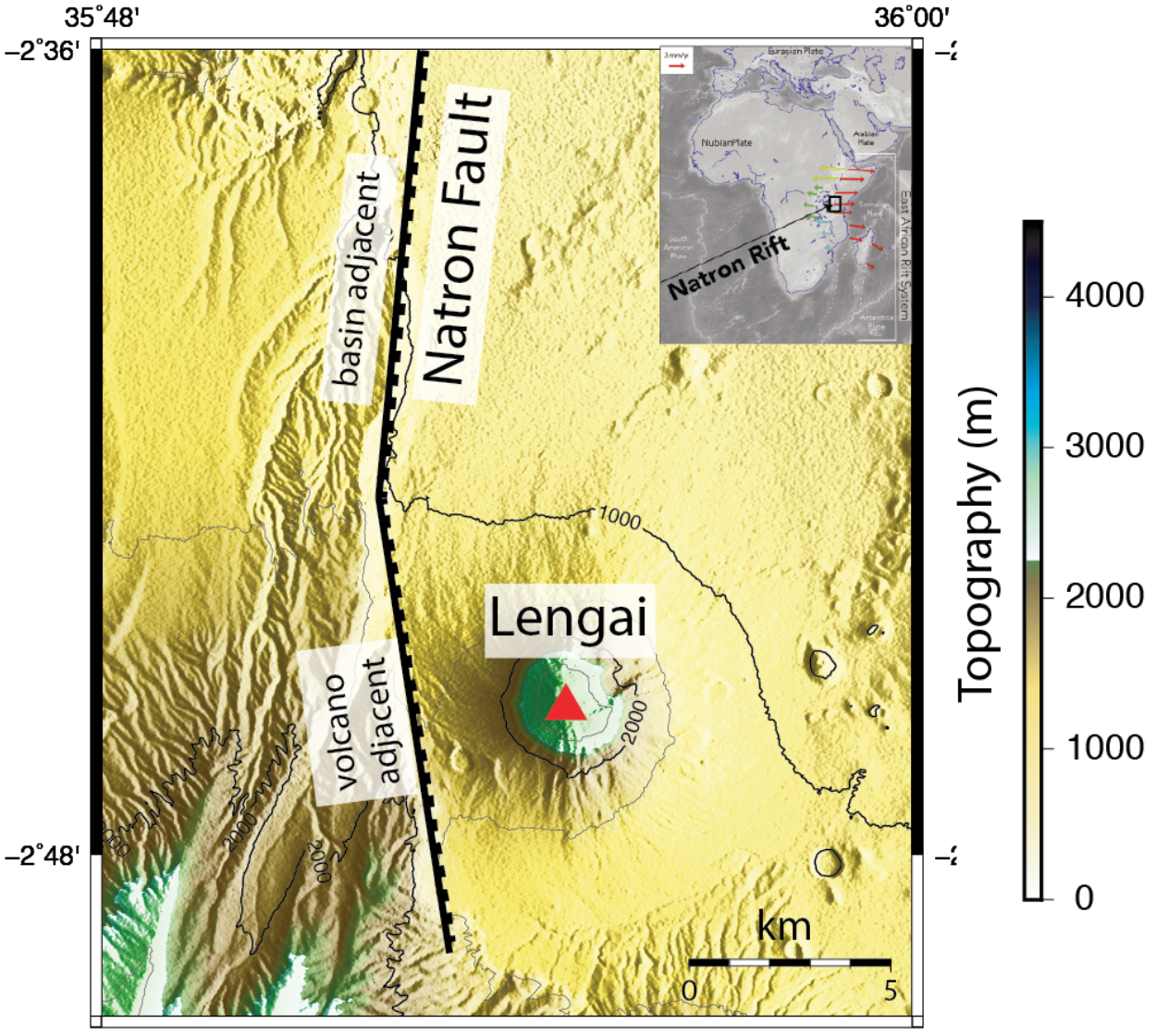

Figure 2.1: The western section of the Natron Rift that we chose to model in PyLith. The active carbonite volcano Ol Doinyo Lengai is labeled and the white dotted line is the fault layout for the Natron Fault. This figure also includes the newly installed GNSS network, TZVOLCANO, with instruments marked by blue triangles and radio repeaters marked with green circles.

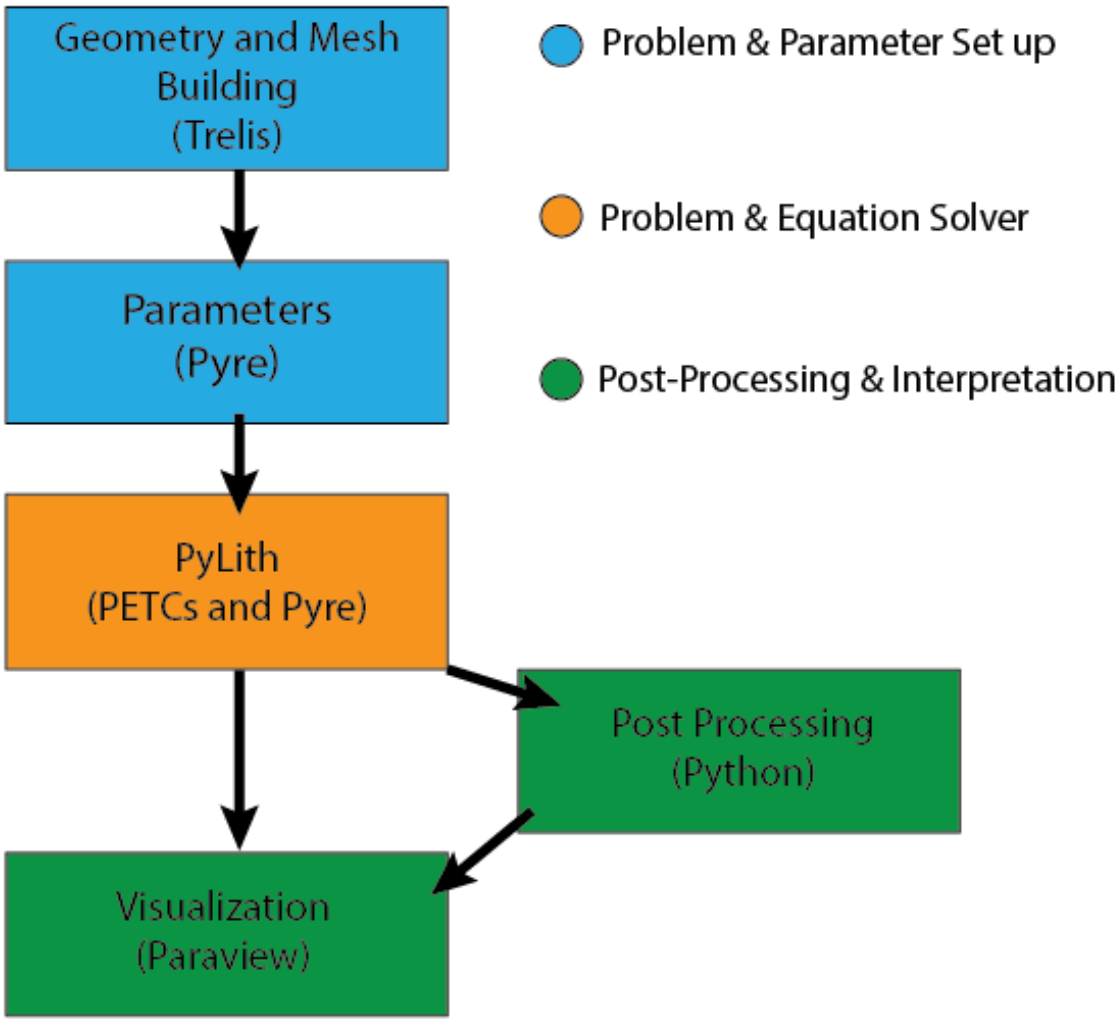

Figure 2.2: The PyLith workflow utilized for this project separated into the individual main modules. Each module is annotated with the specific code used for the associated step. Modules in blue are associated with model set up, module in orange are associated with the model evaluation, and modules in green are associated with model post-processing and interpretation.

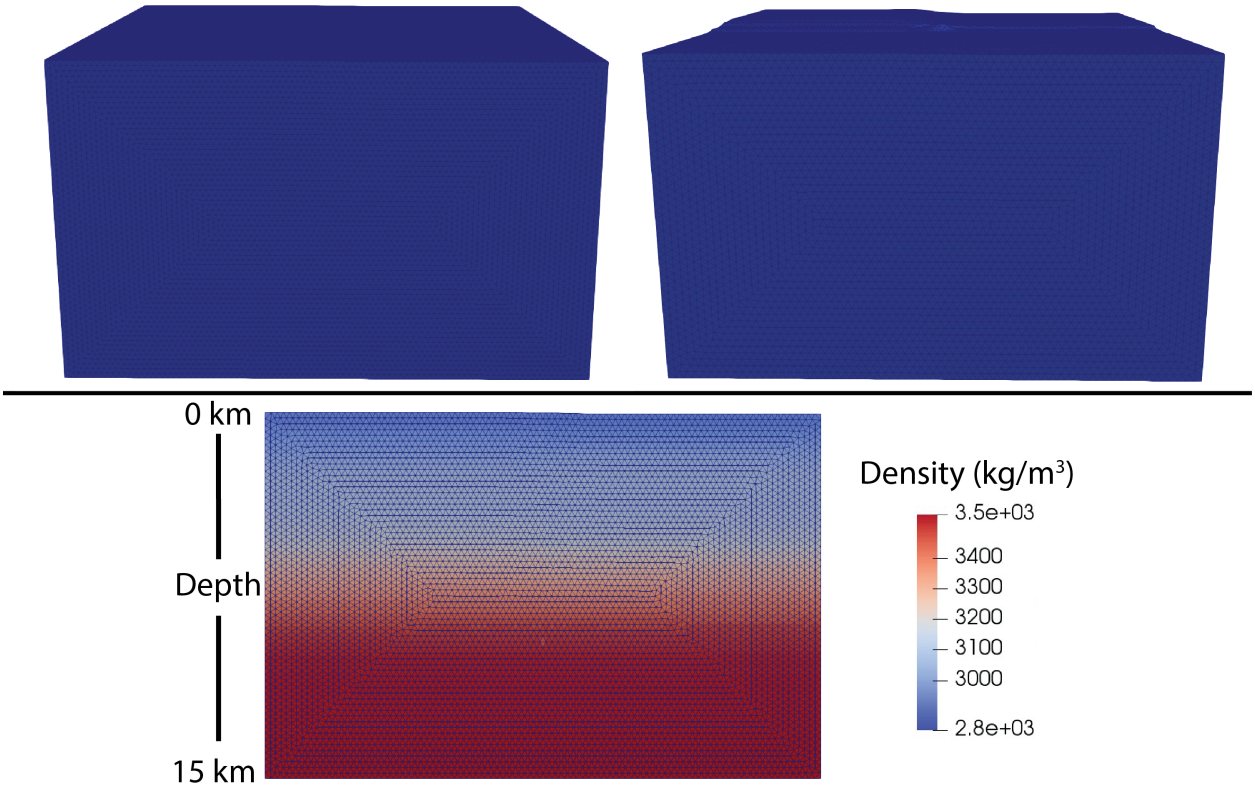

Figure 2.3: Examples of the modeled domains in the geometry and mesh building software Coreform Cubit 2020. Top figures show the incorporation of heterogeneous materials in both the no topography (flat model) and topography model (includes Ol Doinyo Lengai and the Natron Fault escarpment). The bottom figure presents the example of the heterogeneous materials domain with density increasing with depth.

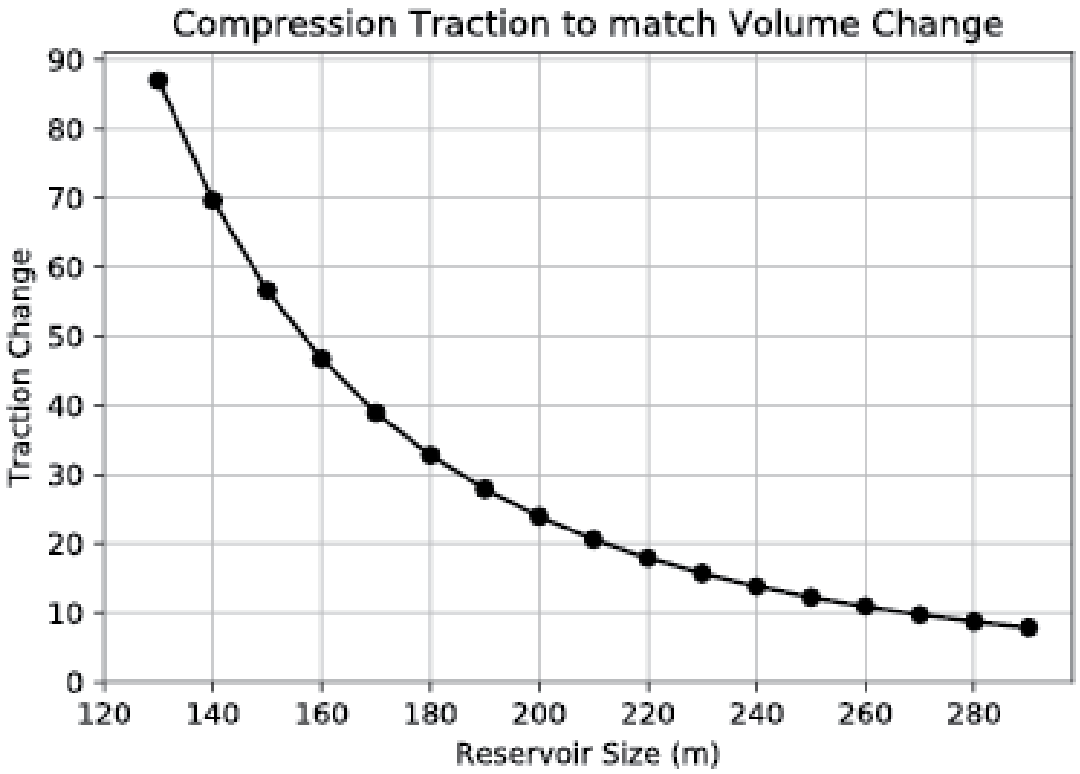

Figure 2.4: The traction required to match the range of volume changes for Ol Doinyo Lengai constrained by Biggs et al. [2013] and the associated reservoir radius used in the model. The graphical representation of Equation 2.6.

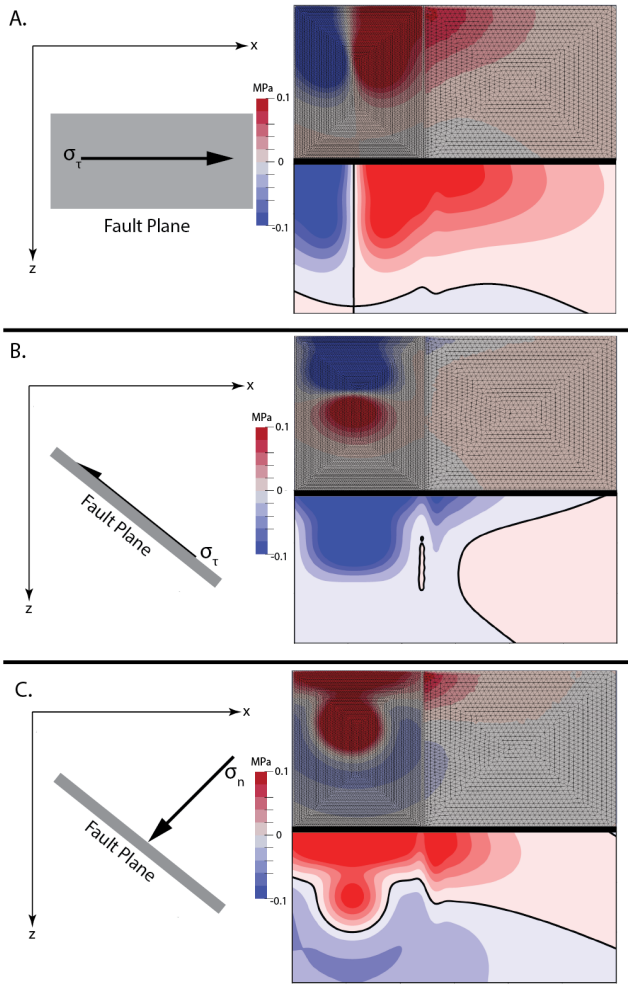

Figure 2.5: Comparisons of PyLith stress components outputs with the previous Coulomb 3.4 stress component results from Jones et al. [2019]. We compare the three main components that are used to calculated the total stress magnitude. These components are the shear component in the strike-slip direction (A), the shear component in the dip-slip component (B), and the normal component (C). For each figure shown the top meshed fault layout is the PyLith output and the bottom fault layout is the Coulomb 3.4 output. Red areas are positive stress change values in each component (in the direction of the arrowhead), and blue areas are negative stress change values (in the direction of the notation).

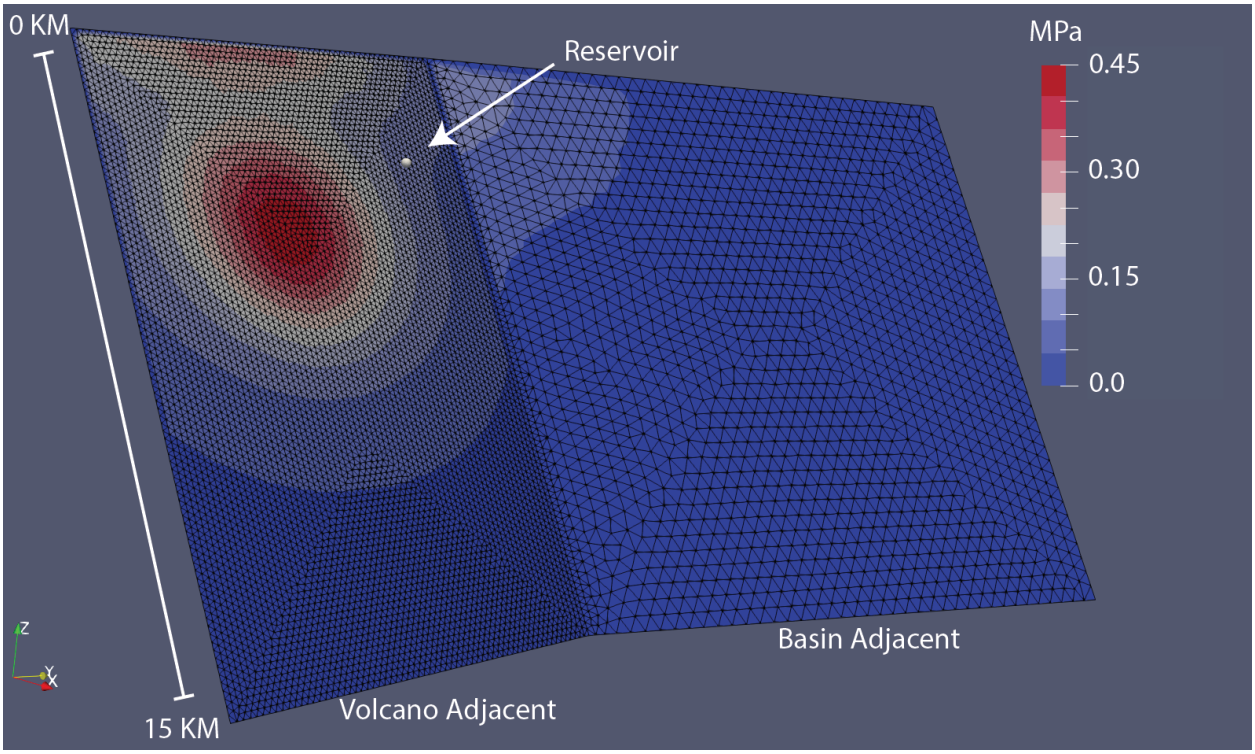

Figure 2.6: Example PyLith output of calculated stress magnitude on the Natron Fault looking west (-y direction). This result is from Model A consisting of a 130 m magma reservoir, no topography, and homogeneous materials. The two different size meshes for the volcano adjacent segment and the basin adjacent segment are visualized clearly, showing the denser mesh for the area of maximum stress change. The scale shown is in Megapascals. Each model output has a similar bulls-eye pattern on the volcano adjacent segment of the Natron Fault.

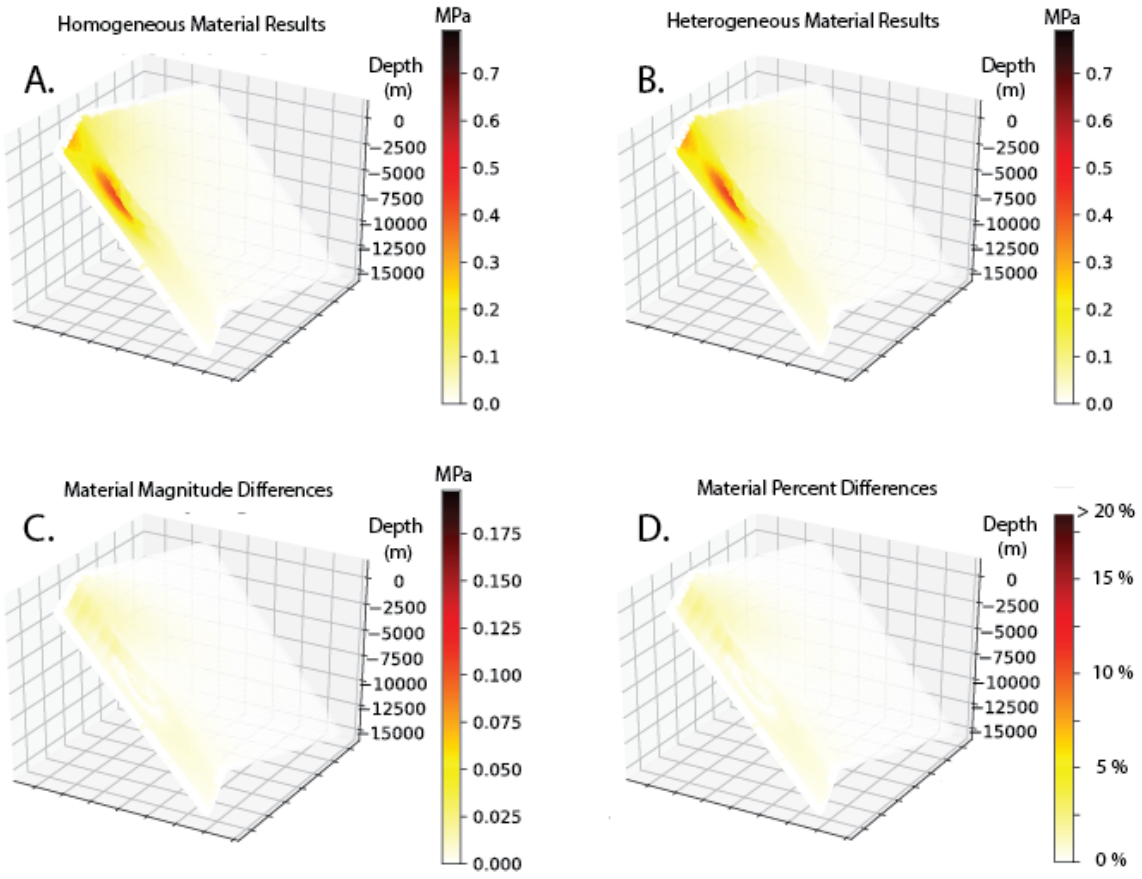

Figure 2.7: Figure presents the comparisons our base model results (A.) with the varied density model (B.) results. Figure C. presents the difference in magnitude between the results shown in A. and B. in MPa. Figure D. presents the percent difference calculation that we average to quantify the change over the fault using the threshold of 'significant change' as the maximum plotted value. All results figure follow this convention. The results in B. have undergone the post-processing interpolation process that is mentioned in Section 2.4.

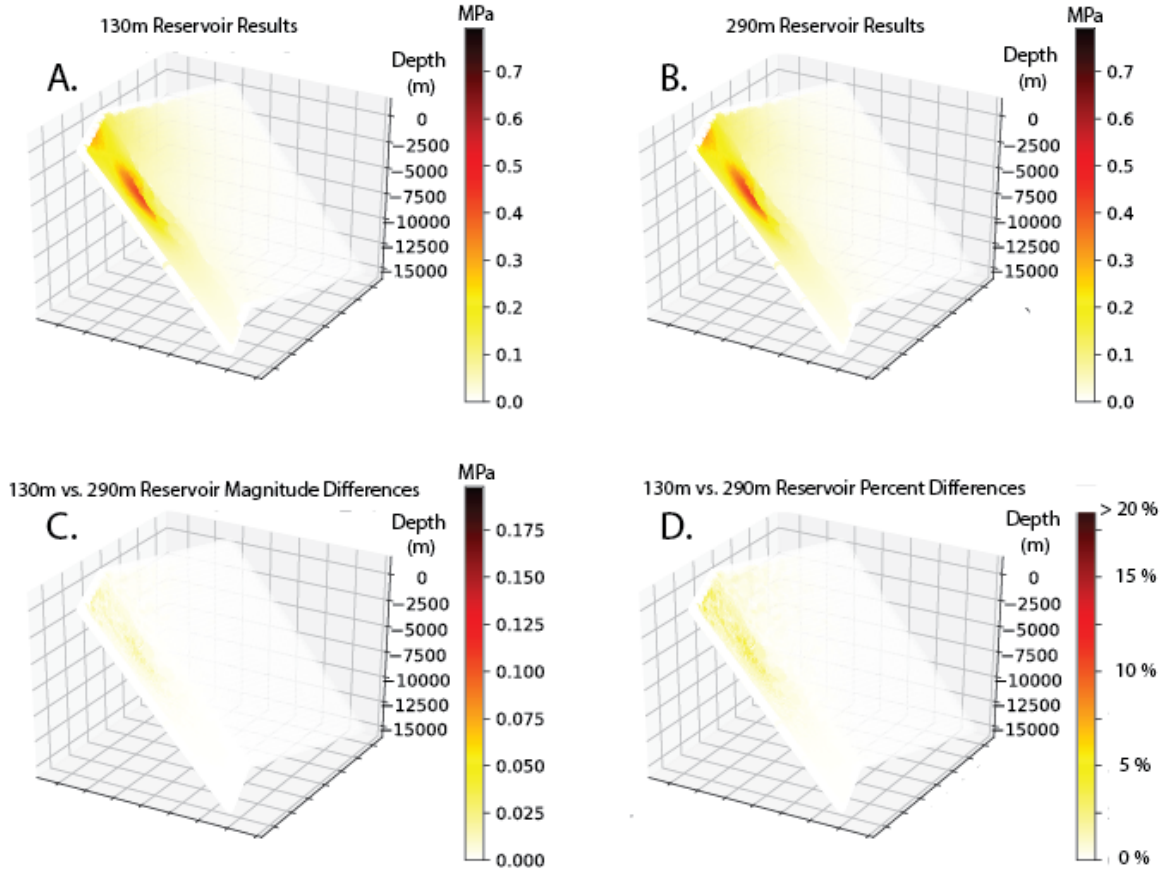

Figure 2.8: The results comparing our base model (A.) with the varied reservoir model of 290 m radius (B.). Following the convention set in Figure 2.7 Figure C. is the difference in magnitude between the results shown in A. and B. . Figure D is the percent difference calculation using the threshold as the maximum value in the scale.

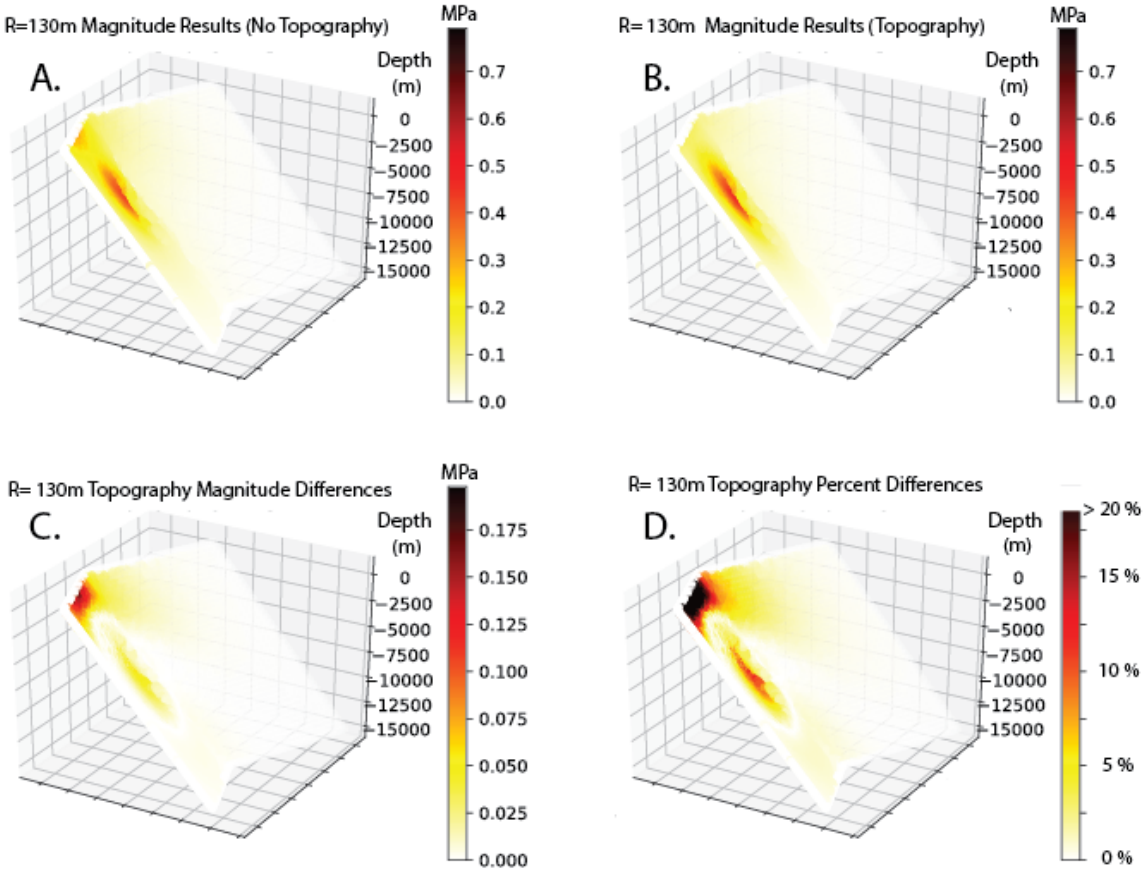

Figure 2.9: The results comparing our base model (A.) with the topography model (B.). Follows the convention of Figure 2.8. Figure C. is the difference in magnitude between the results shown in A. and B. . Figure D is the percent difference calculation using the threshold as the maximum value in the scale.

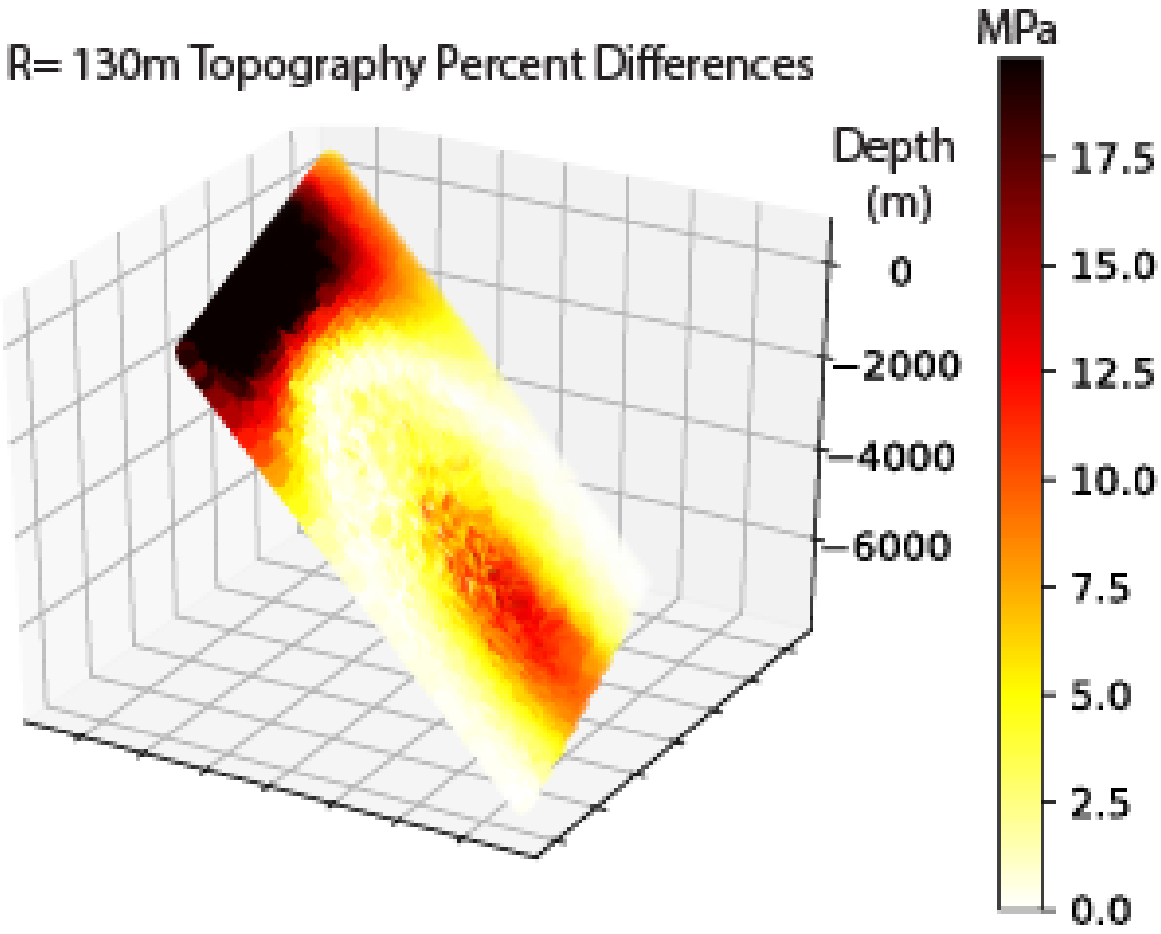

Figure 2.10: The percent difference results of our topography comparison focused on the shallow volcano adjacent section of the fault. Following the convention set in the full fault figures, the threshold of 'significant change' is the maximum plotted value at 20% and that value is exceeded in the black areas of the fault.

Table 2.1: The eight separate models that we created and ran in PyLith. We include the maximum magnitude calculated for each model in the last column.

Model	Reservoir Size (radius)	Topography	Domain Material	Maximum Stress Magnitude (MPa)
A	130 m	no	homogeneous	0.54
B	290 m	no	homogeneous	0.56
C	130 m	no	heterogeneous	0.56
D	290 m	no	heterogeneous	0.58
E	130 m	yes	homogeneous	0.50
F	290 m	yes	homogeneous	0.60
G	130 m	yes	heterogeneous	0.52
H	290 m	yes	heterogeneous	0.62

Table 2.2: Table 2. The results from the comparison of maximum stress magnitude resolved on the Natron Fault from the model simulations. Precent differences presented have been averaged over the entirety of the modeled Natron Fault.

Models	Similar Properties	Comparison	Percent Difference
A vs E	130 m reservoir homogeneous material	topography	7.12%
A vs B	no topography homogeneous material	130 m vs 290 m reservoir	1.13%
A vs C	130 m reservoir no topography	domain material	4.13%
C vs G	130 m reservoir heterogeneous material	topography	7.19%
B vs F	290 m reservoir homogeneous material	topography	7.73%
D vs H	290 m reservoir heterogeneous material	topography	7.33%
C vs D	no topography heterogeneous material	133 m vs 290 m reservoir	1.04%
E vs F	topography homogeneous material	133 m vs 290 m reservoir	1.17%
G vs H	topography heterogeneous material	133 m vs 290 m reservoir	1.13%
E vs G	130 m reservoir topography	domain material	4.12%
B vs D	290 m reservoir no topography	domain material	4.86%
F vs H	290 m reservoir topography	domain material	5.02%

Chapter 3

GNSS2CHORDS: A new tool for connecting UNAVCO Real-Time GPS Data Services to CHORDS

3.1 Abstract

Modern instruments used in the geosciences often include the capabilities to record and stream data in real or near-real-time. Real-time data collection can be valuable in addressing scientific questions, as well as for developing hazard assessment approaches. In this work, we present a real-time data broker application called GNSS2CHORDS, which provides the ability to broker streaming positioning data from UNAVCO Real-Time GNSS Data Services into a CHORDS portal. The EarthCube project CHORDS, Cloud Hosted Real-Time Data for the Geosciences, is an open-source cyberinfrastructure designed so that users can easily manage streaming real-time data. We created the data broker application GNSS2CHORDS to access Global Navigation Satellite System (GNSS) sites streaming real-time data through UNAVCO Real-Time Data Services and then relaying that data into a user's CHORDS portal. GNSS2CHORDS helps to remove technical barriers for scientists that want to utilize UNAVCO Real-Time GNSS Data Services. Linking real-time GNSS data with CHORDS opens up data access through simple web services (URLs) and data services, such as visual-

ization and analysis. GNSS2CHORDS also enables the application of FAIR Data Principles to real-time GNSS data.

3.2 Introduction

Tectonic processes in numerous active settings have been observed to occur over a wide range of time-scales. Examples include fault rupture occurring over time periods of less than a day, postseismic slow-slip events that continue for several days, and volcanic reservoir inflation and deflation lasting weeks or months. Seismometers have been used for several decades to capture seismic events across the globe allowing for the development of near-real-time hazard alerts. More recently, Global Navigation Satellite System (GNSS) instruments have become capable of recording 1 Hz positioning data (hereafter referred to as "real-time" data). Accessibility to real-time GNSS data allows for the development of hazard assessments using information about surface displacements, rather than seismic wave velocities, which is beneficial when seismic stations and associated seismology-based hazard assessment tools are not readily available, are saturated in large events, or are subject to long latencies.

Researchers have recognized various technical obstacles associated with the use of real-time data. As a result, scientific communities (i.e. Open Geoscience Consortium (OGC), Open Sensor Hub, Unidata) and standards (i.e. OGC Sensor Web Enablement, National Marine Electronics Association (NMEA) strings) have formed to streamline the construction of real-time data interfaces for a broad set of disciplines. Although numerous tools have been developed using the existing standards to stream and evaluate real-time data, many research groups face barriers implementing real-time data visualization, analysis, and/or hazard assessments with these tools due to the lack of resources or technical limitations [Kerkez et al., 2016].

In this work, we present an open-source cybertool called GNSS2CHORDS that provides streamlined access to 5 cm precision longitude, latitude, and height data [Leandro et al., 2011] from real-time GNSS data streamed through the Real-Time GNSS Data Services at UNAVCO (www.unavco.org), the US National Science Foundation (NSF) geodesy facility. Our cybertool, based in Python, brokers GNSS positioning data from UNAVCO to an instance of the open-source online platform CHORDS [Cloud-Hosted Real-time Data Services; http://chord-srt.com Daniels et al., 2014, Kerkez et al., 2016]. CHORDS is an NSF EarthCube-funded cyberinfrastructure designed to facilitate easy access to real-time data for geoscience disciplines and employ standards and best practices for real-time streaming data among the geoscience community. The CHORDS platform provides user-configured online portals with simple URL data upload and download methods (Web Services). Several geoscience disciplines already integrate CHORDS into their workflows. For example, Gooch and Chandrasekar [2017] describe how atmospheric radar data can be streamed through CHORDS. In this work, we utilized the TZVOLCANO GNSS Network CHORDS portal to test and validate our broker [http://tzvolcano.chordsrt.com; Figure 3.1 Stamps et al., 2016].

Our new open-source code GNSS2CHORDS allows users to broker positioning data from any GNSS station streaming the RTX NMEA format, through UNAVCO's Real-Time GNSS Data Services, into an instance of a CHORDS portal. The code parses NMEA strings for 3-5 cm precision latitude, longitude, and height information and ports the data into CHORDS with a URL. Once data are made available in CHORDS, the user has a set of data services available for visualizing and analyzing real-time data streams with Grafana (http://grafana.com) and can access the data in different formats.

3.3 Results

We designed the GNSS2CHORDS data broker application with Python to access UNAVCO's real-time GNSS data stream, find and select one or more user-requested real-time data streams from a GNSS site, and build the CHORDS portal URL for upload. We chose Python due to its adaptability, open source distribution, and familiarity in the geoscience disciplines. GNSS2CHORDS consists of three executable parts with an associated parameter file and is executed through a Python package executable from the user's terminal.

Our data broker application utilizes the existing BKG Ntrip Client program [Stürze et al., 2016], which is designed to apply the Ntrip standard (Networked Transport of RTCM via Internet Protocol) to real-time GNSS data streams. The BKG Ntrip Client provides us with streaming GNSS data in a standardized format utilized by the National Marine Electronics Association, known as a NMEA string, from stations that are connected to UNAVCO's data caster [Hodgkinson et al., 2020]. The NMEA string format includes information useful for navigation primarily focused on marine instruments (i.e. Bearing Origin to Destination - BOD, and Overall Satellite data - GSA). For GNSS information, we access the NMEA "Global Positioning System Fix Data" string, also known as the GGA string. Relevant for this work, the GGA string standard contains UTC time, geodetic latitude, geodetic longitude, height above the ellipsoid WGS84.

Two workflows for utilizing UNAVCO Real-Time Data Services are shown in Figure 3.2. Without the use of GNSS2CHORDS and an associated CHORDS portal, institutions interested in using the real-time GNSS data streams must develop their own data analysis, visualization, and hazards assessment tools. However, implementing GNSS2CHORDS and a CHORDS portal opens up access to a suite of data services, such as visualization and statistical analysis, and the use of community standards and best practices. GNSS2CHORDS was

validated by streaming real-time GNSS data available through UNAVCO into the TZVOLCANO GNSS Network CHORDS portal, which provides a use-case for demonstrating the value of incorporating GNSS2CHORDS into a workflow.

3.4 Discussion

The application of GNSS2CHORDS for real-time GNSS data streams opens up two key functionalities: data access and data services. Regarding data access, ∼3-5 cm precision positions [Leandro et al., 2011] for specified time frames provided as longitude, latitude, and height become easily downloadable through URLs or through the GUI (Figure 3.1B) in formats commonly used by geoscientists (i.e. GeoCSV, http://geows.ds.iris.edu/documents/GeoCSV.pdf and GeoJSON, geojson.org). For data services, CHORDS connects with the open-source platform Grafana via InFluxDB. Grafana provides tools for automated data analysis and functions such as issuing user-defined alerts when data meet a certain criteria and visualization of the data streams at 5-second intervals.

Data access capabilities made possible by using GNSS2CHORDS and leveraging the short-term storage functionality of CHORDS provide a framework for developing download programs using URLs. We created download scripts that can be used in both Python and Jupyter Notebooks that allow users to request specific daily data files in either GeoJSON or GeoCSV format. The daily files comprise the 1 second coordinates as longitude (degree), latitude (degree), and height (m). These scripts provide a template for users to build download URLs, create daily files, and create weekly files for real-time GNSS data streamed into their CHORDS portal. These download scripts are shared via the same GitHub repository as our data broker application GNSS2CHORDS (See Code Availability below).

Data visualization is accomplished through Grafana. The Grafana interface is employed via CHORDS as an open-source visualization and analysis platform that allows users to query, visualize, and explore various metrics from data streamed through CHORDS. Grafana users can configure data visualization panels as part of their online interface dashboard. With over 350 customizable, pre-configured downloadable dashboards, Grafana provides users numerous options for customization. For our use-case, we use Grafana for time-series visualization and a simple statistical analysis to assess if height data averaged over a specified time frame (i.e. 5 minutes) exceeds a certain threshold (i.e. +-5 cm). Email alerts can then be triggered when the threshold is exceeded. This particular data service is a benefit to geohazards applications because shifts in latitude, longitude, and/or height at GNSS stations associated with a natural hazard can occur in periods less than a day [Hoechner et al., 2013, i.e.]. More complex, user-defined algorithms can also be applied to real-time data streaming via GNSS2CHORDS using the Grafana add-on Kapacitor.

In addition to the benefits of the data access and data services described above, implementing GNSS2CHORDS in a real-time GNSS workflow helps users align their data streams with FAIR Data Principles [Wilkinson et al., 2016]. FAIR data is findable, accessible, interoperable, and reusable. GNSS2CHORDS provides a mechanism to make positioning data publicly accessible. Anyone with internet access has the ability to view and download positioning data provided by GNSS2CHORDS. Given the simplicity of the positioning data (latitude, longitude, and height), the data can be compared with other streaming datasets, such as gas measurements, which would increase interoperability and reusability. The successful deployment and integration of a CHORDS portal with UNAVCO's real-time data services can offer significant utility to the GNSS workflow, offering simple adjustments, standards-based outputs and iterative analysis. Adapting current methods will continue to spur innovation in the geosciences pushing developments of more capabilities and uses of

real-time data and ultimately will allow our scientists to better advise policy makers about possible community risk.

3.5 Methods

Figure 3.3 details the operation of GNSS2CHORDS. The first step of GNSS2CHORDS involves initializing the BKG Ntrip Client program to access UNAVCO Ntrip's connection. In this first stage, the real-time data streams are accessed and the requested GNSS site data stream is discovered. The site ID, caster information, caster connection port, and other network requirements (i.e username and passwords) are read from the parameter file. Once a connection has been made to the data stream, the next step of the code pushes the stream to continue operating in the background.

The second process of the data broker application is executed once the stream is in the background and is able to be read; all while the BKG Ntrip Client continues to stream future data entries. It is important to mention that the stream cannot be parsed until it is running in the background state. At this second stage, the data broker application reads the GGA-NMEA formatted GNSS data strings and parses the fields for latitude, longitude, height, and time, while simultaneously converting values to fields recognized by CHORDS. These conversions include changing the latitude and longitude values from separate fields of degree, minutes, seconds to one field of decimal degree. The application also changes the directions attached to latitude and longitude (i.e. N/S and E/W) to +/- respectively, which is a format that can be read by the CHORDS portal. The date and time are also formatted to be read in the CHORDS portal but no conversions are made due to the utilization of UTC time standard. These fields are taken from the GGA-NMEA string, and are then stored in a

temporary queue. The temporary queue provides an additional buffer to mitigate connection errors caused by the differential speeds of UNAVCO's BKG caster and CHORDS data portal.

The final process of GNSS2CHORDS runs when a new data entry is detected in the program queue. When the data entry detection occurs, the program accesses the new data in the queue and builds the URL necessary for data ingestion into the CHORDS portal. An example of the built URL is below:

http://tzvolcano.chordsrt.com/measurements/URL_create?instrument_id=SITE_ID
&lat=LATITUDE &lon=LONGITUDE&height=HEIGHTat=DATETTIME

Values taken from the GGA-NMEA data stream and passed through the program are in red. Once this URL is requested through the program, the data are input into the CHORDS portal. This process continues as GNSS positioning data are streamed and will automatically be counted and visualized in the CHORDS portal until the program is terminated. If the connection to the caster stream is broken, and GNSS2CHORDS will automatically restart to minimize data loss. We note that GNSS2CHORDS allows users to choose any GNSS data stream from UNAVCO Real-Time GNSS Data Services by changing only the site ID and portal location.

3.6 Data Availability

The data from TZVOLCANO discussed in this article that are parsed by GNSS2CHORDS for longitude, latitude, and height can be downloaded from the TZVOLCANO CHORDS portal at http://tzvolcano.chordsrt.com/data for the most recent 5 months. The data can be downloaded in both JSON (GeoJSON) and CSV (GeoCSV) file formats. Data for prior

months can be accessed through VTechData (https://data.lib.vt.edu/), the data repository for Virginia Tech. The TZVOLCANO real-time GNSS data can also be accessed through the UNAVCO Real-Time GNSS Data Services (https://www.unavco.org/data/gps-gnss/real-time/real-time.html) in the NMEA string format.

3.7 Code Availability

GNSS2CHORDS is available through the CHORDS GitHub repository (https://github.com/earthcubeprojects-chords/chords/tree/master/bin/gnss2chords).

3.8 Figures

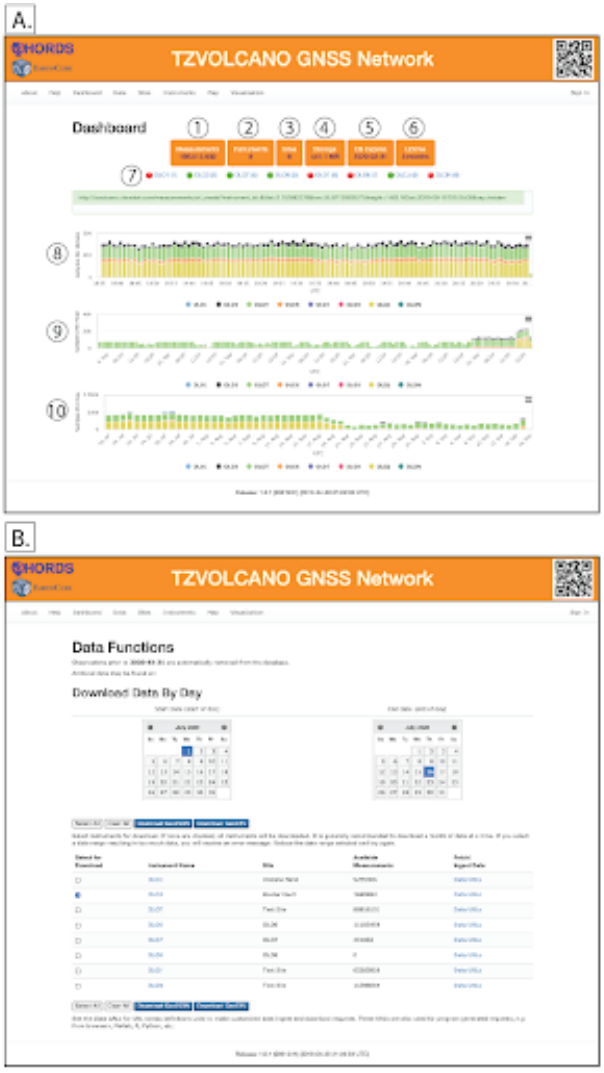

Figure 3.1: The TZVOLCANO GNSS Network CHORDS portal Dashboard (A) and Data Functions interface (B). A: (1) Number of measurements or data points temporarily stored in the CHORDS Portal. (2) Number of instruments currently set up to stream data. (3) Number of sites (important when multiple instruments are set up in one location). (4) Amount of storage space used in the online Portal instance. (5) Date when data will be deleted. (6) Time since the last software update. (7) Red dots represent sites currently not streaming and green dots represent sites that are actively streaming data. (8) Number of samples per minute in bar graph format. (9) Number of samples per hour in bar graph format. (10) Samples per day in bar graph format. Each color in 8-10 corresponds with a distinct instrument. B: Data Functions interface that allows for direct file download. Data URL format structures are also found through this interface.

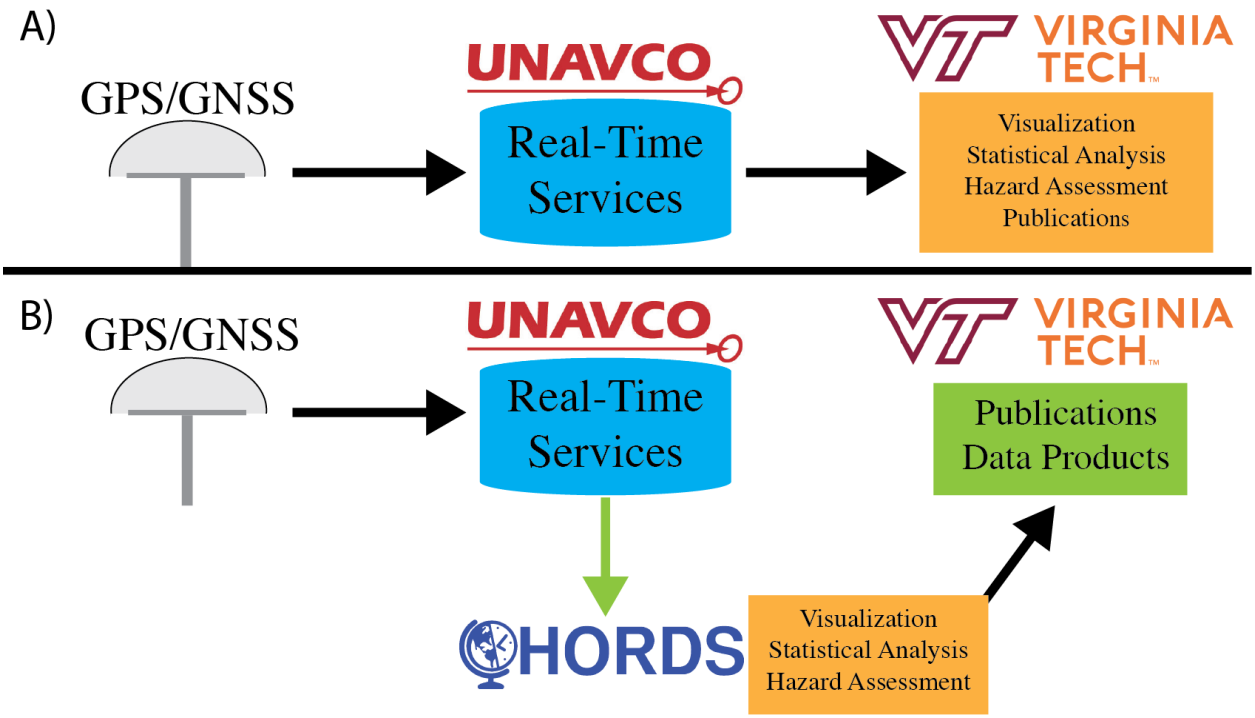

Figure 3.2: A representation of two different workflows for real-time GNSS data streaming through UNAVCO Real-time GNSS Data Services. The green arrow represents the processes executed in GNSS2CHORDS as explained in the methods section. (A) A typical workflow that does not utilize GNSS2CHORDS. In this case, institutions are responsible for all data analysis, visualization, and hazard assessment. (B) A revised workflow that employs GNSS2CHORDS such that a CHORDS portal can be utilized for data analysis, visualization, and automated hazard assessment.

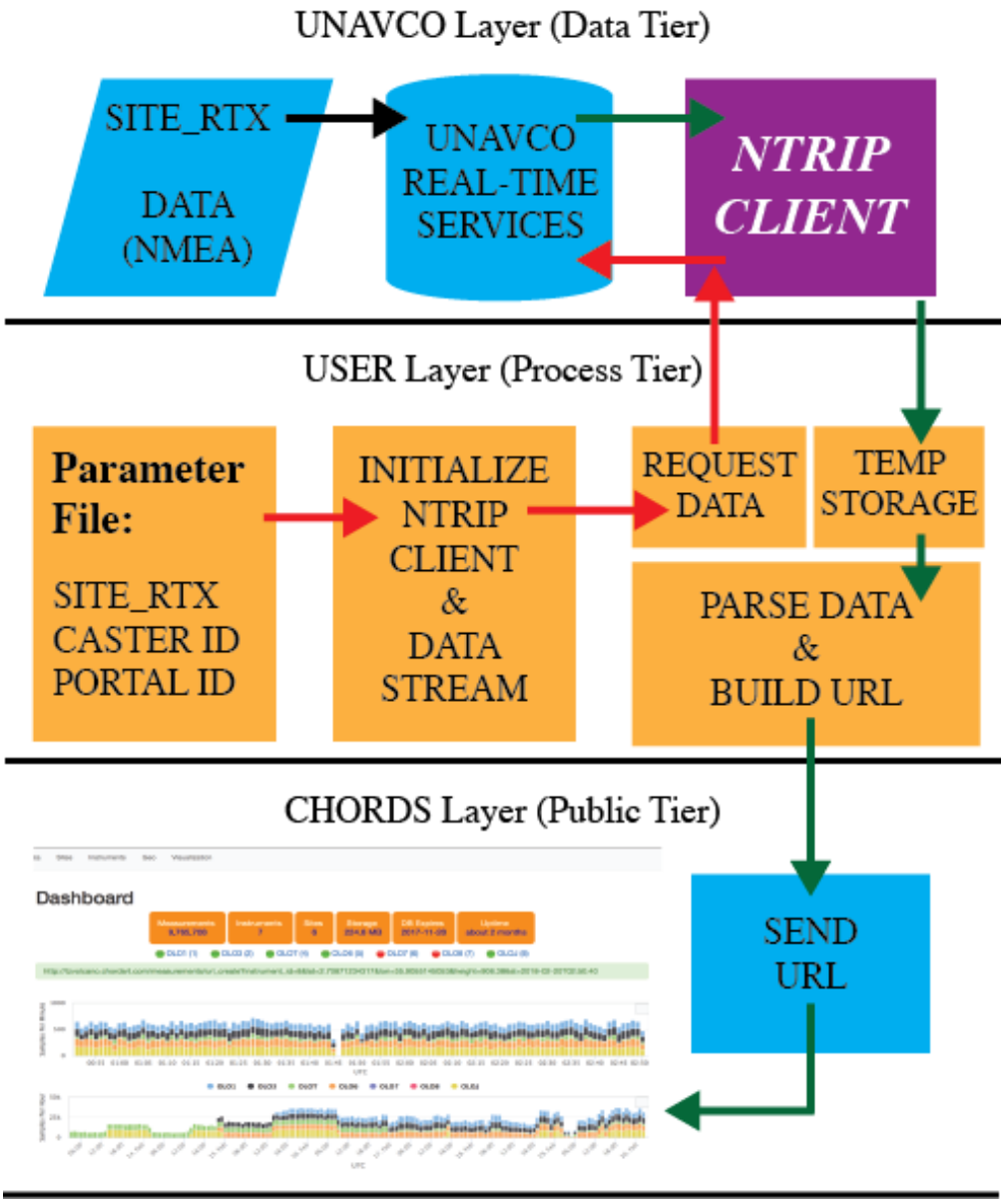

Figure 3.3: The workflow of the data broker application designed to connect UNAVCO Real-Time data services to an active CHORDS Portal. Presented in a format of a three tier architecture consisting of private data tier (not accessible to users), processing tier (can be edited by user), and the public tier (visible and accessible by user's audience). The data broker application begins with the user editing the parameter file and initializing the application. Following the red arrows first, the data broker application moves into the private or UNAVCO tier accessing the real-time data services. Next, following the green arrows the data is continuously streamed through the Ntrip Client and into the CHORDS Portal.

Bibliography

B Aagaard, S Kientz, M Knepley, L Strand, and C Williams. Pylith user manual, version 1.3, computational infrastructure for geodynamics. *URL: www. geodynamics. org/cig/-software/short/pylith/pylith_b ook-1.3. pdf*, 2008.

Brad Aagaard, Charles Williams, Matthew Knepley, Sue Kientz, and Leif Strand. Pylith. 2009.

J Albaric, J Perrot, J Déverchère, Anne Deschamps, B Le Gall, RW Ferdinand, Carole Petit, C Tiberi, C Sue, and M Songo. Contrasted seismogenic and rheological behaviours from shallow and deep earthquake sequences in the north tanzanian divergence, east africa. *Journal of African Earth Sciences*, 58(5):799–811, 2010.

T Apuani and C Corazzato. Numerical model of the stromboli volcano (italy) including the effect of magma pressure in the dyke system. *Rock Mechanics and Rock Engineering*, 42 (1):53–72, 2009.

G Baer, Y Hamiel, G Shamir, and R Nof. Evolution of a magma-driven earthquake swarm and triggering of the nearby oldoinyo lengai eruption, as resolved by insar, ground observations and elastic modeling, east african rift, 2007. *Earth and Planetary Science Letters*, 272(1):339–352, 2008.

G Berrino, G Corrado, G Luongo, and B Toro. Ground deformation and gravity changes accompanying the 1982 pozzuoli uplift. *Bulletin volcanologique*, 47(2):187–200, 1984.

Robert W Bialas, W Roger Buck, and Ran Qin. How much magma is required to rift a continent? *Earth and Planetary Science Letters*, 292(1-2):68–78, 2010.

Juliet Biggs, Falk Amelung, Noel Gourmelen, Timothy H Dixon, and Sang-Wan Kim. Insar observations of 2007 tanzania rifting episode reveal mixed fault and dyke extension in an immature continental rift. *Geophysical Journal International*, 179(1):549–558, 2009.

Juliet Biggs, Michael Chivers, and Michael C Hutchinson. Surface deformation and stress interactions during the 2007–2010 sequence of earthquake, dyke intrusion and eruption in northern tanzania. *Geophysical Journal International*, 195(1):16–26, 2013.

Thomas M Brocher. Empirical relations between elastic wavespeeds and density in the earth's crust. *Bulletin of the seismological Society of America*, 95(6):2081–2092, 2005.

WR Buck. The role of magma in the development of the afro-arabian rift system. *Geological Society, London, Special Publications*, 259(1):43–54, 2006.

Eric Calais. Tanzania continuous 2008: Engc, unavco, gps data set, 2008a.

Eric Calais. Tanzania continuous 2008: Ketc, unavco, gps data set, 2008b.

Eric Calais. Tanzania continuous 2008: Ldwc, unavco, gps data set, 2008c.

Eric Calais, Nicolas d'Oreye, Julie Albaric, Anne Deschamps, Damien Delvaux, Jacques Déverchere, Cynthia Ebinger, Richard W Ferdinand, François Kervyn, Athanas S Macheyeki, et al. Strain accommodation by slow slip and dyking in a youthful continental rift, east africa. *Nature*, 456(7223):783–787, 2008.

Eric Calais, Elifuraha Saria, and D. Sarah Stamps. Tanzania 2005, unavco, gps data set, 2014a.

Eric Calais, Elifuraha Saria, and D. Sarah Stamps. Tanzania 2006, unavco, gps data set, 2014b.

Valérie Cayol and François H Cornet. Effects of topography on the interpretation of the deformation field of prominent volcanoes—application to etna. *Geophysical Research Letters*, 25(11):1979–1982, 1998.

Giacomo Corti. Evolution and characteristics of continental rifting: Analog modeling-inspired view and comparison with examples from the east african rift system. *Tectonophysics*, 522:1–33, 2012.

MD Daniels, B Kerkez, V Chandrasekar, S Graves, DS Stamps, C Martin, A Botnick, M Dye, R Gooch, JR Jones, K Keiser, M Bartos, T Nguyen, R Collins, S Chen, and T Yang. Cloud-hosted real-time data services for the geosciences (chords) software (version 1.0.1), 2014.

M Diez, Peter Christopher La Femina, Charles B Connor, W Strauch, and V Tenorio. Evidence for static stress changes triggering the 1999 eruption of cerro negro volcano, nicaragua and regional aftershock sequences. *Geophysical Research Letters*, 32(4), 2005.

Diane I Doser and Dennis R Yarwood. Strike-slip faulting in continental rifts: examples from sabukia, east africa (1928), and other regions. *Tectonophysics*, 197(2-4):213–224, 1991.

AM Dziewonski, T-A Chou, and John H Woodhouse. Determination of earthquake source parameters from waveform data for studies of global and regional seismicity. *Journal of Geophysical Research: Solid Earth*, 86(B4):2825–2852, 1981.

CJ Ebinger, D Keir, ID Bastow, K Whaler, James OS Hammond, A Ayele, MS Miller, Christel Tiberi, and S Hautot. Crustal structure of active deformation zones in africa: Implications for global crustal processes. *Tectonics*, 36(12):3298–3332, 2017.

Cynthia J Ebinger, Jolante van Wijk, and Derek Keir. The time scales of continental rifting: Implications for global processes. *Geol. Soc. Am. Spec. Pap*, 500:371–396, 2013.

Göran Ekström, Meredith Nettles, and AM Dziewoński. The global cmt project 2004–2010: Centroid-moment tensors for 13,017 earthquakes. *Physics of the Earth and Planetary Interiors*, 200:1–9, 2012.

RMS Fernandes, JM Miranda, D Delvaux, DS Stamps, and E Saria. Re-evaluation of the kinematics of victoria block using continuous gnss data. *Geophysical Journal International*, 193(1):1–10, 2013.

TP Fischer, P Burnard, B Marty, DR Hilton, E Füri, F Palhol, ZD Sharp, and F Mangasini. Upper-mantle volatile chemistry at oldoinyo lengai volcano and the origin of carbonatites. *Nature*, 459(7243):77–80, 2009.

Ryan Gooch and Venkatachalam Chandrasekar. Integration of real-time weather radar data and internet of things with cloud-hosted real-time data services for the geosciences (chords). In *2017 IEEE International Geoscience and Remote Sensing Symposium (IGARSS)*, pages 4519–4521. IEEE, 2017.

Robert G Green, Robert S White, and Tim Greenfield. Motion in the north iceland volcanic rift zone accommodated by bookshelf faulting. *Nature Geoscience*, 7(1):29–33, 2014.

Agust Gudmundsson. Magma chambers: Formation, local stresses, excess pressures, and compartments. *Journal of Volcanology and Geothermal Research*, 237:19–41, 2012.

Ian J Hamling, Tim J Wright, Eric Calais, Laura Bennati, and Elias Lewi. Stress transfer between thirteen successive dyke intrusions in ethiopia. *Nature Geoscience*, 3(10):713–717, 2010.

Ramon F Hanssen. *Radar interferometry: data interpretation and error analysis*, volume 2. Springer Science & Business Media, 2001.

Oliver Heidbach, Mark Tingay, Andreas Barth, John Reinecker, Daniel Kurfeß, and Birgit Müller. Global crustal stress pattern based on the world stress map database release 2008. *Tectonophysics*, 482(1):3–15, 2010.

TA Herring, RW King, M Floyd, and SC McClusky. Introduction to gamit/globk, release 10.6, massachusetts institute of technology, http://geoweb.mit.edu/∼simon/gtgt/intro_gg.pdf, 2016.

Kathleen M Hodgkinson, David J Mencin, Karl Feaux, Charles Sievers, and Glen S Mattioli. Evaluation of earthquake magnitude estimation and event detection thresholds for real-time gnss networks: Examples from recent events captured by the network of the americas. *Seismological Research Letters*, 91(3):1628–1645, 2020.

Andreas Hoechner, Maorong Ge, Andrey Babeyko, and Stephan V Sobolev. Instant tsunami early warning based on real time gps–tohoku 2011 case study. *Natural Hazards and Earth System Sciences (NHESS)*, 13(5):1285–1292, 2013.

William Hutchison, Juliet Biggs, Tamsin A Mather, David M Pyle, Elias Lewi, Gezahegn Yirgu, Stefano Caliro, Giovanni Chiodini, Laura E Clor, and Tobias P Fischer. Causes of unrest at silicic calderas in the east african rift: New constraints from insar and soil-gas chemistry at aluto volcano, ethiopia. *Geochemistry, Geophysics, Geosystems*, 17(8): 3008–3030, 2016.

Andy Jarvis, Hannes I Reuter, Andy Nelson, Edward Guevara, et al. Hole-filled srtm for the globe version 4, available from the cgiar-csi srtm 90m database, 2008.

J Robert Jones, D Sarah Stamps, Christelle Wauthier, Elifuraha Saria, and Juliet Biggs. Evidence for slip on a border fault triggered by magmatic processes in an immature continental rift. *Geochemistry, Geophysics, Geosystems*, 20(5):2515–2530, 2019.

Jeffrey A Karson and Patchin C Curtis. Tectonic and magmatic processes in the eastern branch of the east african rift and implications for magmatically active continental rifts. *Journal of African Earth Sciences (and the Middle East)*, 8(2):431–453, 1989.

Derek Keir, Ian J Hamling, Atalay Ayele, Eric Calais, Cindy Ebinger, Tim J Wright, Eric Jacques, Kassim Mohamed, James OS Hammond, Manahloh Belachew, et al. Evidence for focused magmatic accretion at segment centers from lateral dike injections captured beneath the red sea rift in afar. *Geology*, 37(1):59–62, 2009.

Branko Kerkez, Michael Daniels, Sara Graves, V Chandrasekar, Ken Keiser, Charlie Martin, Michael Dye, Manil Maskey, and Frank Vernon. Cloud hosted real-time data services for the geosciences (chords). *Springer Berlin Heidelberg*, 2016.

Matthieu Kervyn, Gerald GJ Ernst, Jörg Keller, R Greg Vaughan, Jurgis Klaudius, Evelyne Pradal, Frederic Belton, Hannes B Mattsson, Evelyne Mbede, and Patric Jacobs. Fundamental changes in the activity of the natrocarbonatite volcano oldoinyo lengai, tanzania. *Bulletin of Volcanology*, 72(8):913–931, 2010.

Geoffrey CP King, Ross S Stein, and Jian Lin. Static stress changes and the triggering of earthquakes. *Bulletin of the Seismological Society of America*, 84(3):935–953, 1994.

MOGI Kiyoo. Relations between the eruptions of various volcanoes and the deformations of the ground surfaces around them. *Earthq Res Inst*, 36:99–134, 1958.

Alexander Koptev, Eric Calais, Evgueni Burov, Sylvie Leroy, and Taras Gerya. Dual continental rift systems generated by plume–lithosphere interaction. *Nature Geoscience*, 8(5): 388–392, 2015.

Rodrigo Leandro, Herbert Landau, Markus Nitschke, Markus Glocker, Stephan Seeger, Xiaoming Chen, Alois Deking, Mohamed BenTahar, Feipeng Zhang, Kendall Ferguson, et al.

Rtx positioning: the next generation of cm-accurate real-time gnss positioning. In *ION GNSS*, volume 14601475, 2011.

Hyunwoo Lee, James D Muirhead, Tobias P Fischer, Cynthia J Ebinger, Simon A Kattenhorn, Zachary D Sharp, and Gladys Kianji. Massive and prolonged deep carbon emissions associated with continental rifting. *Nature Geoscience*, 9(2):145, 2016.

Hyunwoo Lee, Tobias P Fischer, James D Muirhead, Cynthia J Ebinger, Simon A Kattenhorn, Zachary D Sharp, Gladys Kianji, Naoto Takahata, and Yuji Sano. Incipient rifting accompanied by the release of subcontinental lithospheric mantle volatiles in the magadi and natron basin, east africa. *Journal of Volcanology and Geothermal Research*, 346: 118–133, 2017.

Khumo Leseane, Estella A Atekwana, Kevin L Mickus, Mohamed G Abdelsalam, Elisha M Shemang, and Eliot A Atekwana. Thermal perturbations beneath the incipient okavango rift zone, northwest botswana. *Journal of Geophysical Research: Solid Earth*, 120(2): 1210–1228, 2015.

Jian Lin and Ross S Stein. Stress triggering in thrust and subduction earthquakes and stress interaction between the southern san andreas and nearby thrust and strike-slip faults. *Journal of Geophysical Research: Solid Earth*, 109(B2), 2004.

Didier Massonnet and Kurt L Feigl. Radar interferometry and its application to changes in the earth's surface. *Reviews of geophysics*, 36(4):441–500, 1998.

James D Muirhead, Simon A Kattenhorn, and Nicolas Le Corvec. Varying styles of magmatic strain accommodation across the east african rift. *Geochemistry, Geophysics, Geosystems*, 16(8):2775–2795, 2015.

JD Muirhead, SA Kattenhorn, H Lee, S Mana, BD Turrin, TP Fischer, G Kianji, E Dindi, and DS Stamps. Evolution of upper crustal faulting assisted by magmatic volatile release during early-stage continental rift development in the east african rift. *Geosphere*, 12(6): 1670–1700, 2016.

Concetta Nostro, Ross S Stein, Massimo Cocco, Maria Elina Belardinelli, and Warner Marzocchi. Two-way coupling between vesuvius eruptions and southern apennine earthquakes, italy, by elastic stress transfer. *Journal of Geophysical Research: Solid Earth*, 103(B10): 24487–24504, 1998.

Yoshimitsu Okada. Surface deformation due to shear and tensile faults in a half-space. *Bulletin of the seismological society of America*, 75(4):1135–1154, 1985.

CM Petibon, BA Kjarsgaard, GA Jenner, and SE Jackson. Phase relationships of a silicate-bearing natrocarbonatite from oldoinyo lengai at 20 and 100 mpa. *Journal of Petrology*, 39(11-12):2137–2151, 1998.

MC Reiss, JD Muirhead, AS Laizer, F Link, EO Kazimoto, CJ Ebinger, and G Rümpker. The impact of complex volcanic plumbing on the nature of seismicity in the developing magmatic natron rift, tanzania. front. *Earth Sci*, 8:609805, 2021.

Uwe Ring, Christian Betzler, and Damian Delvaux. Normal vs. strike-slip faulting during rift development in east africa: the malawi rift. *Geology*, 20(11):1015–1018, 1992.

S Roecker, C Ebinger, Christel Tiberi, G Mulibo, R Ferdinand-Wambura, K Mtelela, G Kianji, A Muzuka, Stephanie Gautier, Julie Albaric, et al. Subsurface images of the eastern rift, africa, from the joint inversion of body waves, surface waves and gravity: investigating the role of fluids in early-stage continental rifting. *Geophysical Journal International*, 210(2):931–950, 2017.

Allan M Rubin and David D Pollard. Dike-induced faulting in rift zones of iceland and afar. *Geology*, 16(5):413–417, 1988.

E Saria, E Calais, Z Altamimi, P Willis, and H Farah. A new velocity field for africa from combined gps and doris space geodetic solutions: Contribution to the definition of the african reference frame (afref). *Journal of Geophysical Research: Solid Earth*, 118(4): 1677–1697, 2013.

E Saria, E Calais, DS Stamps, D Delvaux, and CJH Hartnady. Present-day kinematics of the east african rift. *Journal of Geophysical Research: Solid Earth*, 119(4):3584–3600, 2014.

David R Sherrod, Masota M Magigita, and Shimba Kwelwa. Geologic map of oldonyo lengai (oldoinyo lengai) volcano and surroundings, arusha region, united republic of tanzania. Technical report, US Geological Survey, 2013.

D Sarah Stamps, Eric Calais, Elifuraha Saria, Chris Hartnady, Jean-Mathieu Nocquet, Cynthia J Ebinger, and Rui M Fernandes. A kinematic model for the east african rift. *Geophysical Research Letters*, 35(5), 2008.

DS Stamps, LM Flesch, and E Calais. Lithospheric buoyancy forces in africa from a thin sheet approach. *International Journal of Earth Sciences*, 99(7):1525–1533, 2010.

DS Stamps, LM Flesch, E Calais, and A Ghosh. Current kinematics and dynamics of africa and the east african rift system. *Journal of Geophysical Research: Solid Earth*, 119(6): 5161–5186, 2014.

DS Stamps, E Saria, KH Ji, JR Jones, D Ntambila, MD Daniels, and D Mencin. Real-time data from the tanzania volcano observatory at the ol doinyo lengai volcano in tanzania (tzvolcano), 2016.

D.S. Stamps, C. Kreemer, R. Fernandes, T.A. Rajaonarison, and G. Rambolamanana. Redefining East African Rift System kinematics. *Geology*, 49(2):150–155, 09 2021. ISSN 0091-7613. doi: 10.1130/G47985.1. URL https://doi.org/10.1130/G47985.1.

Ross S Stein. The role of stress transfer in earthquake occurrence. *Nature*, 402(6762): 605–609, 1999.

Ross S Stein, Geoffrey CP King, and Jian Lin. Change in failure stress on the southern san andreas fault system caused by the 1992 magnitude= 7.4 landers earthquake. *Science*, 258 (5086):1328–1332, 1992.

Ross S Stein, Aykut A Barka, and James H Dieterich. Progressive failure on the north anatolian fault since 1939 by earthquake stress triggering. *Geophysical Journal International*, 128(3):594–604, 1997.

Andrea Stürze, Leos Mervart, Georg Weber, Axel Rülke, Erwin Wiesensarter, and Peter Neumaier. The new version 2.12 of bkg ntrip client (bnc). In *Geophys. Res. Abstr*, volume 18, page 12012, 2016.

Paul Tapponnier, Rolando Armijo, Isabelle Manighetti, and Vincent Courtillot. Bookshelf faulting and horizontal block rotations between overlapping rifts in southern afar. *Geophysical Research Letters*, 17(1):1–4, 1990.

Shinji Toda, Ross S Stein, Keith Richards-Dinger, and Serkan B Bozkurt. Forecasting the evolution of seismicity in southern california: Animations built on earthquake stress transfer. *Journal of Geophysical Research: Solid Earth*, 110(B5), 2005.

Shinji Toda, Ross S Stein, Volkan Sevilgen, and Jian Lin. Coulomb 3.3 graphic-rich deformation and stress-change software for earthquake, tectonic, and volcano research and teaching—user guide. *US Geological Survey open-file report*, 1060(2011):63, 2011.

E Venzke. Global volcanism program. *Volcanoes of the World*, 4:1, 2013.

C Wauthier, B Smets, and D Keir. Diking-induced moderate-magnitude earthquakes on a youthful rift border fault: The 2002 nyiragongo-kalehe sequence, dr congo. *Geochemistry, Geophysics, Geosystems*, 16(12):4280–4291, 2015.

Christelle Wauthier, Diana C Roman, and Michael P Poland. Moderate-magnitude earthquakes induced by magma reservoir inflation at kilauea volcano, hawai'i. *Geophysical Research Letters*, 40(20):5366–5370, 2013.

Alexander Weinstein, Sarah J Oliva, Cynthia J Ebinger, S Roecker, Christel Tiberi, M Aman, C Lambert, E Witkin, Julie Albaric, Stephanie Gautier, et al. Fault-magma interactions during early continental rifting: Seismicity of the m agadi-n atron-m anyara basins, a frica. *Geochemistry, Geophysics, Geosystems*, 18(10):3662–3686, 2017.

Mark D Wilkinson, Michel Dumontier, IJsbrand Jan Aalbersberg, Gabrielle Appleton, Myles Axton, Arie Baak, Niklas Blomberg, Jan-Willem Boiten, Luiz Bonino da Silva Santos, Philip E Bourne, et al. The fair guiding principles for scientific data management and stewardship. *Scientific data*, 3(1):1–9, 2016.

Appendices

Appendix A

Chpt. 1 Supporting Information

A.1 Introduction

This project uses (1) the USGS open source program Coulomb 3.4 to calculate the Coulomb stress changes and surface displacements associated with fault slip and magmatic reservoir changes, and (2) GAMIT-GLOBK [Herring et al., 2016] to produce the timeseries presented for Engaresero, Lwondolwo, and Ketumbeine semi-continuous sites in 2008. The Coulomb 3.4 input files are ascii files (.inp format). Timeseries produced by GAMIT-GLOBK use doubly-differenced GPS phase observations for calculations of the daily positions given and are provided as ascii files (.pos format). We correct for Earth tides, polar tides, and ocean loading, and employ 15 regional sites and 24 global sites to stabilize the solution.

Our supplementary materials also include an InSAR interferogram from two ENVISAT satellite passes in 2008 (18 February - 15 September) after the initial rifting events of 2007 and the slip event detected at ENGC in January 2008. InSAR does not provide us with mm horizontal measurements, but the large area coverage and near-cm accuracy for the line-of-sight displacements. These observations can be useful in identifying large scale de- formation patterns. When combining multiple interferograms from different angles it is also possible to achieve higher precision for horizontal and vertical motion [Hanssen, 2001]. In the interferogram presented, precise ENVISAT orbits (European Space Agency, ESA) have been used to remove orbital effects and a SRTM DEM (30 meters resolution) is used

to remove topographic effects following Jarvis et al. [2008]. Atmospheric corrections were not applied to the InSAR interferogram. To confirm that the observed phase changes were due to actual deformation and not atmospheric artifacts, the interferogram was inspected through a pairwise logic approach checking other interferogram pairs for atmospheric artifacts [Massonnet and Feigl, 1998]. Since these passes occur after the distinct slip event measured ∼30 January 2008 at ENGC, we do not include it in our primary discussion in the manuscript. However, there are incoherent fringes near the 'volcano adjacent' section of the Natron Fault that could be representative of slip continuing on the Natron Fault after the ∼30 January 2008 signal at ENGC.

A.2 Datasets

Datasets S1 - S3: Model input files used in the program Coulomb 3.4 in ascii format (.inp). These files provide the information used in calculating Coulomb stress changes in the region and on receiver faults. The first file (S1) provides the input for the cumulative events from the 2007-2008 Tanzanzia rifting event with the Natron fault tapered 1 km x 1 km. The second file (S2) is the input for the individual events occurring at Gelai. The third file (S3) provides the input for the isolated events at Ol Doinyo Lengai in 2008 with the Natron fault tapered 1 km x 1 km.

Datasets S4 - S6: These are the output files for Coulomb 3.4 for the calculations of stress changes on the fault with the default values chosen for the calculations provided as ascii files. These files provide the calculated normal stress in bars on the chosen receiver Natron fault and are divided as follows: Rows are fault segments. Columns 1-7 are the location and geometry of the fault segment. Columns 8-9 are the amount of slip imposed in the input file. Columns 10-18 are the calculated various stress changes in bars with the primary Coulomb

normal stress change in Column 12. Column 19-20 are the element conditions including rake and coupling.

Dataset S7: The timeseries file (.pos) created for the Engaresero (ENGC) semi-continuous GPS site.

Dataset S8: The timeseries file (.pos) created for the Ketumbaine (KETC) semi-continuous GPS site.

Dataset S9: The timeseries file (.pos) created for the Londolwo (LDWC) semi-continuous GPS site.

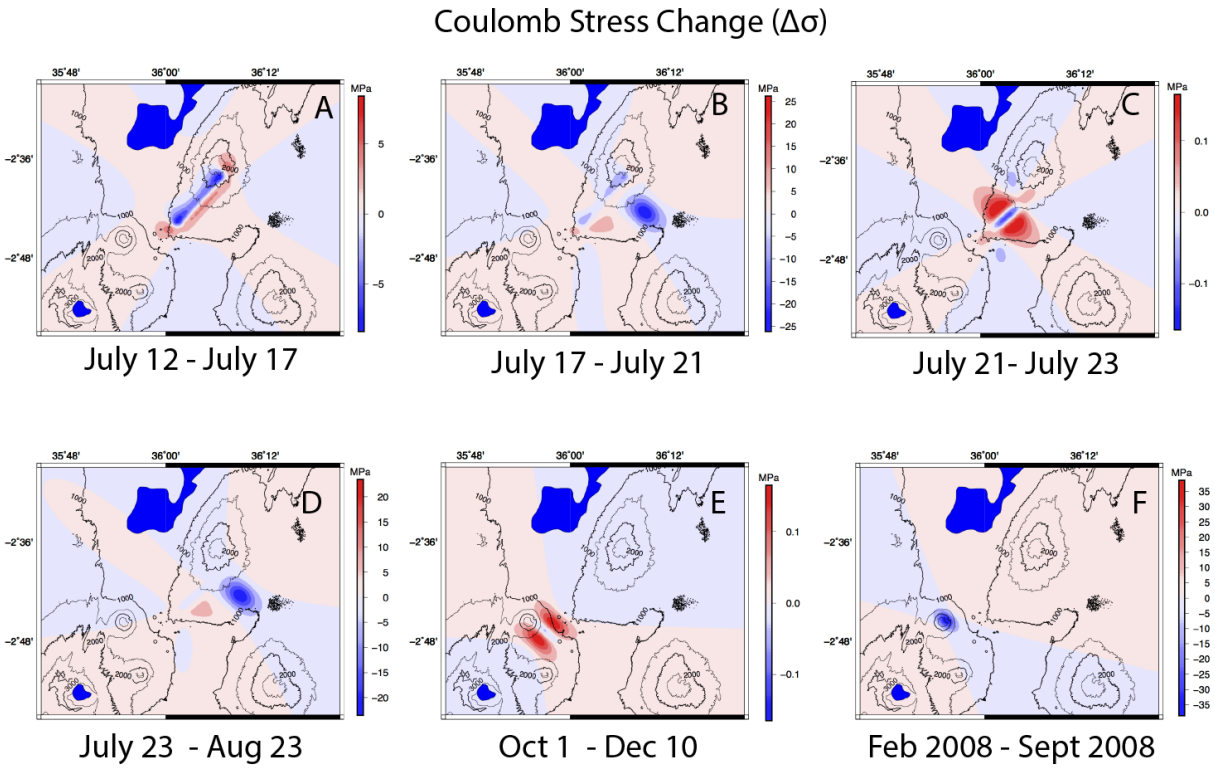

Figure A.1: Calculated Coulomb stress change associated with the isolated events 2007-2008 Tanzania rifting crisis. A-F defines the active stage modeled corresponding to Table 1.2 in the manuscript. Warmer colors represent positive Coulomb stress changes and cooler colors represent negative Coulomb stress changes.

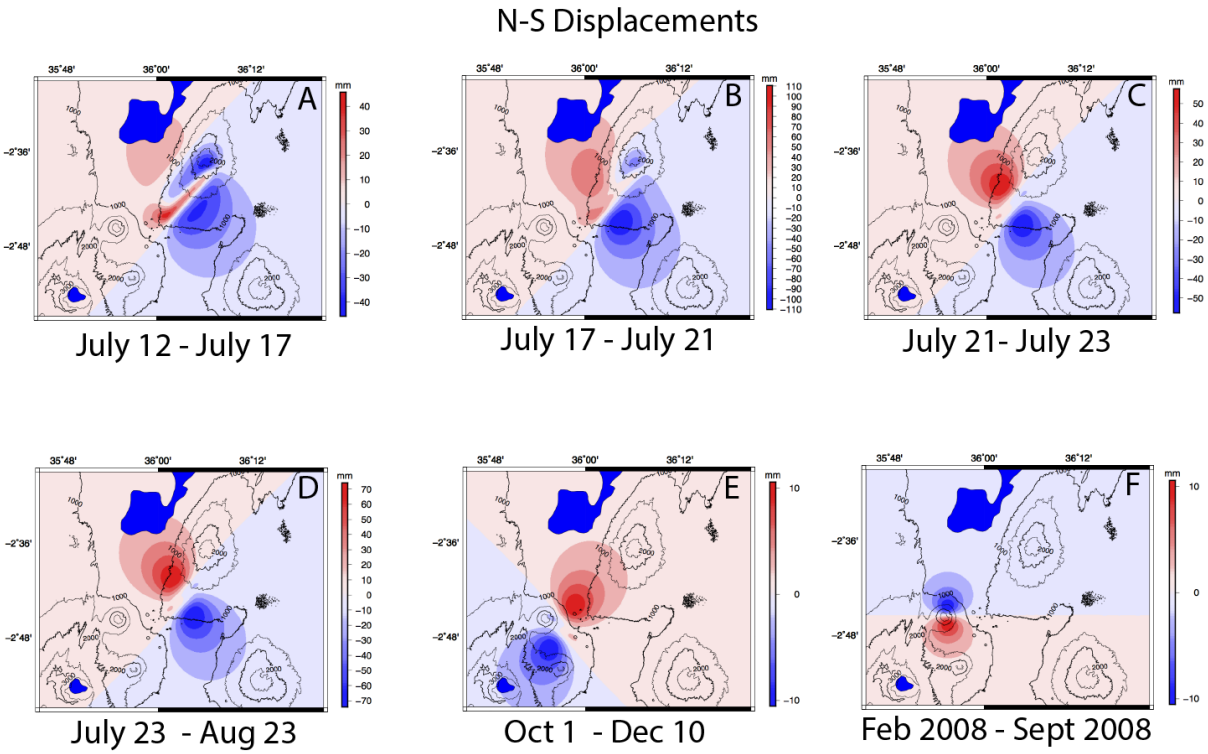

Figure A.2: Calculated displacements in the N-S component associated with the isolated events from the 2007-2008 Tanzania Rifting crisis. A-F defines the active stage modeled corresponding to Table 1.2 in the manuscript. Warmer colors represent displacements in the northern direction and cooler colors represent displacements in the southern direction.

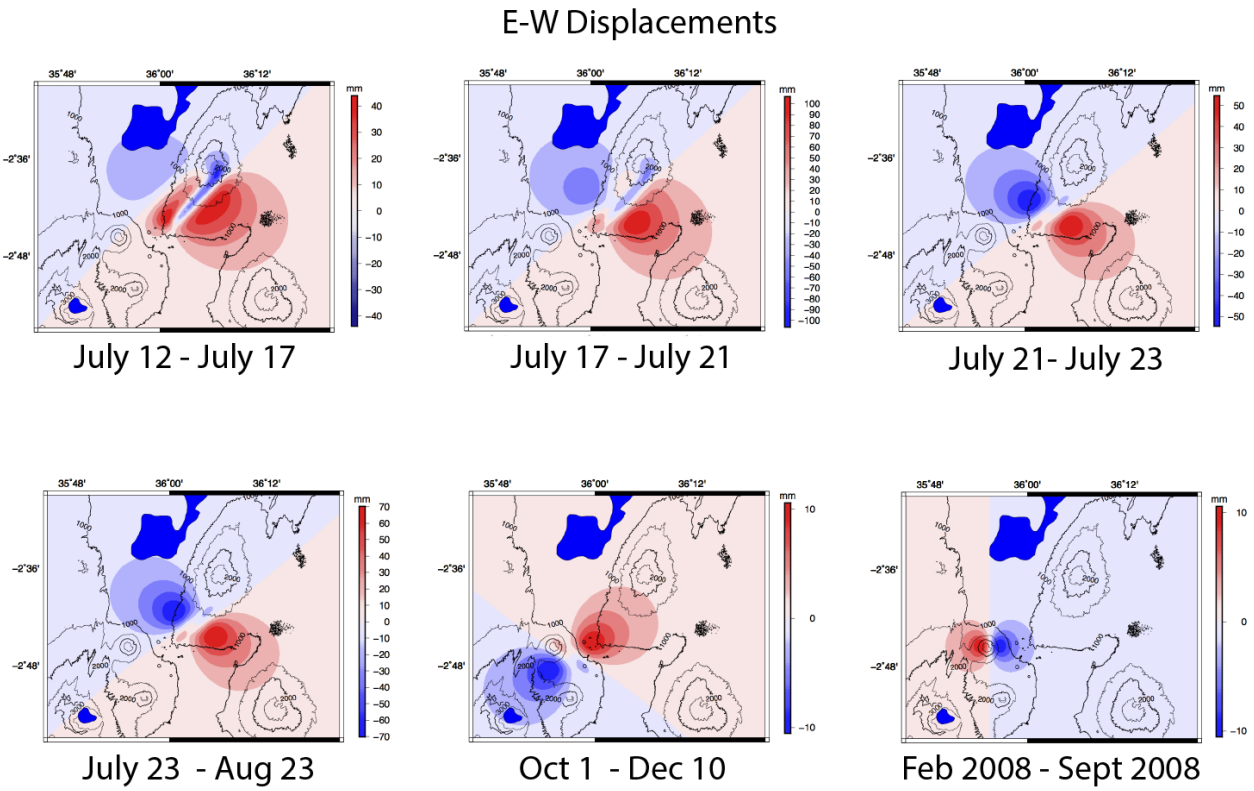

Figure A.3: Calculated displacements in the E-W component associated with the isolated events from the 2007-2008 Tanzania Rifting crisis. A-F defines the active stage modeled corresponding to Table 1.2 in the manuscript. Warmer colors represent displacements in the eastern direction and cooler colors represent displacements in the western direction.

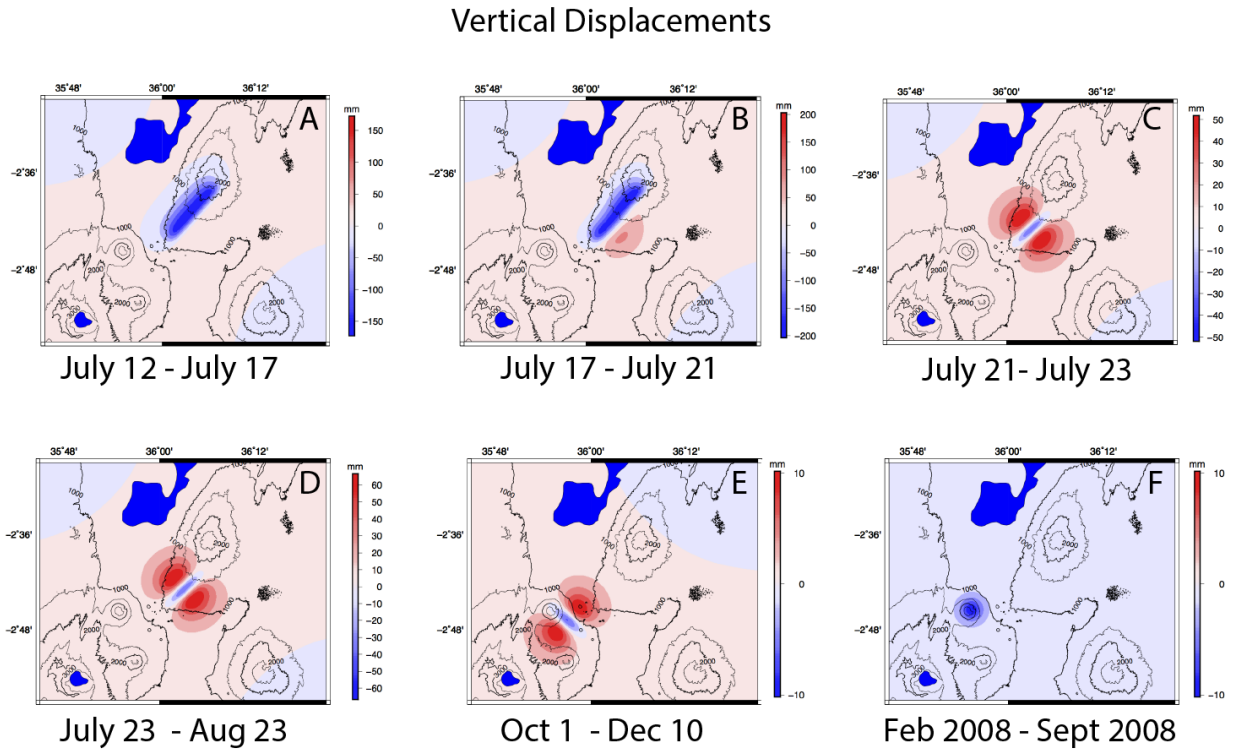

Figure A.4: Calculated displacements in the E-W component associated with the isolated events from the 2007-2008 Tanzania Rifting crisis. A-F defines the active stage modeled corresponding to Table 1.2 in the manuscript. Warmer colors represent displacements in the eastern direction and cooler colors represent displacements in the western direction.

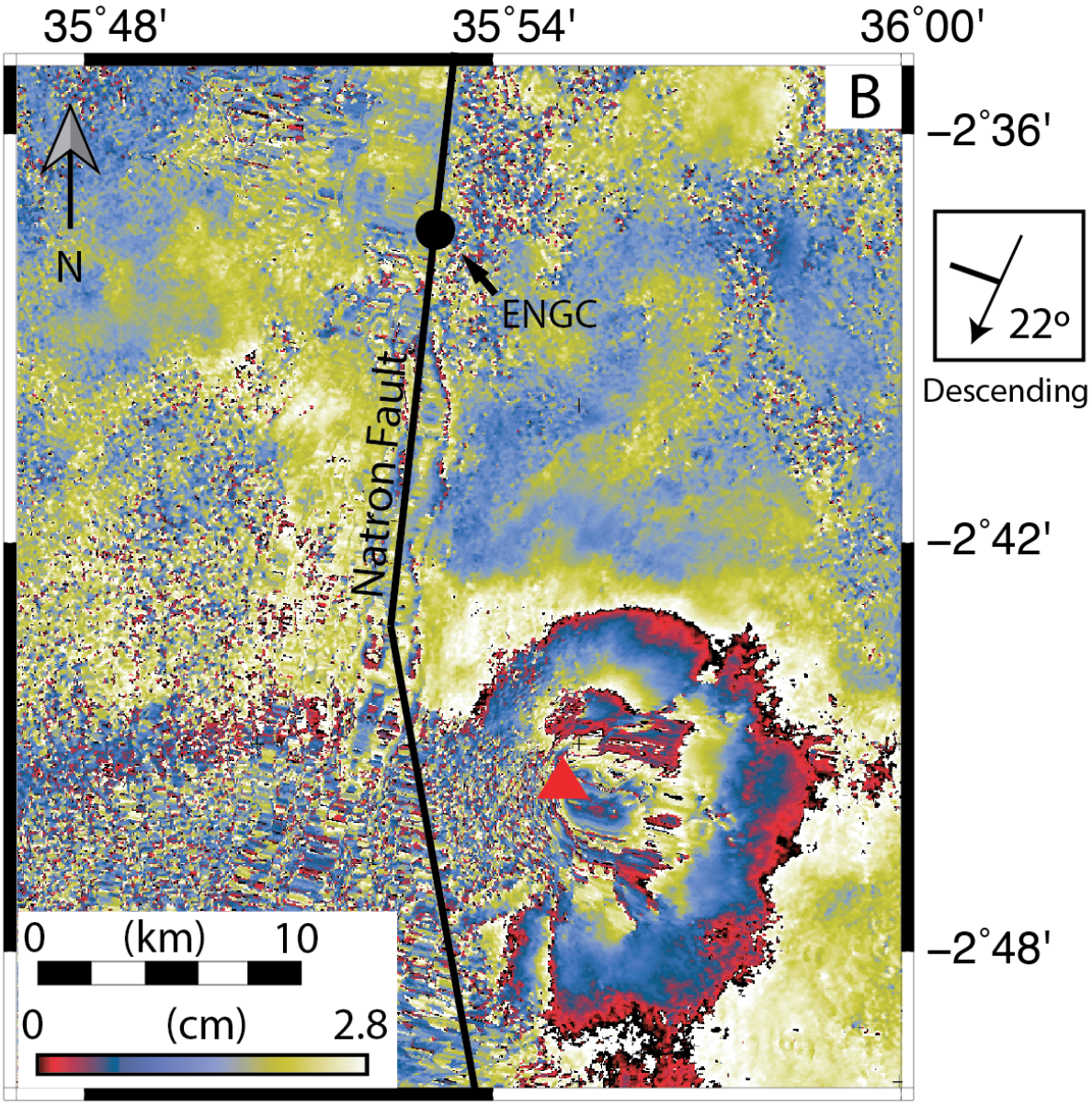

Figure A.5: An InSAR interferogram processed from two ENVISAT passes in 2008 (18 February - 15 September 2008) after the initial rifting events of 2007 (Figure 1.3B). The red triangle represents the edifice of the volcano Ol Doinyo Lengai and the black dot is the location of the semi-continuous GPS site ENGC.

Appendix B

Chpt. 2 Supporting Information

B.1 Introduction

Here we present supplementary information for our PyLith modeling. We explain in more detail the steps and results of our boundary condition tests. We also include examples of our PyLith input and parameter files that are used to create the models tested in the main manuscript.

B.2 Boundary Condition Tests

For our boundary condition tests we test four different types of boundaries: Dirichlet, Neumann, Free-surface, and Rolling Boundaries. Each of these values affect how the solution of our PyLith simulations are resolved at the edges of our models. We test these boundaries to avoid edge effects on the solution calculated on the surface of the model and on the Natron Fault modeled segments. Dirichlet boundaries force the displacement and strain solution to approach zero at the edge of the model and does not constrain the stress solution at the edges. Neumann boundaries force the stress solution to approach zero at the boundaries but does not constrain the strain solution. A free-surface boundary does not constrain either stress or strain solution allowing the values to continue outside of the model domain. Rolling boundaries are a combination of Dirichlet and Neumann boundaries allowing stress

and strain solutions to continue in certain directions and constrains the solution in the other directions to zero.

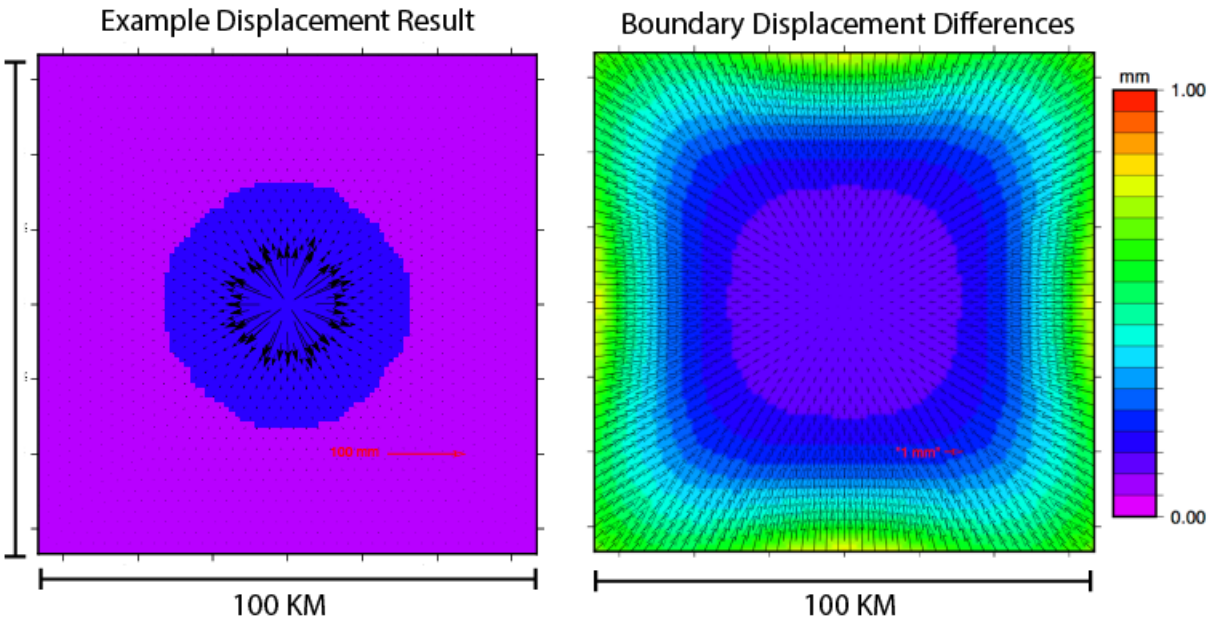

Figure B.1: Example of the results of our boundary condition tests conducted.

Figure B.2: The PyLith surface displacement outputs that we use as one method of model validation visualized by Paraview. The model outputs are for an isolated magma reservoir deflation event with a radius of 133 m. We present examples of the outputs for no topography compared with topography A) no topography model with a deflation amount of ∼20 cm. B) topography model with a deflation amount of ∼20 cm. Displacement values on the right are in meters. We calculate identical displacement values for the models with a magma reservoir with a radius of 290 m.

B.3 Example PyLith Files

Here we present example pylith files to create a simulation for a magma reservoir deflation event with a reservoir size of 133 m. There are two main configuration files as well as files used for material information called spatialdb files.

Configuration File 1

```
#Pure elastic problem with simple sphere and fault segments in block

#to run
# pylith sphere_fault_simple.cfg

#this program is not selfcontained
#it needs pylithapp.cfg

[pylithapp.timedependent.formulation.time_step]
# Define the total time for the simulation.
total_time = 0.0*year
# Define an appropriate time step for simulations. Important for
# nondimensionalization of velocities and slip rates.
dt = 1.0*year

[pylithapp.timedependent]
# Set bc to an array of all boundary conditions: 'edge_xpos','edge_xneg', '
    edge_ypos',
# 'edge_yneg', 'edge_zneg', 'magma_chamber' 'fault_edge', 'fault'.
bc = [edge_xpos,edge_xneg,edge_ypos,edge_yneg,edge_zneg,resevior_edge]

#set interfaces to an array of 1 for fault
interfaces=[fault]
```

```
23
24 [pylithapp.timedependent.implicit]
25 # Set the output to an array of 3 output managers.
26 # We will output the solution over the domain, the ground surface, and the
27 # wall of the magma chamber.
28 output = [domain, edge_zpos, resevior_edge, fault]
29
30 # Set subdomain components to OutputSolnSubset (boundary of the domain).
31 output.edge_zpos = pylith.meshio.OutputSolnSubset
32 output.edge_zpos.label = edge_zpos
33 output.resevior_edge = pylith.meshio.OutputSolnSubset
34 output.resevior_edge.label = resevior_edge
35
36 # ----------------------------------------------------------------------
37 # boundary conditions
38 # ----------------------------------------------------------------------
39 # Set the parameters for Dirichlet boundary conditions applied on the
40 # -x, +x, -y, +y, and -z faces of the box.
41 #
42 # We fix each degree of freedom in the direction perpendicular to the
43 # boundary.
44 #
45 # For all boundaries, we retain the default ZeroDispDB, which specifies
46 # a zero value.
47 #
48
49 # The label corresponds to the name of the nodeset in Trelis.
50
51 # +x face
52 [pylithapp.timedependent.bc.edge_xpos]
53 bc_dof = [0]
```

```
label = edge_xpos

# -x face
[pylithapp.timedependent.bc.edge_xneg]
bc_dof = [0]
label = edge_xneg

# +y face
[pylithapp.timedependent.bc.edge_ypos]
bc_dof = [1]
label = edge_ypos

# -y face
[pylithapp.timedependent.bc.edge_yneg]
bc_dof = [1]
label = edge_yneg

# -z face
[pylithapp.timedependent.bc.edge_zneg]
bc_dof = [2]
label = edge_zneg

# Magma chamber. We must first change the default BC type to Neumann.
[pylithapp.timedependent.bc]
resevior_edge = pylith.bc.Neumann

# We use a spatial database to specify the tractions.
[pylithapp.timedependent.bc.resevior_edge]
label = resevior_edge
db_change = spatialdata.spatialdb.SimpleDB
db_change.label = Neumann BC on resevior_edge
```

```
85 db_change.iohandler.filename = ../spatialdb/magma_pressure.spatialdb
86
87 # We must specify quadrature information for the cell faces.
88 quadrature.cell = pylith.feassemble.FIATSimplex
89 quadrature.cell.dimension = 2
90 quadrature.cell.quad_order = 2
91
92 [pylithapp.timedependent.interfaces.fault]
93 # The label corresponds to the name of the nodeset in CUBIT.
94 label = fault
95 edge = fault_edge
96 #id =2
97 # We must define the quadrature information for fault cells.
98 # The fault cells are 2D (surface).
99 quadrature.cell = pylith.feassemble.FIATSimplex
100 quadrature.cell.dimension = 2
101
102 [pylithapp.timedependent.interfaces.fault.eq_srcs.rupture.slip_function]
103 slip.label = fault slip
104 slip.iohandler.filename = ../spatialdb/faultslip.spatialdb
105 slip.query_type = nearest
106
107 slip_time.label  = Slip initiation time
108 slip_time.iohandler.filename = ../spatialdb/sliptime.spatialdb
109
110 # ----------------------------------------------------------------------
111 # output
112 # ----------------------------------------------------------------------
113 # Give basename for h5 domain output of solution over domain.
114 # Give basename for VTK domain output of solution over domain.
115
```

```
116 [pylithapp.problem.formulation.output.domain]
117 writer.filename = ../output/no_topo_r133m_domain_def.vtk
118
119 [pylithapp.problem.formulation.output.edge_zpos]
120 writer.filename = ../output/no_topo_r133m_surface_def.vtk
121
122 # Give basename for VTK domain output of solution over ground surface.
123 [pylithapp.problem.formulation.output.resevior_edge]
124 # Name of nodeset for ground surface.
125 writer.filename = ../output/no_topo_r133m_resevior_def.vtk
126
127 [pylithapp.timedependent.materials.domain.output]
128 # Average values over quadrature points.
129 cell_filter = pylith.meshio.CellFilterAvg
130 writer.filename = ../output/no_topo_r133m_domain_materials_def.vtk
131
132 [pylithapp.problem.interfaces.fault.output]
133 writer = pylith.meshio.DataWriterHDF5
134 writer.filename = ../output/no_topo_r133m_fault_output_def.h5
135 # We again switch the writer to produce HDF5 output.
136 #writer = pylith.meshio.DataWriterHDF5
137 #writer.filename = output/natron_fault_domain_stress.vtk
138
139 #[pylithapp.problem.formulation.output.edge_zpos]
140 #writer = pylith.meshio.DataWriterHDF5
141 #writer.filename = output/natron_test_surface.h5
142
143 # Give basename for h5 domain output of solution over ground surface.
144 #[pylithapp.problem.formulation.output.magma_chamber]
145 # Name of nodeset for ground surface.
146 #writer = pylith.meshio.DataWriterHDF5
```

```
147 #writer.filename = output/natron_test_chamber.h5
```

Configuration File 2

```
1 [pylithapp]
2
3 # This is not a self-contained simulation configuration file. This
4 # file only specifies the general parameters common to the simulations
5 # in this directory.
6
7 # ----------------------------------------------------------------------
8 # journal
9 # ----------------------------------------------------------------------
10 # Turn on some journals to show progress.
11 [pylithapp.journal.info]
12 timedependent = 1
13 greensfns = 1
14 implicit = 1
15 petsc = 1
16 solverlinear = 1
17 meshiocubit = 1
18 implicitelasticity = 1
19 faultcohesivekin = 1
20 fiatlagrange = 1
21 pylithapp = 1
22 materials = 1
23
24 # ----------------------------------------------------------------------
25 # mesh_generator
26 # ----------------------------------------------------------------------
27 [pylithapp.mesh_generator]
28 # Change the default mesh reader to the CUBIT reader.
```

```
29 reader = pylith.meshio.MeshIOCubit
30
31 # Optimize ordering of mesh cells and vertices using reverse
32 # Cuthill-KcKee algorithm.
33 reorder_mesh = True
34
35 [pylithapp.mesh_generator.reader]
36 # Set filename of mesh to import.
37 filename = ../mesh/natron_no_topo_mesh_dense.exo
38 coordsys = spatialdata.geocoords.CSGeoProj
39 coordsys.space_dim = 3
40 coordsys.datum_horiz = WGS84
41 coordsys.datum_vert = mean sea level
42 coordsys.projector.projection = tmerc
43 coordsys.projector.proj_options = +lon_0=35.914 +lat_0=-2.764 +k=.9996
44
45 # ----------------------------------------------------------------------
46 # materials
47 # ----------------------------------------------------------------------
48 [pylithapp.problem]
49
50 # Set materials to an array of 2 materials:
51 #   'domain, magma_body'
52 materials = [domain, magma_body]
53
54 [pylithapp.problem.materials.domain]
55 label = domain
56 id = 1
57 db_properties = spatialdata.spatialdb.SimpleDB
58 db_properties.label = Properties for outer elastic material
59 db_properties.iohandler.filename = ../spatialdb/const_elastic.spatialdb
```

```
quadrature.cell = pylith.feassemble.FIATSimplex
quadrature.cell.dimension = 3

[pylithapp.problem.materials.magma_body]
label = resevior
id = 2
db_properties = spatialdata.spatialdb.SimpleDB
db_properties.label = Properties for lengai elastic material
db_properties.iohandler.filename = ../spatialdb/const_elastic.spatialdb
quadrature.cell = pylith.feassemble.FIATSimplex
quadrature.cell.dimension = 3

# ----------------------------------------------------------------------
# PETSc
# ----------------------------------------------------------------------
# Set the solver options.
# Set PyLith problem formulation settings for Field Split.
[pylithapp.problem.formulation]
split_fields = True
matrix_type = aij
use_custom_constraint_pc = True

[pylithapp.petsc]
# Preconditioner settings.
fs_pc_type = fieldsplit
fs_pc_use_amat = true
fs_pc_fieldsplit_type = multiplicative
fs_fieldsplit_displacement_pc_type = ml
fs_fieldsplit_displacement_ksp_type = preonly
fs_fieldsplit_lagrange_multiplier_pc_type = jacobi
fs_fieldsplit_lagrange_multiplier_ksp_type = preonly
```

```
pc_type = ml

# Convergence parameters.
ksp_rtol = 1.0e-10
ksp_atol = 1.0e-12
ksp_max_it = 1000
ksp_gmres_restart = 1000

# Linear solver monitoring options.
ksp_monitor = true
ksp_view = true
ksp_converged_reason = true
ksp_error_if_not_converged = true
```

Spatialdb Example

```
// -*- C++ -*- (tell Emacs to use C++ mode for syntax highlighting)
//
// This spatial database specifies the distribution of material
// properties. In this case, the material properties are uniform.
//
#SPATIAL.ascii 1
SimpleDB {
  num-values = 3 // number of material property values
  value-names =  density vs vp // names of the material property values
  value-units =  kg/m**3  km/s  km/s // units
  num-locs = 1 // number of locations
  data-dim = 0
  space-dim = 3
  cs-data = geo-projected {
    to-meters = 1
    ellipsoid = WGS84
```

```
17      datum-horiz = WGS84
18      datum-vert = mean sea level
19      origin-lon = 0
20      origin-lat = 0
21      rotation-angle = 0
22      projector = projector {
23        projection = tmerc
24        units = m
25        proj-options = +lon_0=35.914 +lat_0=-2.764 +k=0.9996
26      }
27    }
28 }
29 // Columns are
30 // (1) x coordinate (longitude)
31 // (2) y coordinate (latitude)
32 // (3) z coordinate (depth m)
33 // (4) density (kg/m^3)
34 // (5) vs (km/s)
35 // (6) vp (km/s)
36 35.914   -2.764   -2000.0   2800.0   3.273   5.669
```

Appendix C

Chpt. 3 Supporting Information

The following codes create the package that is provided for GNSS2CHORDS and is available through the CHORDS GitHub repository (https://github.com/earth-cubeprojects-chords/chords/tree/master/bin/gnss2chords). The main executable is chords_stream. When this code is initialized parameters are read from the json file "parameter.json". Once the stream is active chords_parse.py reads in the NMEA string streaming, converts latitude, longitude, and time to the correct values and builds the necessary url for the ingestion into CHORDS.

C.1 Upload Script

chords_stream.py

```
1
2 #!/Users/joshj55/anaconda/bin/python2.7
3
4 ##Created by: Josh Jones, D. Sarah Stamps
5 ##Date last modified: 5 Dec 2018
6 ##This script is the streaming section of the UNAVCO -> CHORDS workflow
7 ##includes connections to nclient_beta, UNAVCO caster and chords_parse
8 ##Please read the README.txt file before starting
9
10 from __future__ import print_function
11 import socket
```

```
12 import sys
13 import psutil
14 from datetime import datetime
15 import base64
16 import requests
17 import time
18 import os
19 import subprocess
20 import argparse
21 import json
22 import pprint
23 import nclient_beta
24 import chords_parse
25 import logging
26
27 # Set true for debugging prints.
28 verbose = False
29
30 # Maximum number of caster authorization attempts.
31 MAX_CASTER_AUTH_ATTEMPTS = 10
32
33 logger = logging.getLogger(__name__)
34 module_name = file_name = __file__.split("/")[len(__file__.split("/"))-1]
35
36 def execute(cmd):
37         """Runs the chords_background script that activates the UNAVCO caster
      in the background."""
38
39         output= subprocess.Popen(cmd, stdout=subprocess.PIPE,
      universal_newlines=True)
40         for stdout_line in iter(output.stdout.readline, ""):
```

```
41                  yield stdout_line
42          output.stdout.close()
43          return_code = output.wait()
44          if return_code:
45                  raise subprocess.CalledProcessError(return_code,cmd)
46
47 def write_file(filename,write_line):
48          """Function that writes the data coming in from the UNAVCO caster
      subprocess."""
49
50          open_file= open(filename, "a")
51          open_file.write(str(write_line))
52          return filename
53
54 def get_args(argv):
55          """Parse the command line arguments.
56
57          Keyword arguments:
58          argv -- the command line argument vector
59
60          The arguments are returned as the argparse dictionary.
61          """
62          description = 'Stream UNVACO GNSS to CHORDS.'
63          epilog = """
64 The json file is structured as follows (order is not important):
65 {
66   "caster_ip":   "caster IP name",
67   "caster_port": "caster port number",
68   "caster_user": "caster user name",
69   "caster_pw":   "caster password",
70   "chords_ip":   "CHORDS portal IP name",
```

```
71   "chords_key":  "CHORDS portal data ingest key",
72   "sites": [
73     {"caster_site": "1st caster site", "chords_inst_id": "1st chords
     instrument id"},
74     ...
75     {"caster_site": "nth caster site", "chords_inst_id": "nth chords
     instrument id"}
76   ]
77 }
78
79 Set chords_key to an empty string if it is not required.
80 """
81
82         global verbose
83         parser = argparse.ArgumentParser(description=description, epilog=
     epilog,
84                 formatter_class=argparse.RawTextHelpFormatter)
85         parser.add_argument(
86                 '-j', '--json', metavar='file', action='store',type=str,
87                                                 help='json configuration file'
     , required=True)
88         parser.add_argument(
89                 '-v', '--verbose', action='store_true', default=False,
90                                                 help='enable debug printing')
91
92         args = parser.parse_args()
93
94         args_dict = vars(args)
95
96         # Was an accesible configuration file specified?
97         jsonfile = args_dict['json']
```

```
98          if not os.access(jsonfile, os.R_OK):
99                  logger.error("Configuration file %s is not readable." % (
    jsonfile,))
100                 exit(1)
101
102         # Enable/disable verbosity
103         verbose = args_dict['verbose']
104
105         return args_dict
106
107 def get_options(config_file):
108         """Return the configuration file options as a dictionary."""
109
110         # Read the json configuration from the file, importing it as a
    dictionary.
111         try:
112                 options = json.load(open(config_file))
113         except ValueError as e:
114                 logger.error('Error in the configuration file: %s. %s' % (
    config_file, e))
115                 exit(1)
116
117         if not validate_options(options):
118                 logger.error('Error(s) detected in the configuration file: %s'
     % (config_file,))
119                 exit(1)
120
121         if verbose:
122                 pprint.pprint(options)
123
124         return options
```

```
125
126 def validate_options(options):
127         """Validate that all of the required options are specified and
    legitimate.
128
129         return: True if ok, False otherwise.
130         """
131
132         # THIS ROUTINE NEEDS TO BE COMPLETED FOR ALL OPTIONS,
133         # INCLUDING THE ARRAY OF SITES.
134
135         ok = True
136         if 'caster_ip' not in options:
137                 logger.error('Configuration error: "caster_ip" is not present'
    )
138                 ok = False
139         if 'caster_port' not in options:
140                 logger.error('Configuration error: "caster_port" is not
    present')
141                 ok = False
142
143         return ok
144
145 def run_nclient(options):
146         """ Run nclient as a subprocess, returning data lines via yield.
147
148         Keyword arguments:
149         options -- a dictionary containing the json configuration file options
    .
150         """
151
```

```
152         user     = options['caster_user']
153         pw       = options['caster_pw']
154         port     = options['caster_port']
155         ip       = options['caster_ip']
156         site     = options['sites'][0]["caster_site"]
157
158         cmd = ['python', './nclient_beta.py', '-u', user+":"+pw, ip, port,
    site]
159         if verbose:
160                 print(cmd)
161
162         # Sometimes it takes a few tries to succesfully authorize with caster
163         auth_retries = 0
164         while auth_retries < MAX_CASTER_AUTH_ATTEMPTS:
165                 output = subprocess.Popen(cmd, stdout=subprocess.PIPE, bufsize
    =-1, universal_newlines=True)
166                 for line in iter(output.stdout.readline, ""):
167                         line = line.strip()
168                         yield line
169                 output.stdout.close()
170                 return_code = output.wait()
171                 if return_code == 2:
172                         auth_retries = auth_retries + 1
173                         time.sleep(1)
174                         logger.warning('Caster authorization failed, trying
    again...')
175                 else:
176                         break
177         if auth_retries > MAX_CASTER_AUTH_ATTEMPTS:
178                 logger.error('Caster authorization failed after %d attempts.'
    % (MAX_CASTER_AUTH_ATTEMPTS,))
```

```
179                 exit(1)
180         if return_code:
181                 raise subprocess.CalledProcessError(return_code, cmd)
182
183 if __name__=='__main__':
184         """Main block of code that repeats a connection request until
    connection with UNAVCO caster is made."""
185
186         logging.basicConfig(level=logging.INFO, stream=sys.stderr,
187                             format='%(asctime)s (' + module_name + ') %(levelname)
    s: %(message)s')
188
189         # Get the command line arguments.
190         args = get_args(argv=sys.argv)
191
192         # Get the configuration options
193         options = get_options(args['json'])
194
195         chords_ip = options['chords_ip']
196         chords_inst_id = options['sites'][0]['chords_inst_id']
197         chords_key = None
198         if options['chords_key'] != '':
199                 chords_key = options['chords_key']
200
201         # Run nclient, and feed the data lines to CHORDS
202         for gnss_line in run_nclient(options):
203                 if 'Unauthorized' in gnss_line:
204                         logger.error('Error: Authentication to %s:%s failed
    for user %s' % (options['caster_ip'], options['caster_port'], options['
    caster_user']))
205                         exit(1)
```

```
206                 if gnss_line[0] == '$':
207                         if verbose:
208                                 print(gnss_line)
209                         chords_parse.send_to_chords(
210                                 gnss_line=gnss_line,
211                                 chords_ip=chords_ip,
212                                 chords_key=chords_key,
213                                 chords_inst_id=chords_inst_id, verbose=verbose
    )
214                 else:
215                         logger.warning('Unrecognized line returned from caster
    : %s' % (gnss_line,))
```

chords_parse.py

```
1  from __future__ import print_function
2  import socket
3  import sys
4  import psutil
5  from datetime import datetime
6  import base64
7  import requests
8  import time
9  import os
10 import subprocess
11 from optparse import OptionParser
12 import nclient_beta
13 import chords_stream
14
15 def parse_string(string,direction):
16         """Parse the strings for latitude and longitude.
17
```

```
18          Requires string,direction as input which are read from the input file
    and contained in the path read.
19          """
20          string_val= map(str,string)
21          string_test=string.split('.')
22          string_deg= string_val[0]
23 #These statements find the degrees and minutes in the latitude/longitude for
    the difference in decimal places 1., 10., and 100.
24          if len(string_test[0]) == 3:
25                  string_deg= string_val[0]
26                  string_min= string_val[1]+string_val[2]
27          elif len(string_test[0]) == 4:
28                  string_deg= string_val[0]+string_val[1]
29                  string_min= string_val[2]+string_val[3]
30          elif len(string_test[0]) == 5:
31                  string_deg= string_val[0]+string_val[1]+string_val[2]
32                  string_min= string_val[3]+string_val[4]
33          string_sec= string_test[1]
34          string_min_sec= float(string_min+'.'+string_sec)/60
35          string_full=float(string_deg)+string_min_sec
36 #writes the directions as + or - based off of if the latitude/longitude is E/N
     or W/S| Necessary for CHORDS
37          if direction == 'E' or 'N':
38                  string_final= string_full
39          elif direction == 'W' or 'S':
40                  string_final= -1 * string_full
41          return string_final
42
43 def parse_time(time):
44          """Parses the time field read from the input file and place it into
    CHORDS format hr/min/sec."""
```

```
45
46          time_string= map(str,time)
47          time_split= time.split('.')
48          time_front=time_split[0]
49          time_hour= time_front[0]+time_front[1]
50          time_min= time_front[2]+time_front[3]
51          time_sec= time_front[4:]
52          time_fin= str(time_hour)+':'+str(time_min)+':'+str(time_sec)
53          return time_fin
54
55 def parse_date(date):
56          """Parses the data read from the input file and places it into CHORDS
        format yr/mon/day."""
57
58          date_string= map(str,date)
59          date_mon= date_string[0]+date_string[1]
60          date_day= (date_string[2])+(date_string[3])
61          date_yr= date_string[4]+date_string[5]
62          date_fin= str(20)+str(date_yr)+'-'+str(date_mon)+'-'+str(date_day)
63          return date_fin
64
65 def read_file(filename):
66          """Reads the input file and takes the information to be parsed."""
67
68          path= open(filename, "r")
69          read_path= path.readline()
70          path.close()
71          path= open(filename, "r+")
72          new_path= path.readlines()
73          updated_path= new_path[1:]
74          new_path.insert(0,updated_path)
```

```
75          path.close()
76          path= open(filename, "w")
77          path.writelines(updated_path)
78          path.close()
79          return read_path
80
81  def send_to_chords(gnss_line, chords_ip, chords_inst_id, chords_key=None,
        verbose = False):
82          myline = gnss_line.split(',')
83          time= myline[2]
84          date= myline[3]
85          latitude_string= myline[4]
86          latitude_dir= myline[5]
87          longitude_string= myline[6]
88          longitude_dir= myline[7]
89          latitude_final = str(parse_string(latitude_string,latitude_dir))
90          longitude_final= str(parse_string(longitude_string,longitude_dir))
91          time_final= str(parse_time(time))
92          date_final= str(parse_date(date))
93          height= str(myline[11])[3:]
94          date_fin = datetime.utcnow().strftime("%Y-%m-%d")
95          time_fin = datetime.utcnow().strftime("%H:%M:%S")
96          url = 'http://' + chords_ip + '/measurements/url_create?instrument_id=
        ' + chords_inst_id + \
97                  '&lat=' + latitude_final + \
98                  '&lon=' + longitude_final + \
99                  '&height=' + height + \
100                 'at=' + date_final + 'T' + time_final
101         if chords_key:
102                 url = url + "&key=" + chords_key
103         if verbose:
```

```
104                 print(url)
105         response=requests.get(url=url)
106         if verbose:
107                 print(response)
```

C.2 Download Script

```
1 # coding: utf-8
2
3 # In[22]:
4 ##Uncomment following line and In* lines to use in python notebook
5 #get_ipython().magic(u'pylab inline')
6
7 import json, requests, os, sys, glob, path, csv, urllib2, datetime
8 from datetime import timedelta
9
10 # In[23]:
11 ##Function to access csv data. for different portals use different url
12 def json_func(sites,date):
13     for i in range(0,len(sites)):
14         url = 'http://tzvolcano.chordsrt.com/api/v1/data/'+str(sites[i])+'.
    geojson?start='+str(date)+'T00:00&end='+str(date)+'T24:00'
15         response = requests.get(url=url)
16         data = json.loads(response.content)
17         sys.stdout= open(str(date)+'_'+str(sites[i])+'_tzv.json','w')
18         print json.dumps(data, indent=4, sort_keys=True)
19         sys.stdout.close
20
21 # In[24]:
22 ##Function to access csv data. for different portals use different url
```

```
23 def csv(sites,date):
24     for i in range(0,len(sites)):
25         url = 'http://tzvolcano.chordsrt.com/api/v1/data/'+str(sites[i])+'.csv
       ?start='+str(date)+'T00:00&end='+str(date)+'T24:00'
26         response = urllib2.urlopen(url)
27         data = response.read()
28         with open(str(date)+'_'+str(sites[i])+'_tzv.csv','wb') as f:
29             f.write(data)
30
31 # In[25]:
32 ##Input site numbers in array format to download all sites from TZVOLCANO
       CHORDS portal
33 date= datetime.date.today()
34 yesterday= date - timedelta(1)
35 day=yesterday.strftime('%Y-%m-%d')
36 sites=[5]
37 print(date,day)
38
39 # In[28]:
40 ##Runs the functions used to access and download data for sites and slected
       days
41 json_func(sites,day)
42 csv(sites,day)
```